2017

Chaotification as a Means of Broadband Vibration Energy Harvesting with Piezoelectric Materials

Daniel Geiyer
University of Central Florida

CHAOTIFICATION AS A MEANS OF BROADBAND VIBRATION ENERGY HARVESTING WITH PIEZOELECTRIC MATERIALS

by

DANIEL GEIYER
Bachelor of Science from Rochester Institute of Technology 2011
Master of Engineering from Rochester Institute of Technology 2011

A dissertation submitted in partial fulfilment of the requirements
for the degree of Doctor of Philosophy
in the Department of Mechanical and Aerospace Engineering
in the College of Engineering and Computer Science
at the University of Central Florida
Orlando, Florda

Fall Term
2017

Major Professor: Jeffrey L. Kauffman

ABSTRACT

Computing advances and component miniaturization in circuits coupled with stagnating battery technology have fueled growth in the development of high efficiency energy harvesters. Vibration-to-electricity energy harvesting techniques have been investigated extensively for use in sensors embedded in structures or in hard-to-reach locations like turbomachinery, surgical implants, and GPS animal trackers. Piezoelectric materials are commonly used in harvesters as they possess the ability to convert strain energy directly into electrical energy and can work concurrently as actuators for damping applications. The prototypical harvesting system places two piezoelectric patches on both sides of the location of maximum strain on a cantilever beam. While efficient around resonance, performance drops dramatically should the driving frequency drift away from the beam's fundamental frequency. To date, researchers have worked to improve harvesting capability by modifying material properties, using alternative geometries, creating more efficient harvesting circuits, and inducing nonlinearities. These techniques have partially mitigated the resonance excitation dependence for vibration-based harvesting, but much work remains.

In this dissertation, an induced nonlinearity destabilizes a central equilibrium point, resulting in a bistable potential function governing the cantilever beam system. Depending on the environment, multiple stable solutions are possible and can coexist. Typically, researchers neglect chaos and assume that with enough energy in the ambient environment, large displacement trajectories can exist uniquely. When subjected to disturbances a system can fall to coexistent lower energy solutions including aperiodic, chaotic oscillations. Treating chaotic motion as a desirable behavior of the system allows frequency content away from resonance to produce motion about a theoretically infinite number of unstable periodic orbits that can be stabilized through control. The extreme sensitivity to initial conditions exhibited by chaotic systems paired with a pole placement control strategy pioneered by Ott, Grebogi, and Yorke permits small perturbations to an accessible system

parameter to alter the system response dramatically. Periodic perturbation of the system trajectories in the vicinity of isolated unstable orbit points can therefore stabilize low-energy chaotic oscillations onto larger trajectory orbits more suitable for energy harvesting.

The periodic perturbation-based control method rids the need of a system model. It only requires discrete displacement, velocity, or voltage time series data of the chaotic system driven by harmonic excitation. While the analysis techniques are not fundamentally limited to harmonic excitation, this condition permits the use of standard discrete mapping techniques to isolate periodic orbits of interest. Local linear model fits characterize the orbit and admit the necessary control perturbation calculations from the time series data.

This work discusses the feasibility of such a method for vibration energy harvesting, displays stable solutions under various control algorithms, and implements a hybrid bench-top experiment using MATLAB and LabVIEW FPGA. In conclusion, this work discusses the limitations for wide-scale use and addresses areas of further work; both with respect to chaotic energy harvesting and parallel advances required within the field as a whole.

Music has been and always will be a significant part of my life. This dissertation is dedicated to all the people I have had the pleasure of sharing a dance floor with; whether from in front or behind the DJ booth. The kick drum and its unyielding dedication to the thump in clubs all around the world pushed me to finish this work.

ACKNOWLEDGMENTS

First and foremost I would like to thank my advisor, Jeff Kauffman, who took me in at a transitional time where I was almost ready to put graduate school aside entirely. His willingness to merge our interests led us into an exciting project that I am glad to have participated in. His laid back advising style and openness to tangential ideas often led to the more interesting aspects of this research. I will always appreciate our discussions, both within the scope of the project and lessons learned about life beyond academia.

Thank you to my committee members Tuhin Das, Faissal Moslehy, and Bhimsen Shivamoggi for lending their respective expertise at various stages throughout this project. Though we did not meet often, coming together always explored the line between laughing and learning.

Thank you to Anthony Fiacco, Christopher Rukas, Sadaf Mackertich, Jeffrey Chiappone, and Julie Lisuzzo who all at one time or other can be considered part of the family. Our fleeting time together due to the demanding schedules of graduate school were a much appreciated change of pace and introspective reminder about the importance of close connections. Additional thanks to Ed Santiago, Tulio Silberberg, Elizabeth Palmer, Veronica Prisco, Melissa Spanos, and Shana Procopio for keeping me sane daily through our entertaining chat sessions about anything and everything.

Thank you to my fellow office colleagues Garrett Lopp, Brandi McPherson, Christopher Kelley, James Little, and Taylor Hynds. On many occasions our days turned into nights and we were always able to have a good time whether it was spent rushing to a deadline or playing Nintendo 64 projected onto a wall. May the group chat live on forever and future reunions be plentiful.

I want to thank my family, for without them I would not be where I am today. Curiously was always encouraged throughout my childhood and I was fortunate to freely explore interests across activities from music, to martial arts, and beyond. I believe that upbringing is what led me to consider a PhD. Lastly, thank you for always acting as a sounding board during my more stressful moments; especially towards the end of this program.

I would like to take a moment and reflect on the experiences afforded to me during this process. I grew up in an environment that fostered travel as a way of opening the mind. During the course of my graduate studies I was able to travel to various cities around the United States, Canada, Mexico, Jamaica, Brazil, the Netherlands, Germany, the United Kingdom, and Iceland. The experiences and lessons learned during these adventures have helped shape who I am and contributed to my success.

I end this section in attempt to shed light on an often ignored but ever present topic of personal health. At times I did not do enough to take care of myself and I hope those reading this, whether in academia or not, find the time to do what I often did not do to stay healthy and well balanced.

TABLE OF CONTENTS

LIST OF FIGURES

CHAPTER 1: INTRODUCTION

Component miniaturization and reduced power requirements in modern electronics have spurred significant developments in new sensing equipment and applications. Health monitoring devices have been designed that detect changes in the structural integrity of buildings, bridges, and cars. Tracking devices have been deployed to monitor wildlife and assist in research efforts studying the behavior of various animal species. Pacemakers have been implanted in patients with heart conditions in efforts to regulate blood flow and extend life expectancy. These technologies are all driven by the advances in computing performance, but all require some type of on-board power source for operation [1].

To date batteries have been the primary solution for wireless power applications, but their low power density often results in large, costly devices not ideal for small-scale applications. In addition, charging and replacing batteries requires hazardous maintenance and inhibits use beyond easily accessible locations. Conversely, ideal health monitoring usually requires sensors to be embedded within a structure. Disturbing wildlife creates safety concerns and can interfere with the natural behavior of the species being tracked. Undergoing routine open heart surgery at significant risk to a patients' health all help to prove why alternative powering methods are highly desirable to mitigate the shortcomings of battery-based technologies. The influx of applications using small-scale electronics can all benefit from the scavenging of power from the ambient environment itself.

1.1 Energy Harvesting

Ambient sources of energy generally fall into four categories: light, radio frequency (RF) electromagnetic radiation, thermal gradients, and motion [2]. Successful implementation of all four meth-

ods has been achieved and selection of an "ideal" technique is both dependent on the application itself and the expertise of the designer. Large-scale power generation from wind and solar energy have successfully supplemented power grid demands from traditional coal-based sources, but are not the subject of this work. The end goal of the harvesting method developed in this dissertation relates specifically to small-scale sensor networks incorporating thousands of nodes operating across a wide band of frequency content from the ambient environment. Common application environments may not receive enough light and temperature differences could potentially be small across the surface of the harvesting element [3, 4]. In line with the device's small physical size, efficient RF extraction from devices smaller than the radiation wavelength poses a problem [5]. Therefore, small-scale distributed sensor networks more readily lend themselves to motion-based energy harvesting.

1.1.1 Vibration Energy Harvesting

Ambient environments produce vibration either directly through an object's motion, or through motion imparted on a structure from external sources (e.g. a car driving over a bridge) illustrated in Figure 1.1. To benefit from these small scale motions, efficient transduction mechanisms are needed to extract usable levels of power for each node in the sensor network. In these applications, electromagnetic induction [6], electrostatic generation [7], dielectric elastomers [8], and piezoelectric materials [9] have all been investigated for extracting usable amounts of ambient vibration energy.

Electromagnetic induction uses the relative motion between a conductor and a magnetic field to generate electricity according to Faraday's Law. The magnetic field strength, number of coil turns, and relative velocity between the coil and the magnet all affect the potential power output of the device. The absence of a bias voltage is a benefit of an electromagnetic design, but a rectifier and

DC converter are required to charge a storage component. Additionally, electromagnetic generators are low-voltage, high-current devices due to a low optimal circuit resistance and require a voltage multiplier to reach the voltage minimums of conventional storage components. A typical configuration for an electromagnetic harvester shown in Figure 1.2 uses a permanent magnet attached at the free end of a base-excited cantilever beam to pass through a fixed coil [1].

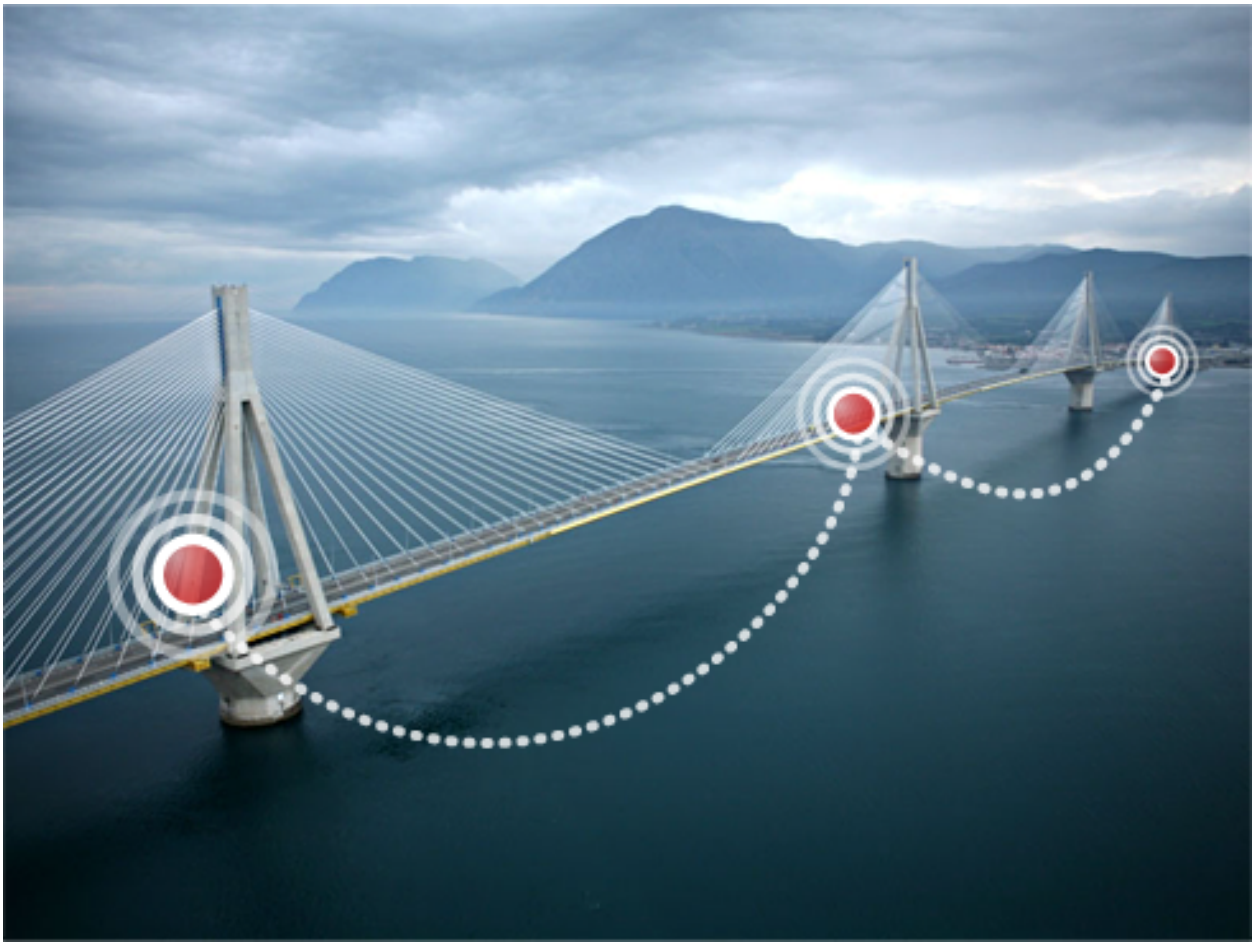

Figure 1.1: A rendering of a wireless sensor network on a suspension bridge [10]

Contrary to an electromagnetic generator, electrostatic transduction uses ambient vibrations to move plates of a variable capacitor separated by a dielectric material against the electrostatic forces between electrodes. The dielectric material is used to increase harvested energy and prevent the capacitor plates from making contact during excitation. To keep the capacitive plates oppositely

charged, a constant DC voltage is required, usually applied through an on-board battery. For each operating cycle the capacitance is varied from a minimum to a maximum value, with energy transfer dependent on the ratio of minimum to maximum capacitance. Two in-plane configurations exist with displacement either closing the gap or causing an overlap between the capacitor plates. A third configuration uses out-of-plane vibrations to move one capacitor plate relative to the other. The in-plane gap closing layout is preferred as it minimizes relative rotation between the plates under asymmetrical excitation and generates comparable power to the other configurations with less displacement [1, 11]. Figure 1.3 depicts a traditional in-plane electrostatic transducer.

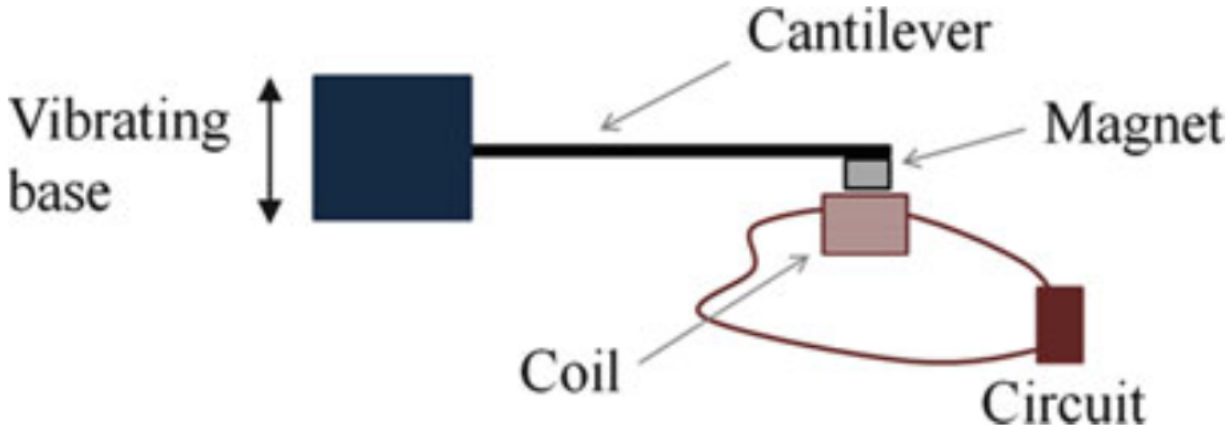

Figure 1.2: An electromagnetic induction-based vibration energy harvester [1]

Electroactive polymers for energy harvesting exist in two forms; dielectric elastomers (EAPs), or ionic polymer metal composites (IPMCs). EAPs exhibit polarization-based electromechanical coupling and work similarly to electrostatic transducers. A dielectric material, typically a soft rubber, is placed between two oppositely charged capacitive plates (bias voltage) and exhibits a four stage harvesting cycle. First, a supplemental battery is used to stretch the dielectric elastomer increasing capacitance of the system. Second, the system is switched to an open-circuit configuration and the dielectric elastomer thickens under a fixed high-charge state. Third, the system is switched to the storage device and system capacitance is reduced as tension in the dielectric elastomer is lost

under further thickening. Lastly, switching back to open-circuit at the low-charge state increases tension and reduces thickness in the dielectric elastomer and completes the harvesting cycle. Maximum energy conversation of an EAP is determined by the electromechanical characteristics of the polymer, electrical breakdown, electromechanical instability, loss and tension, and rupture of the polymer [1].

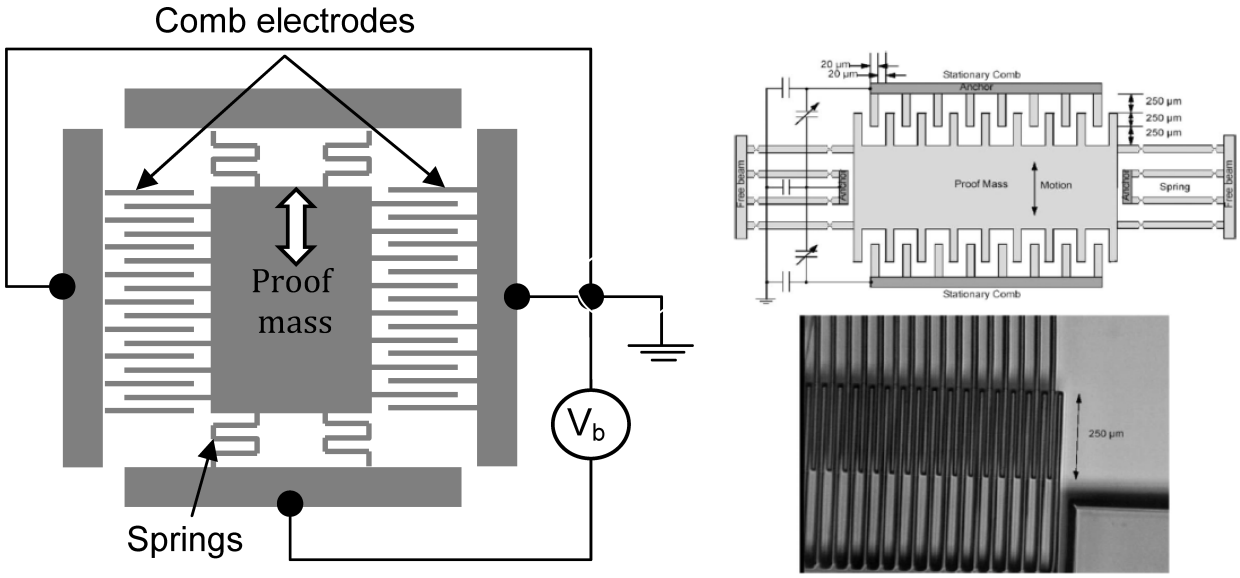

Figure 1.3: In-plane configurations of an electrostatic generator-based vibration energy harvester [12]

IPMCs exhibit electromechanical coupling through diffusion or conduction of charged species in the polymer network. The ionic polymers are composed of Nafion or Flemion and coated by conductive electrodes typically made of gold or platinum. As the ionic polymer is deformed, a charge concentration gradient results as the free cations travel from high-density to low-density regions forcing a potential difference across the electrodes. While similar to piezoelectric harvesters, significantly lower power densities prohibit wide scale usage of this technique [1]. Figure 1.4 illustrates configurations of both a dielectric elastomer harvester and an electroactive polymer harvester.

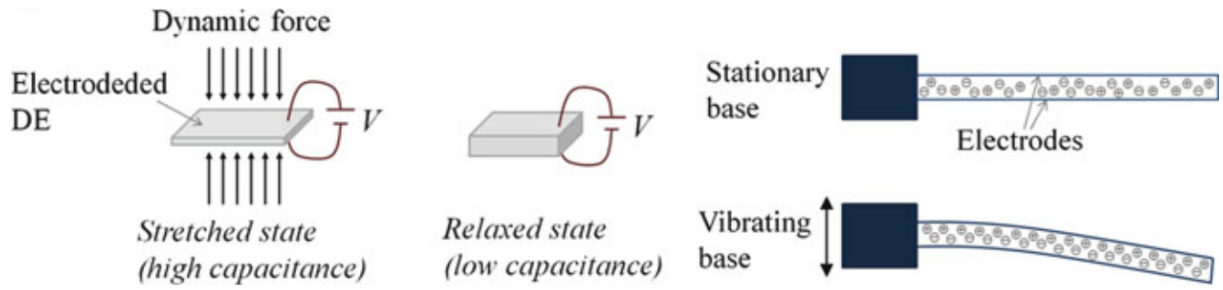

Figure 1.4: A dielectric elastomer and electroactive polymer based vibration energy harvester [1]

Piezoelectric materials are more commonly considered for vibration based energy harvesting due to their direct ability to convert strain energy into electrical energy. The high-voltage, low-current nature of piezoelectric-based harvesters eliminate the need of a voltage multiplier circuit, and bias voltages are not needed for ideal operation. As such, piezoelectric materials can be implemented more readily than other vibrations transduction methods and have received considerably more attention by the research community [9, 13].

1.1.2 Piezoelectric-based Energy Harvesting

Energy harvesting with piezoelectric materials takes advantage of the direct piezoelectric effect, where an applied mechanical force generates internal electric charge. An induced dynamic strain from the environment generates an alternating voltage output across the electrodes of the piezoelectric material. To amplify the displacement and strains of the piezoelectric elements, the patches are typically coupled to a base-excited cantilever beam at maximum strain locations. An ideal beam would possess low mechanical damping and thus well-separated modes with respect to the structure's primary resonance. As a direct result, the cantilever-based harvester has a narrow operating bandwidth where maximum displacement is only attained when the primary resonance frequency is tuned to a dominant frequency existing in the ambient environment. Unfortunately, the operating

requirements of the harvester are often not consistent with the energy spectra of the ambient environment. Using harvesters dependent on a single resonance frequency in environments that do not possess strong dominant frequencies limits their potential power harvesting capability and warrants a solution. Figure 1.5 illustrates the piezoelectric-based cantilever harvester and the narrow-band frequency response functions using various proof masses.

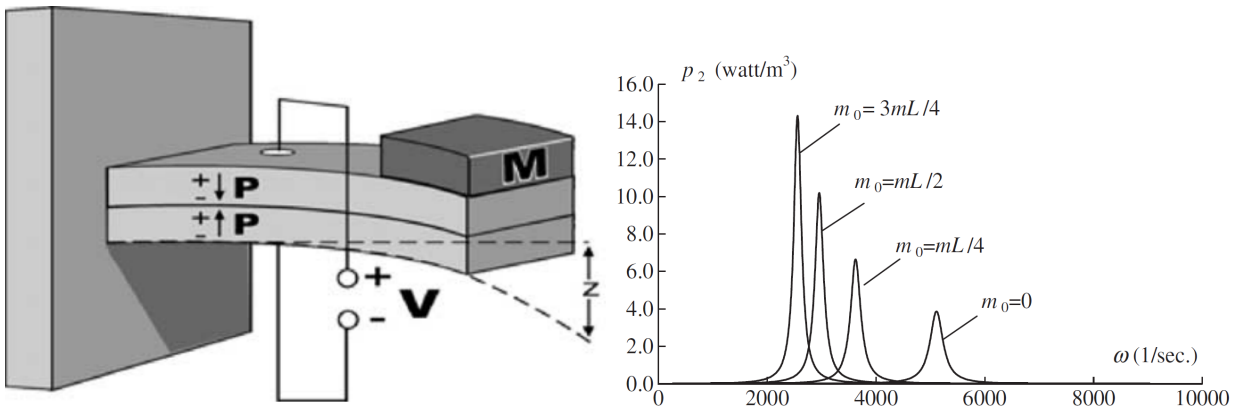

Figure 1.5: A linear cantilevered piezoelectric energy harvester and frequency response [11]

1.1.3 Improved Vibration Energy Harvesting through Nonlinearity

A common technique to increase the bandwidth of vibration energy harvesters is to introduce a nonlinearity and benefit from the rich set of dynamic responses therein. While various methods of introducing nonlinearity exist, the most common creates a typical Duffing oscillator with coexisting attractors that can exhibit widely different dynamic responses [14–16]. Such solutions allow for small-amplitude periodic responses, large-amplitude periodic responses, and an aperiodic chaotic response. All realizable dynamic responses exist away from the system's fundamental frequency, mitigating the resonance limitation. The different system responses can also exist concurrently dependent on the initial conditions.

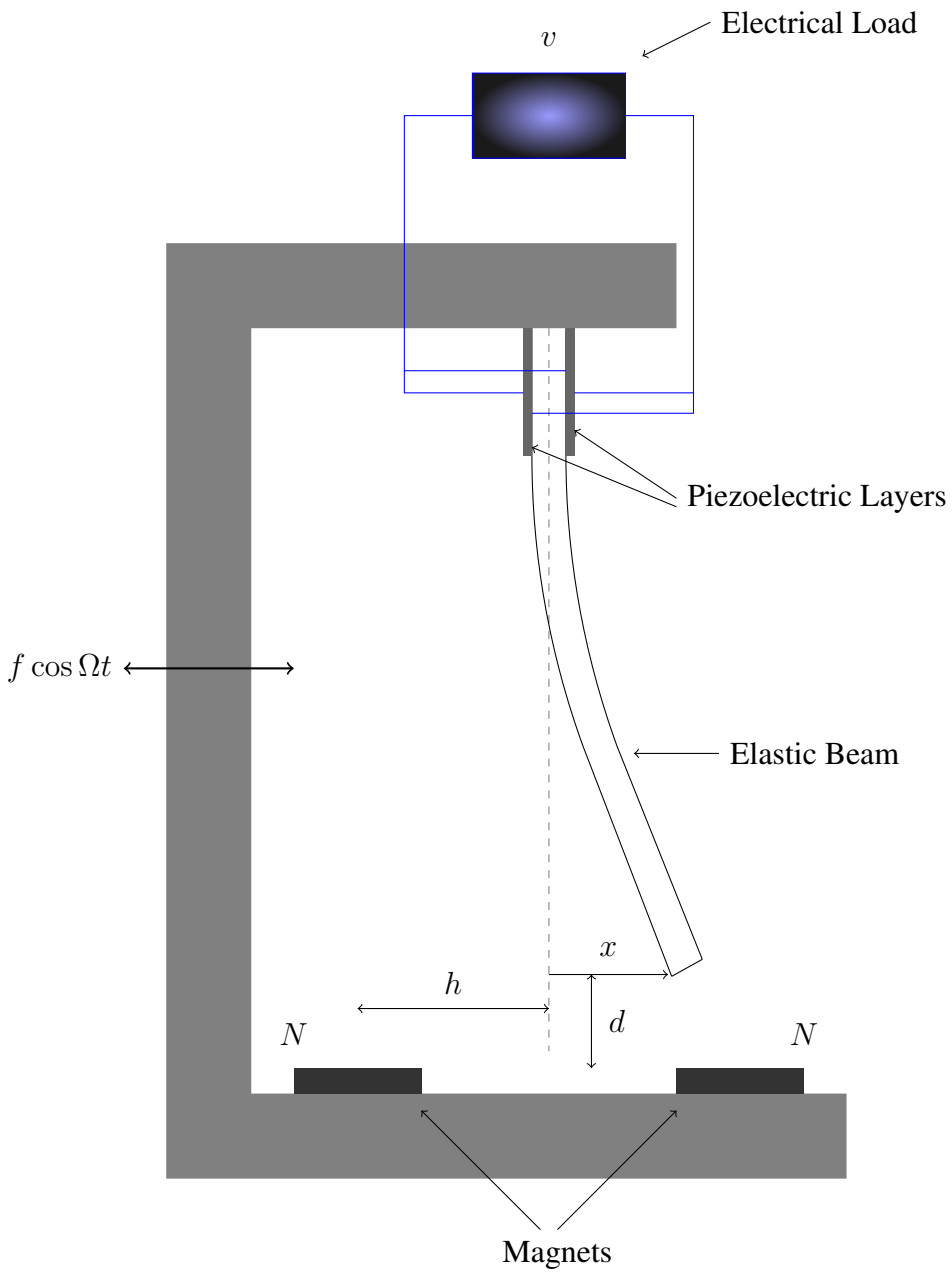

Figure 1.6: A Duffing oscillator-based nonlinear vibration energy harvester

It is implied that a larger displacement periodic solution correlates to greater energy output of the system both due to higher strain in the piezoelectric element and periodicity expected by the harvesting circuitry. To date significant work has been performed in optimizing the large displacement periodic response. Parallel research efforts have focused to better understand the nonlinear dynam-

ics and reduce the frequency range where alternative responses can concurrently exist. The large amplitude response is also often assumed to be maintained indefinitely through proper choice of initial conditions and subsequent perturbation [17–19]. However, improving the frequency range where large amplitude responses exist uniquely only minimally improves operating bandwidth. Unplanned environmental disturbances can cause the system to transition into the lower-energy chaotic attractor, and arbitrary perturbations can significantly reduce the net positive power output of the harvesting system. Rather than avoid chaos, the inherent sensitivity to initial conditions can be considered an advantage when operating in conjunction with a low-power controller developed by Ott, Grebogi, and Yorke (OGY)for maintaining large displacement orbits across a range of excitation frequencies [20].

1.2 Chaotification and Subsequent Control for Improved Harvester Operation

Inducing chaotic motion requires the system to operate within a specific range of forcing parameters and initial conditions. Fortunately, chaotic motion is present through a wide band of excitation frequencies and exists more readily than the optimal large displacement solution in low energy environments. Once induced, a number of steps are required before successful control onto a desirable periodic orbit can be achieved. First, the chaotic attractor must be mapped by sampling system states timed with the excitation period. A recurrence detection algorithm can then be used to isolate the unstable orbit points within the system. A strength of the discretized methods allow the recurrence detection to be completed either in real time, or calculated a priori for known environments. Since the control effort is based on small perturbations, locally linear system models can be fit to each isolated orbit point for subsequent control.

A piezoelectric energy harvester dependent on chaotic motion is inherently a robust system. Whereas linear cantilevered configurations are tuned in the design phase before implementation, nonlinear

chaotic harvesters can be optimized in real time, dependent on the operating environment. The existence of chaos creates an infinite number of unstable orbits embedded within the chaotic attractor. Should the operating environment shift in frequency, or a different periodic orbit be desired, the temporal programming of the small control effort can be changed on-line. Expanding on the idea of real-time control updates, learning algorithms can be implemented so that identical harvesters placed throughout a networked environment can learn the optimal control law for efficient harvesting during operation. Learning harvesters can save large amounts of money over redesigning a system every time a change is detected in the ambient vibration frequency spectrum or a new environment is targeted. Introducing learning harvesters into vibration-rich environments can lead to new applications of remote power sources. Since the devices may already be networked for data sharing, power can be harvested from a few devices in vibration-rich areas of an environment and transfered wirelessly to other devices either in low-vibration areas of an environment or to devices that do not possess an on-board harvester.

1.3 Objectives of this Dissertation

Increasing both the operating bandwidth and the potential power output of a piezoelectric energy harvester can positively impact their application in distributed sensor networks. Micro-scale sensors can be implemented in hard to reach locations without the need for cabling or battery maintenance. These sensors can act independently or as part of a larger array while exhibiting a longer life cycle than the current state of the art. In addition, the use of piezoelectric materials will not only enable health monitoring, process monitoring, and feedback control, but will also allow simultaneous sensing and actuation, further reducing the number of components in a full-scale system [21].

The novelty of the proposed harvester stems from the use of an active controller in stabilizing

periodic orbits within a chaotic attractor. While an active component utilizes some of the generated energy, the extreme sensitivity to initial conditions limits the expended power requirements. Current harvesting systems also do not show an ability to adapt on their own should the operating environment change. The significance of the proposed work is the step taken towards designing battery independent devices with minimal tuning in the design phase. The eventual addition of learning harvesters capable of adapting to the ambient environment introduces the idea of a general all-purpose device for use in many sensing, actuation, and remote power applications in distributed wireless networks.

1.4 Dissertation Structure

This dissertation guides the reader through the field of piezoelectric energy harvesting and details a novel technique for creating a more efficient high-bandwidth harvesting device.

Chapter 2 explores the motivation for vibration-based energy harvesting and the role of piezoelectricity in the process. A clear path through the literature dictates the limitations of current linear and nonlinear techniques, laying the foundation for more optimal nonlinear approaches for energy harvesting away from resonance. Chaotic dynamics, modeling techniques, and control are explained as related to their improvements in nonlinear energy harvesting.

Chapter 3 derives a lumped parameter model of the bistable harvesting system to dictate the effects of the potential function on the solution trajectories. Coexistent attractors are explored, and statistical recurrence techniques are explained to isolate unstable periodic orbits within the chaotic attractor. From the isolated orbits, least squares fit methods for an approximate linear model are explained, and various control methods are derived in relation to this model. Delay coordinate embedding is also introduced, approximating the full nonlinear harvester through measurement of

a single state of the system.

Chapter 4 illustrates the theoretical solution of the harvesting model under various forms of control. In conjunction with the simulations, the development of an experimental test stand is dictated and used as a proof of concept towards real-world implementation on a nonlinear energy harvester with active chaos control. Switch-based harvesting circuitry is described in relation to applying control perturbations to multiple parameters of the system and harvesting potential is qualitatively explained.

Lastly, Chapter 5 reiterates the benefits of the proposed harvesting system and explains its novelty and significance to the field as a whole. In addition, remaining research questions are explored both within the field of energy harvesting and the subfields of nonlinear dynamics and chaos control. The unification of advances of the aforementioned fields would serve to advance development of the nonlinear piezoelectric-based energy harvesting system.

CHAPTER 2: BACKGROUND

Prior to developing the theoretical framework of an improved nonlinear vibration energy harvester, a review of the relevant literature is needed to provide sufficient understanding of the problem as well as any analysis methods needed herein. This chapter starts by considering the electromechanical phenomena of piezoelectricity and its constitutive relations. Common coupling methods are explored, with detail on the prototypical cantilever beam structure primarily used in vibration energy harvesting. Limitations of the linear system and the induced nonlinearity are explained along with the potential energy functions and the dynamic attractors. The need for chaos control and common forms of chaos control are then detailed as relevant to nonlinear vibration energy harvesting.

2.1 Piezoelectricity

Piezoelectricity is a naturally occurring process where certain solid materials exhibit electromechanical responses in the event of a mechanical stress or an electric field. The direct piezoelectric effect describes the electric charge that accumulates in response to an applied mechanical stress [22]. By extension, the indirect effect describes when a mechanical force develops due to the application of a magnetic field [23]. While the direct effect was discovered in 1880 by French physicists Jacques and Pierre Curie and the indirect effect one year later by Gabriel Lippmann, piezoelectricity was not full classified until Woldemar Voigt's paper in 1910. His paper classified the crystal structures that exhibit piezoelectricity and defined twenty classes of crystal capable of piezoelectricity and defined their piezoelectric constants [24].

2.1.1 Piezoelectric Materials

There are many natural and synthetic materials that exhibit piezoelectric effects. Quartz, berlinite, sucrose, Rochelle salt, and topaz are a few naturally occurring crystals known to have piezoelectric properties. Interestingly, biological materials such as tendon, silk, wood, enamel, dentin, and DNA possess piezoelectric properties as well. Fukada et al. observed the piezoelectric effect within the collagen of dry bones [25]. More recently, Lee et al. showed the existence of piezoelectric behavior in viral proteins. Specifically, thin films of M13 bacteriophage were used to generate enough electricity to power a liquid crystal display [26]. For large-scale piezoelectric energy harvesting, naturally occurring crystals and biological micro-materials do not produce enough power. Synthetic materials are common choices for harvesting and include gallium orthophosphate, barium titanate and lead titanate. Sodano et al. concluded lead zirconate titanate (PZT) to be the most efficient piezoceramic for energy harvesting in its ability to charge a battery under random vibrations typically present in an environment as compared to other synthetic materials [27].

2.1.2 Constitutive Relations

The piezoelectric effect is mathematically described through the constitutive relations of piezoelectric materials showing the interaction between stress T, strain S, charge-density displacement D, and electric field E. The Cartesian coordinate system shown in Figure 2.1 illustrates the common axis labeling convention in mathematical formulation and polarization of a piezoelectric cube. Four standard sets of linear relations exist; strain-charge form is shown in index notation in Equation 2.1 [28, 29]:

$$\begin{aligned} S_{ij} &= s^{E}_{ijkl} T_{kl} + d_{kij} E_k \\ D_i &= d_{ikl} T_{kl} + \epsilon^{T}_{ik} E_k \end{aligned} \tag{2.1}$$

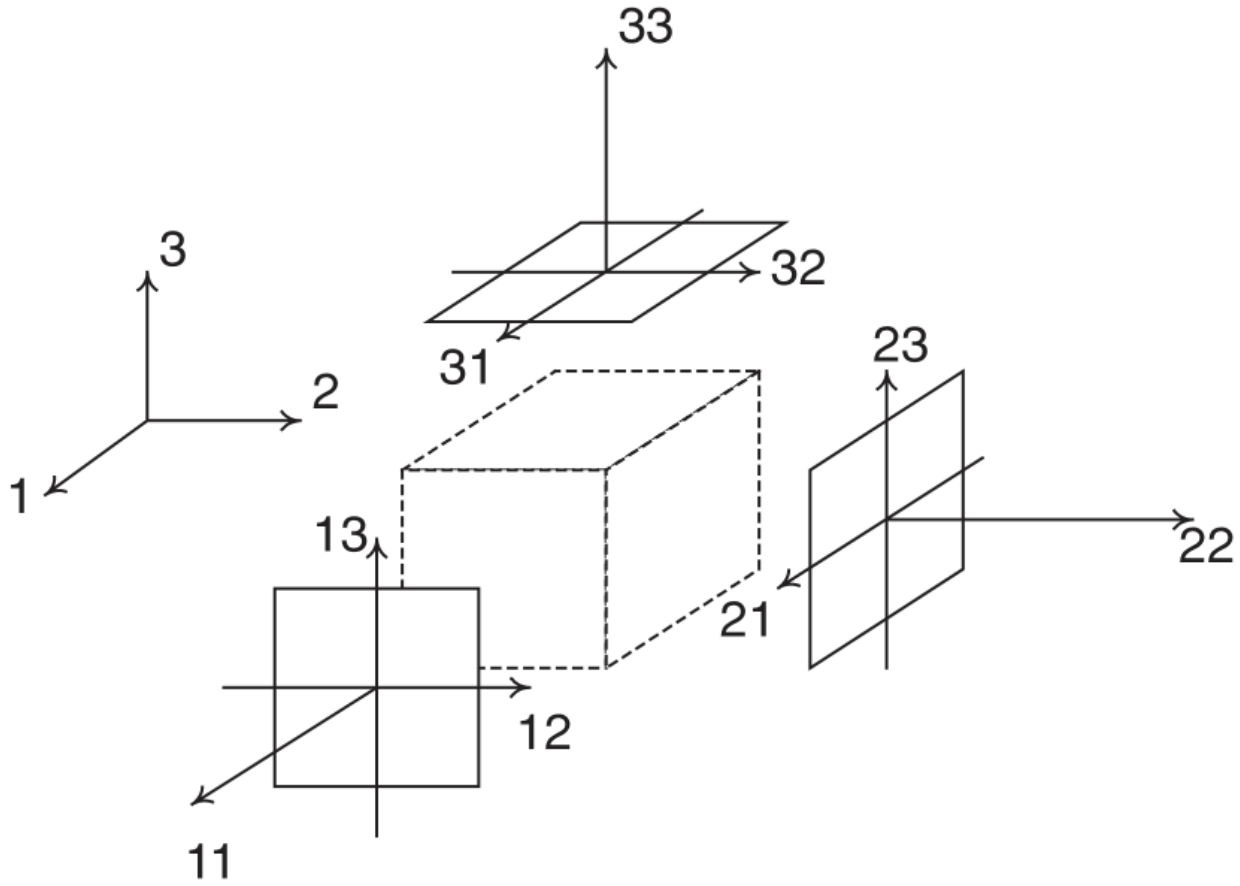

Figure 2.1: Coordinate axes of a piezoelectric cube [29]

The complete set of equations are defined by 81 mechanical compliance constants, 27 piezoelectric strain coefficient values, and 9 dielectric permittivities. Due to symmetry of the stress and strain tensors, only 6 elements of stress and strain are unique and a notation reduction known as Voigt notation can be applied. Equation 2.2 shows how Voigt notation reduces stress and strain components from an (i, j) index notation where each component takes a value from 1 through 3 to a single index of values 1 through 6.

$$\begin{aligned} S_1 &= S_{11} & T_1 &= T_{11} \\ S_2 &= S_{22} & T_2 &= T_{22} \\ S_3 &= S_{33} & T_3 &= T_{33} \\ S_4 &= S_{23} + S_{32} & T_4 &= T_{23} + T_{32} \\ S_5 &= S_{31} + S_{13} & T_5 &= T_{31} + T_{13} \\ S_6 &= S_{12} + S_{21} & T_6 &= T_{12} + T_{21} \end{aligned} \tag{2.2}$$

Using Voigt notation, Equation 2.1 can be rewritten [29]:

$$\begin{aligned} S_i &= s_{ij}^E T_j + d_{ik} E_k \\ D_m &= d_{mj} T_j + \epsilon_{mk}^T E_n \end{aligned} \tag{2.3}$$

where i and j take on values from 1 through 6 and m and n take on values from 1 through 3. This simplification results in 36 independent elastic coefficients, 18 piezoelectric strain coefficients, and 9 dielectric permittivities. The constitutive equations can be compacted further into the commonly known matrix form [28]:

$$\begin{Bmatrix} \mathbf{S} \\ \mathbf{D} \end{Bmatrix} = \begin{bmatrix} \mathbf{s}^E & \mathbf{d}^t \\ \mathbf{d} & \epsilon^T \end{bmatrix} \begin{Bmatrix} \mathbf{T} \\ \mathbf{E} \end{Bmatrix} \tag{2.4}$$

where $\mathbf{s}^E$ is a 6×6 matrix of compliance coefficients, $\mathbf{d}$ is a 3×6 matrix of piezoelectric strain

coefficients, and ϵ^T is a 3×3 matrix of dielectric permittivities. Superscripts E and T are used to indicate that the quantity is taken at constant electric field and stress, respectively, and t represents the transpose operator [29]. Further reduction of the number of parameters comes with the knowledge that most manufactured piezoelectric materials are orthotropic and therefore $s_{ij} = s_{ji} = 0$ with $i = 1, 2, 3$, $j = 4, 5, 6$ and $s_{45} = s_{46} = s_{56} = s_{65} = 0$. Piezoelectric materials also exhibit a plane of symmetry resulting in equal elastic moduli in the 1 and 2 directions illustrating transversely isotropic behavior. Similarly, electric fields applied in any direction will not produce electric displacements in the orthogonal directions. Therefore the number of coefficients can be reduced further and written in the expanded matrix form:

$$\begin{bmatrix} S_1 \\ S_2 \\ S_3 \\ S_4 \\ S_5 \\ S_6 \end{bmatrix} = \begin{bmatrix} s_{11}^E & s_{12}^E & s_{13}^E & 0 & 0 & 0 \\ s_{21}^E & s_{22}^E & s_{23}^E & 0 & 0 & 0 \\ s_{31}^E & s_{32}^E & s_{33}^E & 0 & 0 & 0 \\ 0 & 0 & 0 & s_{44}^E & 0 & 0 \\ 0 & 0 & 0 & 0 & s_{55}^E & 0 \\ 0 & 0 & 0 & 0 & 0 & s_{66}^E \end{bmatrix} \begin{bmatrix} T_1 \\ T_2 \\ T_3 \\ T_4 \\ T_5 \\ T_6 \end{bmatrix} + \begin{bmatrix} 0 & 0 & d_{31} \\ 0 & 0 & d_{32} \\ 0 & 0 & d_{33} \\ 0 & d_{24} & 0 \\ d_{15} & 0 & 0 \\ 0 & 0 & 0 \end{bmatrix} \begin{bmatrix} E_1 \\ E_2 \\ E_3 \end{bmatrix} \tag{2.5}$$

$$\begin{bmatrix} D_1 \\ D_2 \\ D_3 \end{bmatrix} = \begin{bmatrix} 0 & 0 & 0 & 0 & d_{15} & 0 \\ 0 & 0 & 0 & d_{24} & 0 & 0 \\ d_{13} & d_{23} & d_{33} & 0 & 0 & 0 \end{bmatrix} \begin{bmatrix} T_1 \\ T_2 \\ T_3 \\ T_4 \\ T_5 \\ T_6 \end{bmatrix} + \begin{bmatrix} \epsilon_{11}^T & 0 & 0 \\ 0 & \epsilon_{22}^T & 0 \\ 0 & 0 & \epsilon_{33}^T \end{bmatrix} \begin{bmatrix} E_1 \\ E_2 \\ E_3 \end{bmatrix} \tag{2.6}$$

where:

$$s^E = \begin{bmatrix} \frac{1}{Y_1^E} & \frac{-\nu_{12}}{Y_1^E} & \frac{-\nu_{13}}{Y_1^E} & 0 & 0 & 0 \\ \frac{-\nu_{21}}{Y_2^E} & \frac{1}{Y_2^E} & \frac{-\nu_{23}}{Y_2^E} & 0 & 0 & 0 \\ \frac{-\nu_{31}}{Y_3^E} & \frac{-\nu_{32}}{Y_3^E} & \frac{1}{Y_3^E} & 0 & 0 & 0 \\ 0 & 0 & 0 & \frac{1}{G_{23}^E} & 0 & 0 \\ 0 & 0 & 0 & 0 & \frac{1}{G_{13}^E} & 0 \\ 0 & 0 & 0 & 0 & 0 & \frac{1}{G_{12}^E} \end{bmatrix} \tag{2.7}$$

Compliance terms are dependent on the short-circuit elastic moduli, Poisson's ratio, and the short circuit shear-moduli.

In relation to harvesting potential, a simple metric relating the elastic boundary conditions imposed on the material known as the piezoelectric coupling coefficients is defined as:

$$k_{ij} = \frac{d_{ij}}{\sqrt{\epsilon_{ii}^T s_{jj}^E}} \tag{2.8}$$

and is typically found in vendor catalogs. Deciding which index is important depends on the mode of operation in which the harvester is being utilized. For each mode of coupling where only one stress or strain component and one electric displacement or field component is non-zero, a separate coefficient exists [28]. The constitutive relations are then simplified to scalar terms. The coupling coefficient can also be defined mechanically as the difference between open-circuit and short-circuit stiffness (c^D and c^E) and electrically defined as the difference between free and blocked dielectric permittivity (ϵ^T and ϵ^S):

$$k^2 = \frac{c^D - c^E}{c^D} = \frac{\epsilon^T - \epsilon^S}{\epsilon^T} \tag{2.9}$$

Equation 2.9 can be rewritten in terms of resonant frequencies under short-circuit and open-circuit

conditions:

$$k^2 = \frac{\omega_{oc}^2 - \omega_{sc}^2}{\omega_{oc}^2}. \tag{2.10}$$

Note, while similar to the generalized mechanical coupling coefficient κ, the two are not the same. The generalized mechanical coupling coefficient κ is the ratio of converted energy to unconverted energy and always positive. When κ equals infinity under complete energy conversion, k reaches a theoretical maximum of unity [30]. The two quantities k and κ are related by:

$$\kappa^2 = \frac{\omega_{oc}^2 - \omega_{sc}^2}{\omega_{sc}^2} = \frac{k^2}{1 - k^2}. \tag{2.11}$$

2.1.3 Coupling Modes

The separation of charge needed within the piezoelectric element for energy harvesting is due to electric dipole displacement caused by a strain in the material. When loaded, the crystal structure of the piezoelectric material deforms causing an ion to shift within each unit cell of the structure producing charge [31]. Thus each unit cell has an electric dipole which can be re-oriented through pressure to configurable directions. Figure 2.2 illustrates the poling process in a piezoelectric material.

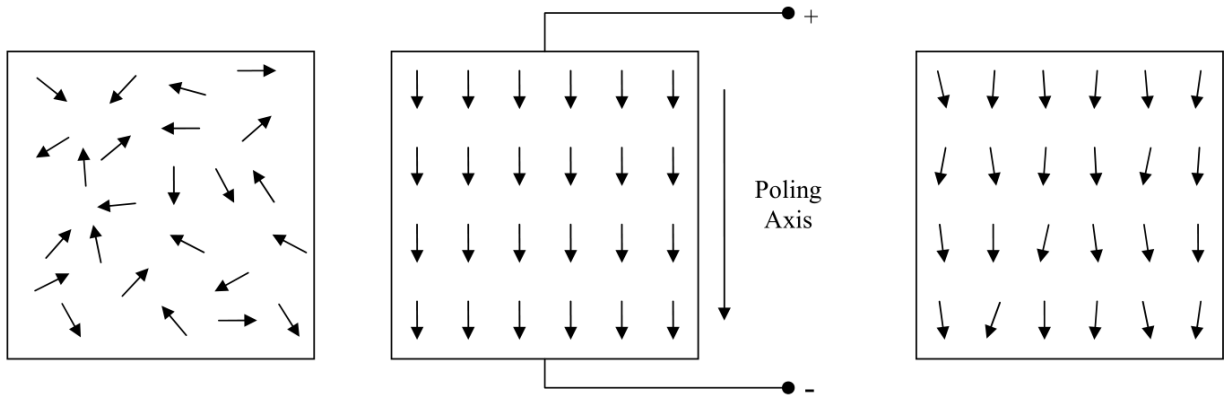

Figure 2.2: Electric dipole orientation before, during, and after poling [32]

Piezoelectric energy harvesters generally involve some method of force or power amplification making their application more attractive. Piezoelectric elements can be stacked together or coupled to a substructure inducing larger strains and producing more electric power. Two common coupling modes arise in application and both lead to the generation of electric charge known as the 31 mode and the 33 mode. Coordinate convention always aligns the poling axis in the three direction with the other coordinate direction representing the direction of mechanical loading. Figure 2.3 illustrates the two common coupling configurations highlighting the axes involved, the direction of poling, and the location of the electrodes.

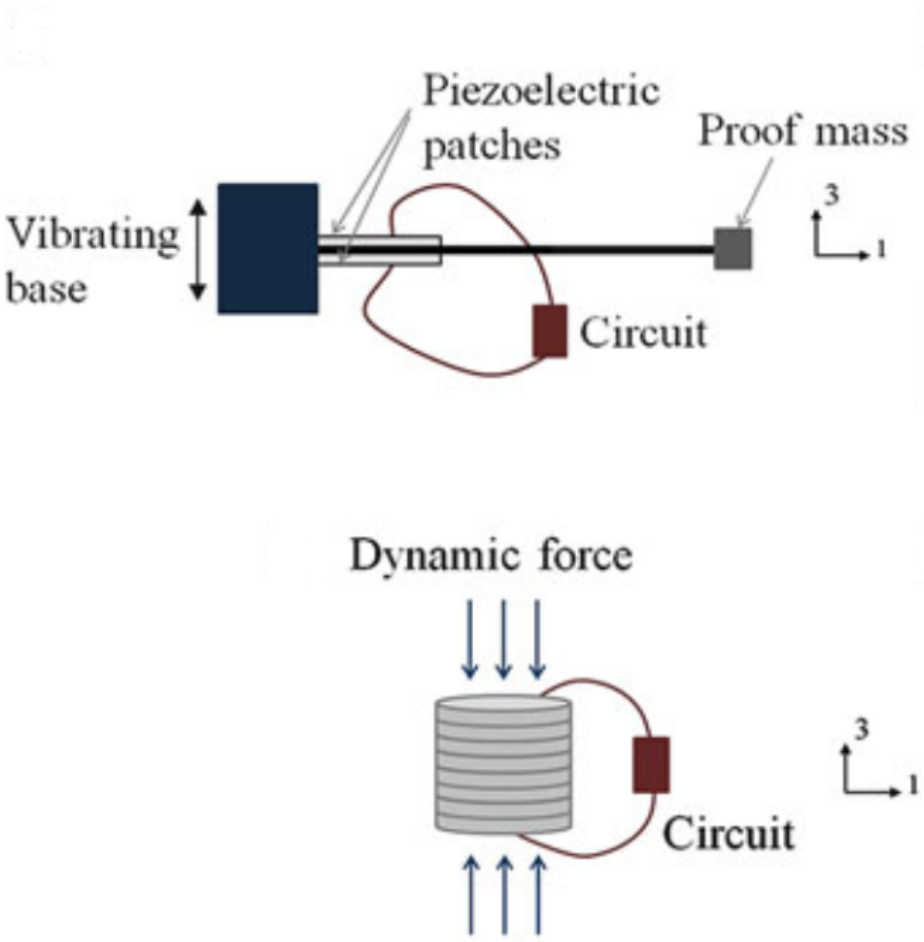

Figure 2.3: Coupling modes of the piezoelectric vibration energy harvesting system [1]

Loading a piezoelectric material through bending is known as the 31 mode, while compressing

a piezoelectric material directly is known as the 33 mode. In the 31 mode, a force is applied in the direction perpendicular to the poling direction, for example by bending a beam with a surface-mounted piezoelectric patch. In the 33 mode, the force is applied in the same direction as the poling direction by compressing a piezoelectric stack. In both cases, the potential difference is observed across the top and bottom surfaces of the piezoelectric material. While the 33 mode yields a higher coupling coefficient, most harvesters utilize the more compliant 31 mode configuration as a larger strain can be imparted with less force due to a lower stiffness of the structure in the loading direction.

2.2 The Cantilever Beam

The prototypical structure for a piezoelectric energy harvester operating in the 31 mode is a cantilever beam. Piezoelectric patches are typically bonded to the area of maximum strain and the addition of a proof mass at the free end of the beam both increases coupling between the mechanical and electrical domains, and reduces the system's fundamental natural frequency. The use of thin beams to maximize deflection leads to systems with inherently low damping and well-separated modes. To identify the resonant frequencies of the beam and thus illustrate the limitation of widespread use of this harvester in application, the force interaction of a differential element of a cantilever beam is shown in Figure 2.4:

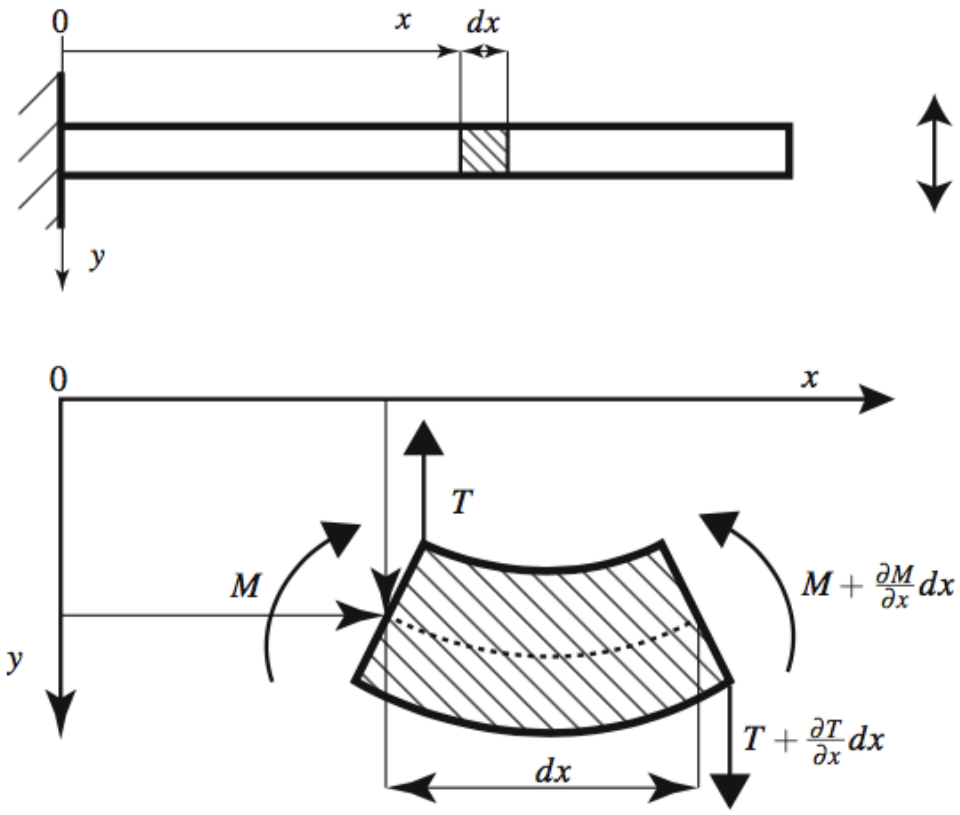

Figure 2.4: A differential element of the cantilever beam for model derivation [33]

Neglecting the effects of rotational inertia and summing the shear forces and bending moments leads to the following equation of motion for each different element of the beam:

$$\begin{aligned} \rho A \frac{\partial^2 y(x,t)}{\partial t^2} &= -T + T + \frac{\partial T}{\partial x} dx \\ 0 &= T\frac{dx}{2} + M + \left(T + \frac{\partial T}{\partial x} dx\right)\frac{dx}{2} - \left(M + \frac{\partial M}{\partial x} dx\right) \end{aligned} \tag{2.12}$$

where ρA is the mass of the element, and $\frac{\partial^2 y(x,t)}{\partial t^2}$ represents the transverse acceleration. Higher order terms can be ignored as their contribution to the solution is insignificant simplifying the

equations of motion:

$$\begin{aligned} \rho A \frac{\partial^2 y(x,t)}{\partial t^2} &= \frac{\partial T}{\partial x} \\ 0 &= T - \frac{\partial M}{\partial x} \end{aligned} \tag{2.13}$$

Since both equations depend on shear force T, the moment equation can be solved and differentiated with respect to x, reducing the system to a single equation capturing all the dynamics [33]:

$$\rho A \frac{\partial^2 y(x,t)}{\partial t^2} = \frac{\partial^2 M}{\partial x^2} \tag{2.14}$$

Curvature, which measures the deflection of the neutral axis indicated by a dotted line in Figure 2.4 allows for the moment M to be described as a relation of (x, y) coordinates and measurable system parameters:

$$\frac{1}{r} \approx \frac{d^2 y}{dx^2} = -\frac{M}{EI} \tag{2.15}$$

Combining the new moment description with Equation 2.14 yields a simplified equation of motion described by (x, y) coordinates and measurable system parameters:

$$\rho A \frac{\partial^2 y(x,t)}{\partial t^2} = -EI \frac{\partial^2}{\partial x^2} \left(\frac{\partial^2 y(x,t)}{\partial t^2} \right) \tag{2.16}$$

Rewriting derivatives with respect to time with dot notation and derivatives with respect to position with roman numeral notation, Equation 2.16 can be expressed in the following compact form:

$$\rho A \ddot{y} + EI y^{iv} = 0 \tag{2.17}$$

Dividing Equation 2.17 by the element mass term ρA and introducing a constant $c = \frac{EI}{\rho A}$ reduces the model further:

$$\ddot{y} + c^2 y^{iv} = 0 \tag{2.18}$$

Equation 2.18 captures the free transverse vibration of a cantilever beam in absence of longitudinal forces and rotational inertia satisfying the assumption of the Euler-Bernoulli beam equation. The major takeaway from this analysis is the evaluation of the beam's resonant frequencies to specifically illustrate the fundamental limitation of energy harvesting with resonant cantilever beams. A general assumption is that the solution will take the form:

$$y(x,t) = a(x)V(t) \tag{2.19}$$

separating the spacial and time dependent components of the system. Substituting the solution form into Equation 2.18 leads to a new equation of motion:

$$\frac{a^{iv}}{a} = -c\frac{\ddot{V}}{V} \tag{2.20}$$

Since each side of the equation is independent of the other side, both must equal a constant (Ω^2) allowing for variables to be separated into two ordinary differential equations:

$$\begin{aligned} a^{iv} - \frac{\Omega^2}{c}a &= 0 \\ \ddot{V} + \Omega^2 V &= 0 \end{aligned} \tag{2.21}$$

A new constant $\nu^4 = \frac{\Omega^2}{c}$ is introduced to simplify notation. The solution of the spacial equation is assumed to take the form:

$$a(x) = Ae^{rx} \tag{2.22}$$

resulting in a characteristic equation having the following roots:

$$r_{1,2} = \pm\nu \qquad r_{3,4} = \pm j\nu \tag{2.23}$$

Expanding leads to the spacial solution:

$$a(x) = A_1 e^{\nu x} + A_2 e^{-\nu x} + A_3 e^{j\nu x} + A_3 e^{-j\nu x} \tag{2.24}$$

Euler's formula for trigonometric relations:

$$\begin{aligned} e^{\pm j\nu x} &= \cos \nu x \pm j \sin \nu x \\ e^{\pm \nu x} &= \cosh \nu x \pm \sinh \nu x \end{aligned} \tag{2.25}$$

are used to remove the exponentials in the spacial solution:

$$a(x) = C_1 \cosh \nu x + C_2 \sinh \nu x + C_3 \cos \nu x + C_4 \sin \nu x \tag{2.26}$$

Constants C_1, C_2, C_3, C_4 are constants of integration determined by the boundary conditions of the problem. Using the typical boundary conditions for a clamped cantilever beam fixed at one end and free at the other:

$$\begin{aligned} y(0,t) &= 0 \qquad & y^{ii}(l,t) &= 0 \\ y^{i}(0,t) &= 0 \qquad & y^{iii}(l,t) &= 0 \end{aligned} \tag{2.27}$$

leads to the following relations solving for the constants of integration:

$$\begin{aligned} C_1 + C_3 &= 0 \\ \nu(C_2 + C_4) &= 0 \\ \nu^2 \left(C_1 \cosh \nu x + C_2 \sinh \nu x - C_3 \cos \nu x - C_3 \sin \nu x\right) &= 0 \\ \nu^2 \left(C_1 \cosh \nu x + C_2 \sinh \nu x + C_3 \cos \nu x - C_3 \sin \nu x\right) &= 0 \end{aligned} \tag{2.28}$$

A nonzero ν implies that $C_3 = -C_1$ and $C_4 = C_2$, and reduces the equations above to:

$$\begin{aligned} (\cosh \nu l + \cos \nu l)\, C_1 + (\sinh \nu l + \sin \nu l)\, C_2 = 0 \\ (\sinh \nu l - \sin \nu l)\, C_1 + (\cosh \nu l + \cos \nu l)\, C_2 = 0 \end{aligned} \tag{2.29}$$

To prevent nontrivial solutions, the following frequency equation must be obeyed:

$$\cos \nu l \cosh \nu l + 1 = 0 \tag{2.30}$$

Therefore, the resonance frequencies are based off the constant ν^4, the roots of Equation 2.30 and [33]:

$$\Omega_n = (\nu_n l)^2 \sqrt{\frac{EI}{\rho A l^4}} \tag{2.31}$$

Solving numerically yields the first few roots as $\nu_1 l = 1.875$, $\nu_2 l = 4,694$, $\nu_3 l = 7.855$, and $\nu_4 l = 10.9955$. Simple inspection of Equation 2.31 shows a spacing between natural frequencies of $\Omega_2 = 6.27\Omega_1$, $\Omega_3 = 17.55\Omega_1$, and $\Omega_4 = 34.39\Omega_1$. For example, this means that if ambient vibration around a harvester is 25 Hz ($\Omega = 157$ rad/sec) and the harvester is tuned to this frequency (i.e., $\Omega_1 = \Omega$), the second mode of vibration will exist at 157 Hz ($\Omega_2 = 985$ rad/sec). With natural frequencies so well-separated, neighboring modes do not influence each other; therefore only the first mode is ever captured during excitation. Excitation of a single mode under normal operation illustrates the resonance limitation inherent to cantilever-based piezoelectric energy harvesters.

The well-separated modes present in a cantilever beam harvester allow the system to be represented by an equivalent, but simpler, lumped parameter model. Reduction to a single degree of freedom system simplifies computation allowing the system to be adequately represented by a mass-spring-damper model coupled to a capacitive electric circuit capturing the effects of beam displacement on energy harvesting. The lumped parameter derivation is reserved for Section 3.1 as it directly frames the proposed nonlinear harvesting technique. Instead, the main takeaway from the dis-

tributed parameter derivation is the resonance limitation that cripples performance of traditional piezoelectric energy harvesters in time-varying ambient environments.

2.3 Energy Harvesting Improvements

Chapter 1 broadly described the different areas of research and the limitations therein of the current state of piezoelectric energy harvesting. From shape variations of the cantilevered beam to harvesting circuits that charge a capacitor until a peak voltage is reached, the techniques aim to better use a harvester in its resonance excitation implementation.

2.3.1 Improvements through Beam Configuration

For energy extraction, a cantilevered configuration is most common for piezoelectric harvesters. Improvements of the cantilevered harvester have been approached through a variety of angles to improve each individual aspect of the device. While typically rectangular, cantilever beams easily allow flexibility in geometrical shape. Altering this shape between a trapezoidal beam, a triangular beam, and an initially curved beam provides multiple avenues for improving beam deflection under lower forces correlating to a larger strain [34–38].

Placement of the piezoelectric material also plays an important role in harvester efficiency. Typically, one piezoelectric element is placed in the area of maximum strain on the beam. Using a single piezoelectric element is commonly known as a unimorph configuration. During bending, the beam deflects in both positive and negative directions; therefore an alternate bimorph configuration involves placing piezoelectric elements on both sides of the beam [39–42].

Inherent to each beam is a corresponding natural frequency that should ideally match the ambient

environment. By adding mass to the tip of the beam, a way of tuning the natural frequency was made possible without changing the entire harvesting system [43]. Pre-stressing the cantilever beam also proved beneficial as a baseline stress ensured a larger charge separation during loading [44].

All of the above methods improve power output at resonance. To combat this bandwidth limitation, research has addressed both tuning the resonance frequency to match that of the ambient vibrations and developing devices with more than one resonant state. A passive high-bandwidth system has been developed using an array of cantilevered harvesters, each tuned to a different resonant frequency [45, 46]. Linear cantilever configurations require resonance excitation because the modes of vibration are well separated. Working to reduce the separation, an L-shaped cantilever configuration was investigated. This design created two closely-spaced natural frequencies resulting in a higher bandwidth harvester [47–49].

Work with respect to geometry and configuration successfully created harvesters yielding larger power outputs, but did not solve the resonance excitation requirement. Even though bandwidth improvements were observed, they were achieved at the expense of initially tuning to a natural frequency. Also, further design improvements through methods of extracting and storing the electric charge were overlooked in the approaches mentioned above.

2.3.2 Improvements through Circuitry and Power Storage

Shifting from the mechanical side of the process, researchers have also focused on modifying the power harvesting circuitry and storage medium. When loading a cantilevered harvester, continuous charge extraction does not result in any meaningful amount of power. Realizing the instantaneous power generated by a harvester was too small for any practical application, circuits were designed to store energy and release it in bursts. Energy was stored in a capacitor until a release voltage

was reached, discharging the capacitor into a load [41, 42]. Improvements to this circuit were made through component changes and the introduction of DC converters [50–56]. Combining both mechanical and electrical modifications, harvesters were developed that diverted some power to sense the ambient frequency and modify the stiffness of the cantilever beam [57].

Electrical improvements are important because once high bandwidth harvesters are created, sufficient charge extraction methods need to exist in parallel to capture the largest amount of energy. Unfortunately, circuit improvements fail to solve the original bandwidth problem plaguing piezoelectric materials. A complete solution to the problem needs to embrace both avenues of improvement from the previous sections, but also eliminate the dependence on resonance excitation and maintain a small footprint.

2.3.3 Improvements through Induced Nonlinearities

A viable method to extend progress further towards the creation of high-bandwidth energy harvesters involves forcing the linear harvester to embrace nonlinear dynamics. By placing the typical cantilevered harvester in a magnetic field, the central equilibrium of the potential function destabilizes, shifting the governing dynamics of the system to a bistable Duffing oscillator.

Progress has been made toward developing a non-resonant piezomagnetoelastic energy harvester and investigating high-energy periodic orbits over a range of excitation frequencies [19, 58]. The resulting system was modeled by the nonlinear bistable Duffing oscillator modified to account for piezoelectric coupling. Experimental measurements showed considerably larger oscillation amplitudes with greater bandwidth than its linear piezoelastic counterpart and a corresponding increase in harvested energy. These results are promising, but still do not reach the full potential of an actively controlled counterpart.

The works cited thus far either only address improvements at resonance excitation, result in clunky ways of mitigating the resonance requirement, or do not exploit nonlinear behavior to their fullest potential. This work aims to improve the bandwidth of the harvester with little expense to power output throughout the operating region. By accepting chaos as a desirable property, small perturbations to a manipulable system parameter can greatly alter the behavior of a system. This extreme sensitivity to initial conditions can allow small control inputs to have large effects on state trajectories and power output. Extending the nonlinear piezomagnetoeleastic beam element described by a Duffing oscillator in Figure 1.6 to embrace chaotic motion more actively can improve the bandwidth of the harvester without compromising harvested energy. Driving motion along a chaotic attractor allows a single excitation frequency to generate a theoretically infinite number of unstable periodic orbits that can be stabilized through control. Ergodic wandering of a chaotic orbit over its strange attractor eventually brings the trajectory arbitrarily close to every unstable period orbit in the attractor [59]. Since each single excitation frequency creates an infinite number of orbits, some overlap is expected with multiple frequencies containing the same orbit in space. The chosen orbit can be accessible from a large range of input excitation frequencies improving the bandwidth of the piezoelectric harvester. Embracing chaotic motion will allow development of a novel harvester able to work across a large range of excitation frequencies, both harmonic and non-harmonic.

Chaotic motion in conjunction with a low-power controller can drive the system through a wider range of trajectories as opposed to the more limited motion captured by linear models [60]. By studying the nonlinear dynamics of said chaotic system, it becomes possible to trap the harvester through feedback in a chosen orbit for energy extraction [59]. As such, a high bandwidth harvester can be created by developing feedback controllers for an unstable periodic orbit within the chaotic attractor.

2.4 The Duffing Oscillator

Classically, the Duffing oscillator is a well researched system of nonlinear dynamics. Famous for its use in studying non-harmonic oscillations and chaotic nonlinear dynamics, the equation was developed by the German engineer Georg Duffing [61]. While the Duffing oscillator is versatile among its applications, it is used herein to model the vibration of a buckled piezomagnetoelastic beam.

To visualize the the effects of nonlinearity on the frequency response of a Duffing oscillator, it is useful to start with the system representation in absence of any electromechanical coupling [62].

$$\ddot{x} + \delta\dot{x} + \alpha x + \beta x^3 = \gamma\cos(\omega t) \tag{2.32}$$

where δ represents the mechanical damping ratio, α and β together represent the effect of the nonlinear spring force, γ is the forcing amplitude, and ω is the harmonic excitation frequency. Applying the method of harmonic balance, a solution to Equation 2.32 is assumed in the following form:

$$x = a\cos(\omega t) + b\sin(\omega t) = z\cos(\omega t + \phi) \tag{2.33}$$

where $z^2 = a^2 + b^2$ and $\tan\phi = \frac{b}{a}$. Differentiation and substitution of Equation 2.33 into Equation

2.32 leads to:

$$\begin{aligned}\left(-\omega^2 a + \omega\delta b + \alpha a + \frac{3}{4}\beta a^3 + \frac{3}{4}\beta a b^2 - \gamma\right)\cos(\omega t) \\ + \left(-\omega^2 b - \omega\delta a + \frac{3}{4}\beta b^3 + \alpha b + \frac{3}{4}\beta a^2 b\right)\sin(\omega t) \\ + \left(\frac{1}{4}\beta a^3 - \frac{3}{4}\beta a b^2\right)\cos(3\omega t) \\ + \left(\frac{3}{4}\beta a^2 b - \frac{1}{4}\beta b^3\right)\sin(3\omega t) = 0\end{aligned} \tag{2.34}$$

Similar to the distributed parameter cantilever beam model, higher order terms and harmonics can be neglected as they pose little impact to the system response. As a result, a nontrivial solution exists when the coefficients of $\sin(\omega t)$ and $\cos(\omega t)$ are independently zero:

$$\begin{aligned}-\omega^2 a + \omega\delta b + \alpha a + \frac{3}{4}\beta a^3 + \frac{3}{4}\beta a b^2 = \gamma \\ -\omega^2 b - \omega\delta a + \frac{3}{4}\beta b^3 + \alpha b + \frac{3}{4}\beta a^2 b = 0\end{aligned} \tag{2.35}$$

Squaring both equations and adding them together results in the magnitude function of the frequency response:

$$\left[\left(\omega^2 - \alpha - \frac{3}{4}\beta z^2\right)^2 + (\delta\omega)^2\right] z^2 = \gamma^2 \tag{2.36}$$

Depending on the sign of the variable spring force, a softening or a hardening Duffing oscillator can result. In each case, the tip of the magnitude plot bends left or right, respectively, and gives initial insight to the coexisting dynamic attractors that can arise during excitation of a Duffing oscillator system. Figure 2.5 illustrates the frequency response of both softening and hardening Duffing oscillators compared to the linear lumped parameter beam model. Nonlinear harvesters aim to eliminate the resonance excitation dependence, while also allowing for efficient operation in low frequency ambient environments. Therefore, a softening harvester is the system of choice,

with a theoretically larger magnitude than an equivalent linear system, wider operating bandwidth, and optimal performance below the resonance frequency.

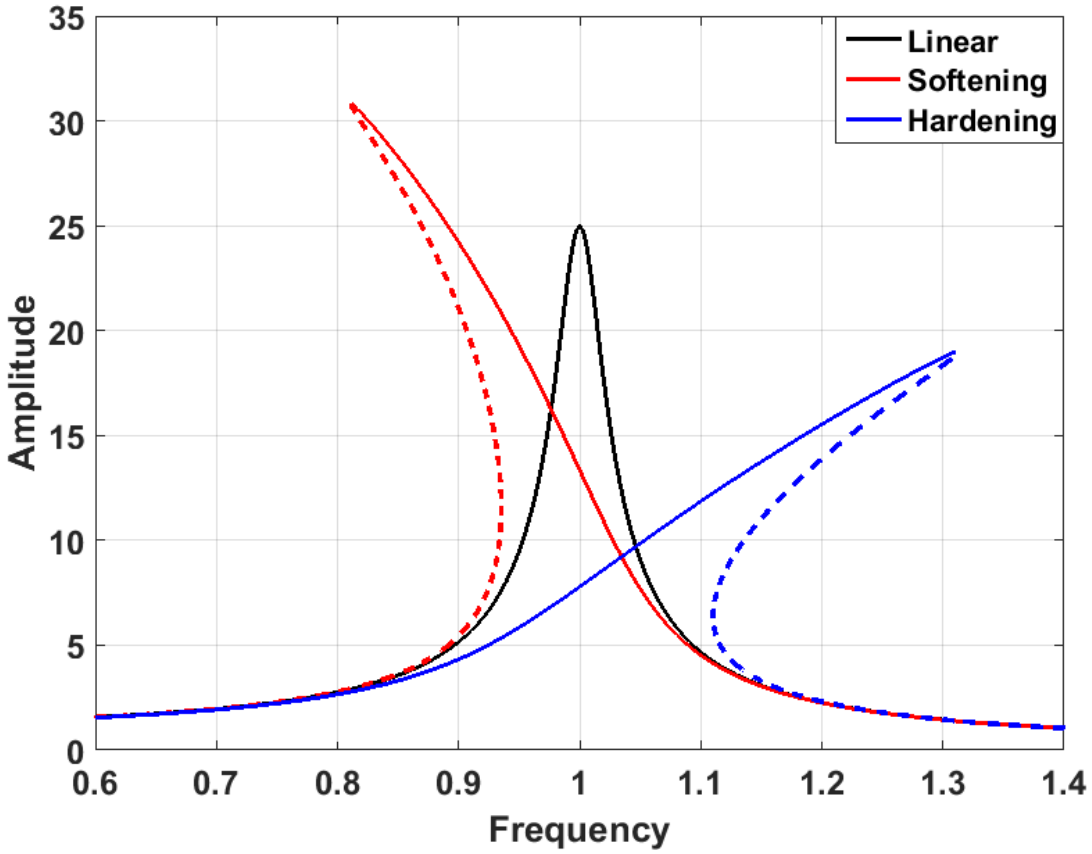

Figure 2.5: Frequency response of the Duffing oscillator

2.4.1 Multistability of the Duffing Oscillator

The bending of the frequency response coincides with the the destabilization of the central equilibrium point caused by the nonlinear restoring spring force in the Duffing oscillator. The direction of the frequency sweep dictates on which branch of the response the system will oscillate. These branches correlate to what are commonly called the dynamic attractors of the system. In addition

to the sweep direction, environmental disturbances can also cause the solutions to jump or fall between the branches [62].

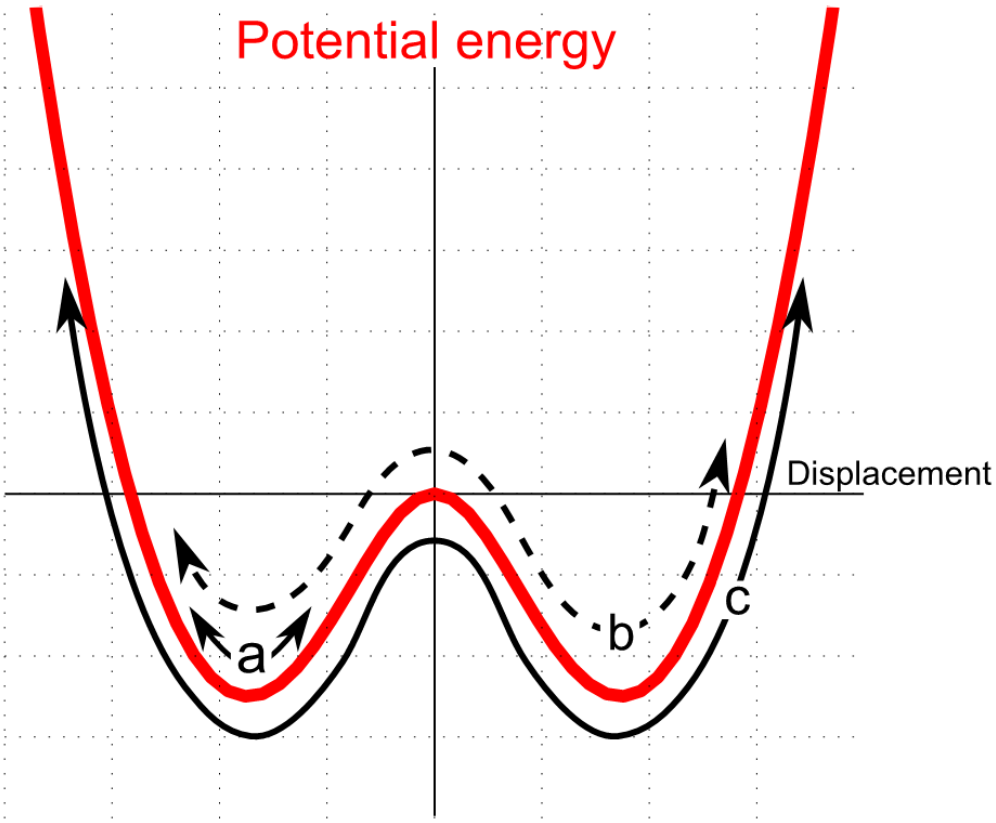

Figure 2.6: A bistable potential function labeled with the possible dynamic attractors [15]

Figure 2.6 more readily illustrates both the destabilized central equilibrium caused by the nonlinearity and the solution branches from a potential function perspective dependent on the excitation energy available in the ambient environment. Under low-energy ambient environments, the trajectories remain in a single well (a) with small periodic solutions inefficient for suitable energy harvesting. Increasing the excitation energy further leads to aperiodic chaotic solutions (b) dominating the response. In chaotic motion the system experiences enough energy to bounce between potential wells, but at an irregular rate. These solutions are different from random motion, in that they exist in a finite region of the phase space as illustrated by the outer bounds of the potential function. Increase the excitation even further and a large-amplitude, periodic interwell solution

(c) dominates the response. With respect to nonlinear vibration energy harvesting with a bistable system, this has been considered the ideal response for optimal performance [15, 16].

Figure 2.7 takes the solution branches illustrated in both Figures 2.5 and 2.6 and depicts them as a phase portrait highlighting the displacement differences between solutions. The outer line (c) is the desirable large displacement orbit. Region (d) and trajectory (b) represent the chaotic attractor and a possible stable periodic orbit within. Trajectory (a) illustrates the poor performance of an equivalent linear harvesting system operating away from its fundamental frequency. A combination of the three figures paints a clear picture of the physical responses possible for each dynamic attractor, and the energy differences presented when considered from the perspective of vibration energy harvesting.

The phase portrait in Figure 2.7 visualizes the types of responses possible, but does not adequately capture the notion that these responses can coexist for a range of system parameters. Bifurcations used to illustrate what dynamics attractors are present for a range of system parameters is addressed in more detail in Section 3.2 once the proper analytical tools are developed. Chaotic oscillations and the large amplitude orbits can both dominate the response, with the final solution depending on initial conditions or disturbances over time. When these instances arise, it is typical to disregard chaos and hope the large amplitude solution wins out. Contrary to common practice, chaos can be a highly beneficial property of an energy harvesting system. The stretching and folding of trajectories in the state space due to the existence of both stable and unstable manifolds gives chaotic systems an extreme sensitivity to variations in parameters and initial conditions. Before any design decisions can be made regarding the chaotic solution, a new set of analysis tools is needed to visualize the system, breaking from the traditional framework of a deterministic analytical solution. The next few sections quantify how chaotic motion is beneficial and provide an explanation of the analytical tools and control ideologies that will be used.

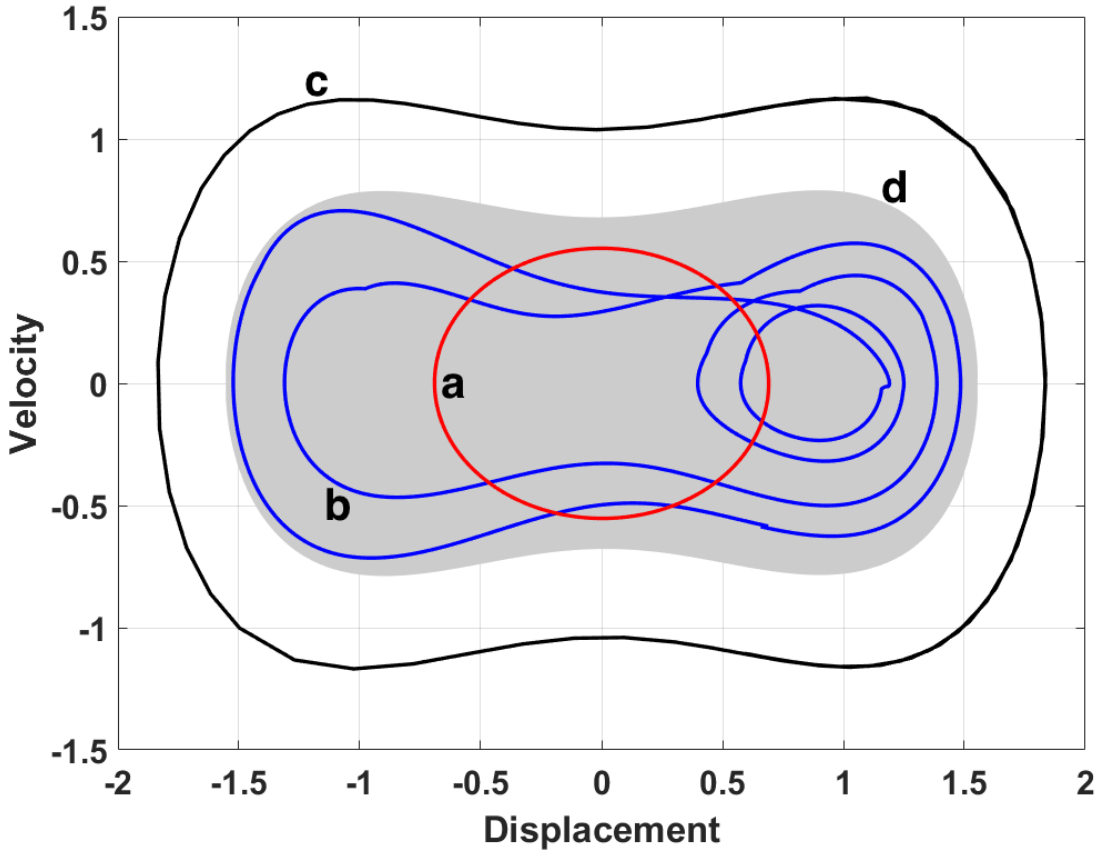

Figure 2.7: Phase portrait comparisons of the common attractors in a bistable energy harvester [63]

2.5 Visualizing Chaotic Systems for Control Design

When solving harmonically forced linear systems of the form $m\ddot{x} + c\dot{x} + kx = F_0 \sin \omega t$, it is often a trivial task to determine key values of damping ratio and natural frequency. Typically a differential equation solver can plot solutions of the form seen in Figure 2.8 and represented by Equation 2.37:

$$x(t) = Ae^{-\zeta_n \omega_n t} \sin(\omega_d t + \phi) + \frac{F_0}{k} \frac{1}{(1-r^2)^2 + (2\zeta_n r)^2} \sin(\omega t + \psi) \tag{2.37}$$

where r represents the ratio of excitation frequency to natural frequency and $\omega_d = \sqrt{1-\zeta_n^2}$ represents the damped natural frequency.

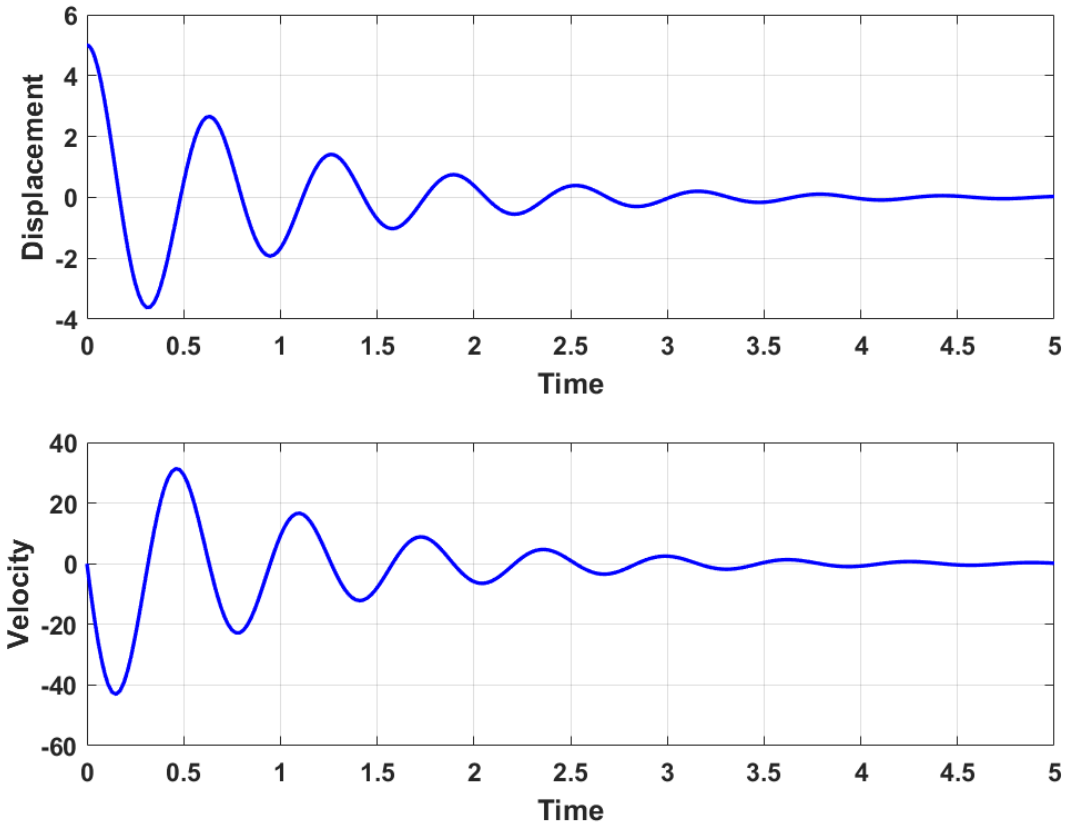

Figure 2.8: Time series solution of a forced linear mass-spring-damper system

Multistability is not possible in linear systems and damping ratio, natural frequency, and excitation frequency can all be interpreted directly from the plot. However, when representing solutions for nonlinear and chaotic systems, it is often impossible to discern significant information from a time domain solution. For example, no distinct pattern or trend exists in the time series solution of the Duffing oscillator exhibiting chaotic motion. Worse still, identical systems occupying the same chaotic attractor can exhibit substantially different solutions from each other due to the extreme sensitivity to initial conditions. Figure 2.9 illustrates the solution of two identical Duffing oscillators. One oscillator was given initial conditions of $(1, 0)$ for displacement and velocity, respec-

tively. The second oscillator was started at $(1.01, 0)$. The solutions remain identical for roughly thirty seconds before traversing highly different trajectories within the same bounded space even though the same chaotic attractor is present in both oscillators as seen in Figure 2.10.

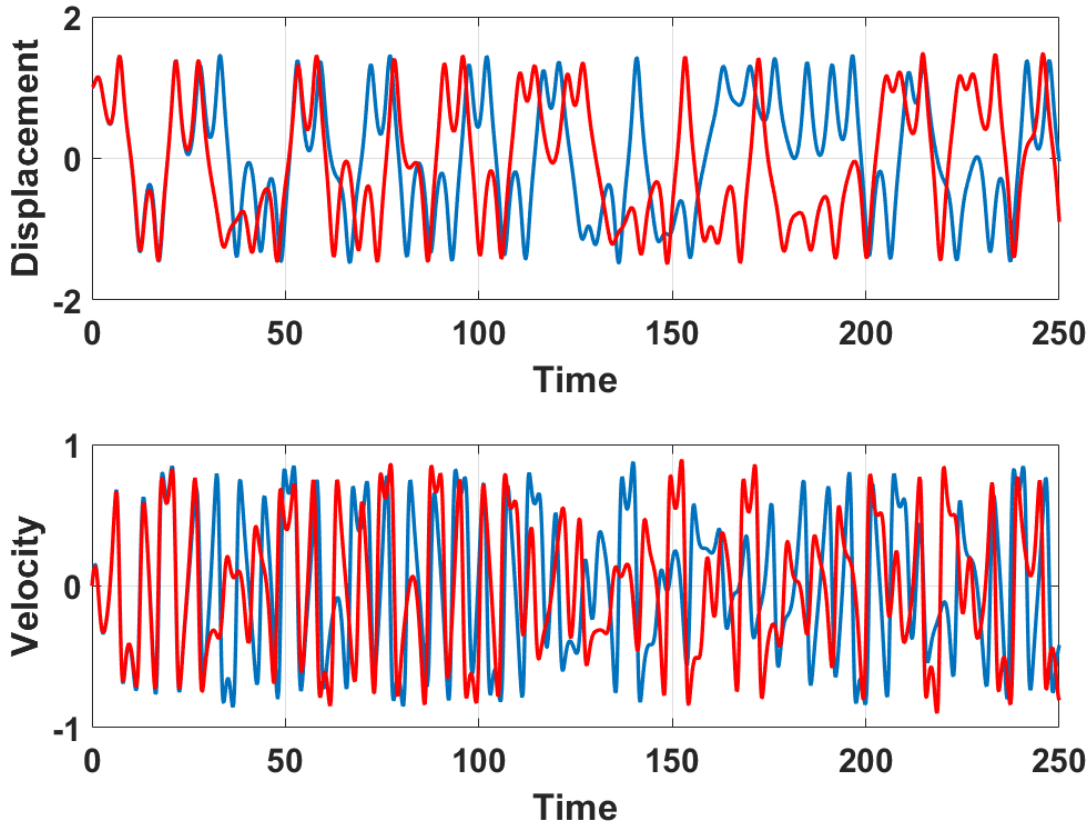

Figure 2.9: Time series solutions of identical Duffing oscillators started from slightly different initial conditions

Successful control of the chaotic system hinges on the ability to isolate useful quantities related to periodicity and stability of the system. While time series plots of the system trajectories are often useless at best, alternative analysis techniques have been investigated in the literature, allowing some conclusions to be made about chaotic systems. The stretching and folding of the trajectories in the state space previously mentioned frame the idea that a chaotic attractor is a dense sea of infinitely many unstable periodic orbits. One method of visualizing these orbits is called the

Poincaré section.

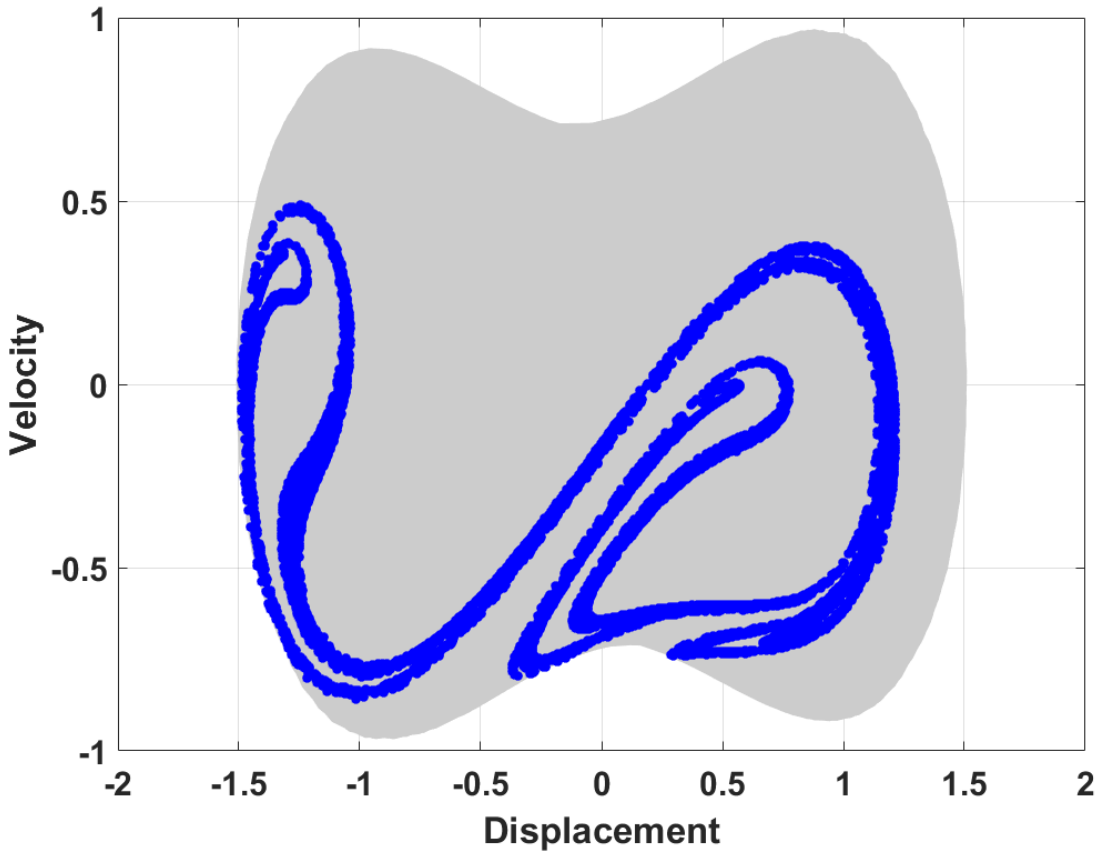

Figure 2.10: Phase portrait and Poincaré section of the Duffing oscillator illustrating the chaotic attractor

2.5.1 Poincaré Sections

In systems exhibiting periodic or quasi-periodic behavior, it becomes beneficial to illustrate the system as a reduced dimensional mapping transverse to another dimension of the system. The resulting plot is then defined as a map of points every time the trajectories either cross the same plane in space, or cross a plane in time with periodic multiplicity. This method is known as a Poincaré map and was developed in 1899 by Henri Poincaré [64]. This discrete map decreases dimensionality to $(n-1)$ while still capturing important dynamical phenomena like periodicity

and stability. Therefore, a Poincaré map allows complex dynamic behavior to be clearly observed for general periodic trends.

Poincaré maps can be generated for spatial and time varying functions, but the total system dimension must be greater than or equal to three. As Duffing oscillators are driven by a time-dependent harmonic function, the latter approach is used in generating a section. Freedom exists to choose a map starting at any time τ within the first period, T, of the system. Then, as the trajectory progresses, a data point is taken at every time $\tau + nT$, when n is an integer from $0, 1, \ldots, n$. Theoretically, a Poincaré map is described by the following equation:

$$x_{k+1} = Px_k \tag{2.38}$$

though it is often impossible to explicitly describe the relation for P. The Poincaré map in Figure 2.11 illustrates that consecutive points traversing through an identical plane from X_n to X_{n+1} involve the analytical mapping P, and motion from X_n to X_{n+2} is described by P^2.

The Poincaré map is exceptionally useful when used on unknown systems suspected of exhibiting periodic behavior. As a tool it can readily display if a solution is periodic as well as the period of said solution, or if more complex chaotic and random behavior is present. Since a map can be created solely from discrete time series states of the system, simple characterization between chaotic and non-chaotic behavior can be made. However, the map by itself does not dictate enough information to develop a control algorithm for the system. The points in the Poincaré map illustrate the location of unstable periodic orbits with the chaotic attractor, with large time horizons providing adequate insight into the bounds of the attractor itself. Unfortunately, the period of each orbit point is still unknown, nor is there any method to find the other points for orbits greater than period-1. Isolating a single dimension of the Poincaré map and plotting a current point against a future point $n + p$ periods later allows the diagonal line $x_n = x_{n+p}$ to be used as a visual classifier for orbits

of that period. Such a plot is called a return map and will be described in Section 3.2. Creating a robust controller requires developing an automated solution that can isolate orbit points of various periods. Using recursive techniques, such an algorithm was developed and will be explained in the following chapter. Once orbit points are isolated, a chaotic controller can be implemented.

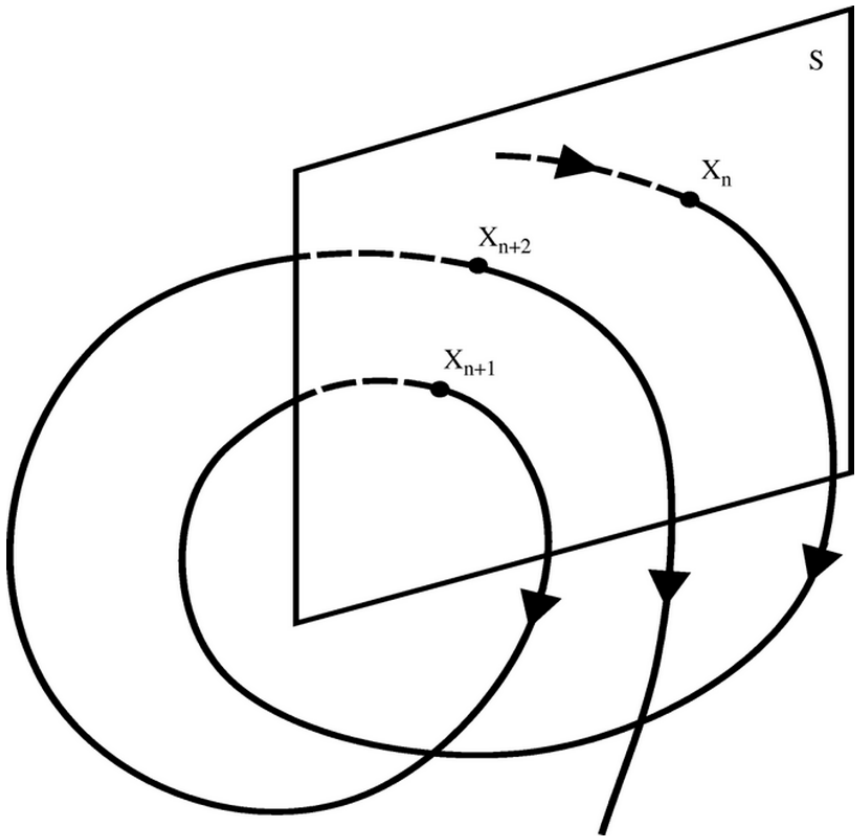

Figure 2.11: Dimensional reduction for computing a Poincaré section

2.6 Chaos Control Methods

Chaos control for piezoelectric-based vibration energy harvesting systems seeks to isolate unstable periodic orbits within the chaotic attractor and generate stable periodic trajectories capable of producing a net larger power output of the system than aperiodic chaotic oscillation alone. To do so while embracing the sensitivity to variations in parameters, local linear models are fit in the

vicinity of each of the isolated unstable periodic orbit points. From these models, control gains are computed depending on the algorithm chosen; these gains aid in perturbing the system onto the stable manifold of the isolated periodic orbit. A caveat of this control approach is the wait time associated for the trajectories to wander sufficiently close to the isolated orbit points for the local linear controller to be valid. While ergodicity of the attractor ensures all unstable orbits points are visited in finite time, this time cannot be quantified and is different between attempts. Also, once control is applied the perturbations must be repeated upon each passing of the trajectory preserving stability as the trajectory then remains along the stable manifold. Two different control techniques were developed using discrete data and a third, model-dependent method was implemented to investigate the success of a control law capable of perturbing the system between attractors.

2.6.1 Ott, Grebogi, and Yorke Control

Derived with the notion that chaotic motion is the result of an infinite number of unstable periodic orbits in the phase portrait, Ott, Grebogi, and Yorke theorized that a well-chosen small perturbation to a parameter within the nonlinear system could allow periodic orbits of any period to be stabilized within a finite number of iterations [20]. Computing this parameter stems from the two-dimensional phase portrait and Poincaré section constructed to isolate the unstable m-periodic orbit points. Fitting a local linear model to each orbit point is equivalent to computing the Jacobian of the system with eigenvalues representing the stable and unstable manifold for each point. Note that a two-dimensional chaotic system is guaranteed to have one stable and one unstable direction, and this is the only condition on which OGY control works.

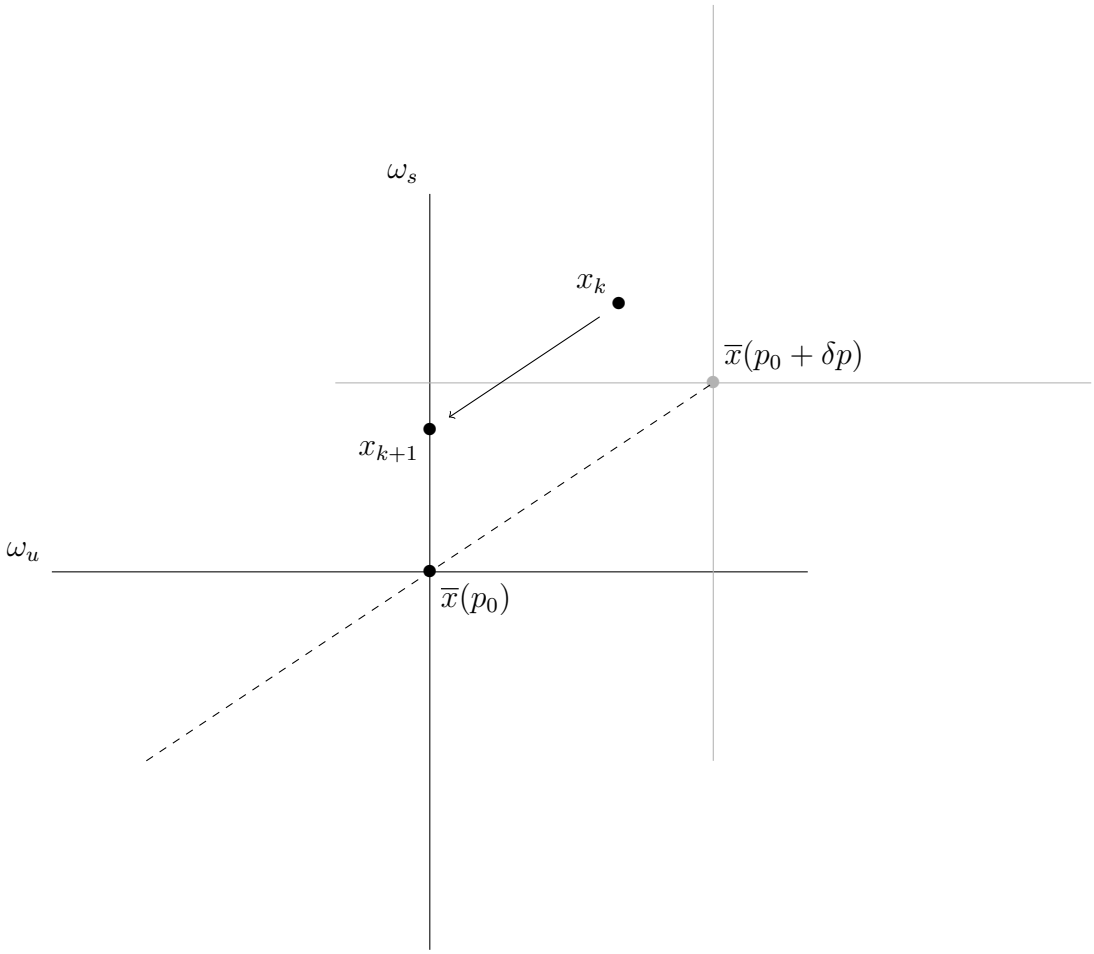

Figure 2.12: Stabilizing an unstable periodic orbit point with OGY control

The OGY control approach illustrated in Figure 2.12 is centered around the idea that an accessible parameter within the system can be perturbed, forcing a point in the neighborhood of $\overline{x}$ onto the stable manifold. The value of p_0 represents the steady state value of the accessible parameter. The point x_k is chosen in the neighborhood of the fixed point with the dotted line representing the path it can be shifted along through perturbation. Once x is perturbed to $(p_0 + \delta p)$, the next iteration forces point x_k to be both attracted to $\overline{x}(p_0 + \delta p)$ parallel to its stable manifold and repelled from $\overline{x}(p_0 + \delta p)$ parallel to its unstable manifold. Proper choice of perturbation δp causes x_{k+1} to fall directly onto the stable manifold of $\overline{x}(p_0)$. The parameter can then be returned to its nominal value p_0 as the periodic orbit will remain stable until the next cycle.

2.6.2 *Sliding Mode Control*

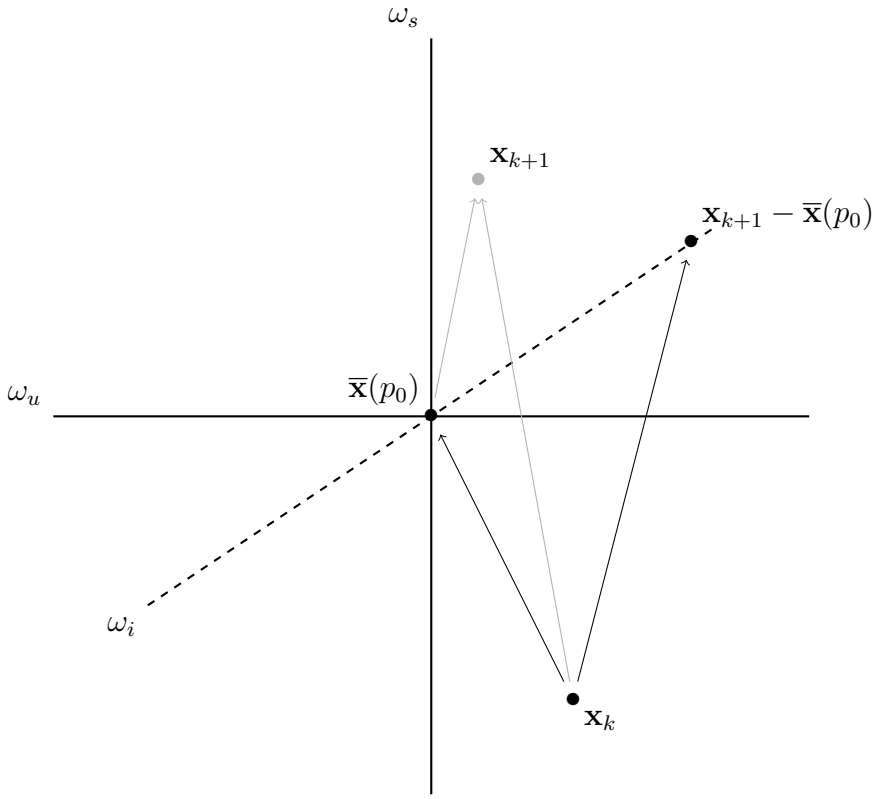

Figure 2.13: Stabilizing an unstable periodic orbit point with sliding mode control

A weakness of the OGY algorithm is its reliance on both the ability to compute the system Jacobian for the chaotic system and the existence of a single unstable manifold direction. For higher-dimensional systems computing a Jacobian is computationally challenging and can lead to multiple unstable manifold directions for a single orbit point. The two-dimensional bistable system used is linearly coupled to a capacitive circuit representative of the harvesting element; introducing another dimension to the system. Therefore, an alternative algorithm was implemented independent of a system Jacobian and robust when considered for higher-dimensional chaotic systems. Whereas the OGY controller prescribed perturbations to shift trajectories along the unstable manifold onto the stable manifold, the sliding mode controller prescribes a custom manifold designed to intersect the stable manifold of the orbit point. Shown in Figure 2.13, perturbations made by the sliding mode

controller do not push the system directly onto the stable manifold of the orbit point. Instead, the trajectory gets pushed into a custom manifold designed to intersect the stable manifold.

2.6.3 Control Across Attractors

Mentioned repeatedly in the literature and earlier sections of this work, the ideal orbit for energy harvesting is pure interwell motion in which the system does not get trapped in either potential well. The above control strategies aim to stabilize interwell trajectories, but these orbits lie within the low energy attractor. Conceptually, re-framing the problem in which isolated orbit points exist in a different attractor altogether, the same control strategy can be implemented with the end result being control across attractors from low energy to high energy. In a method adapted by Liu et al., the bistable harvester system model is solved in parallel to a theoretical model tracking the large amplitude trajectory. The difference between the results is framed as an error to be minimized using control. Contrary to the previous methods, this method cannot presently be done from discrete time series data.

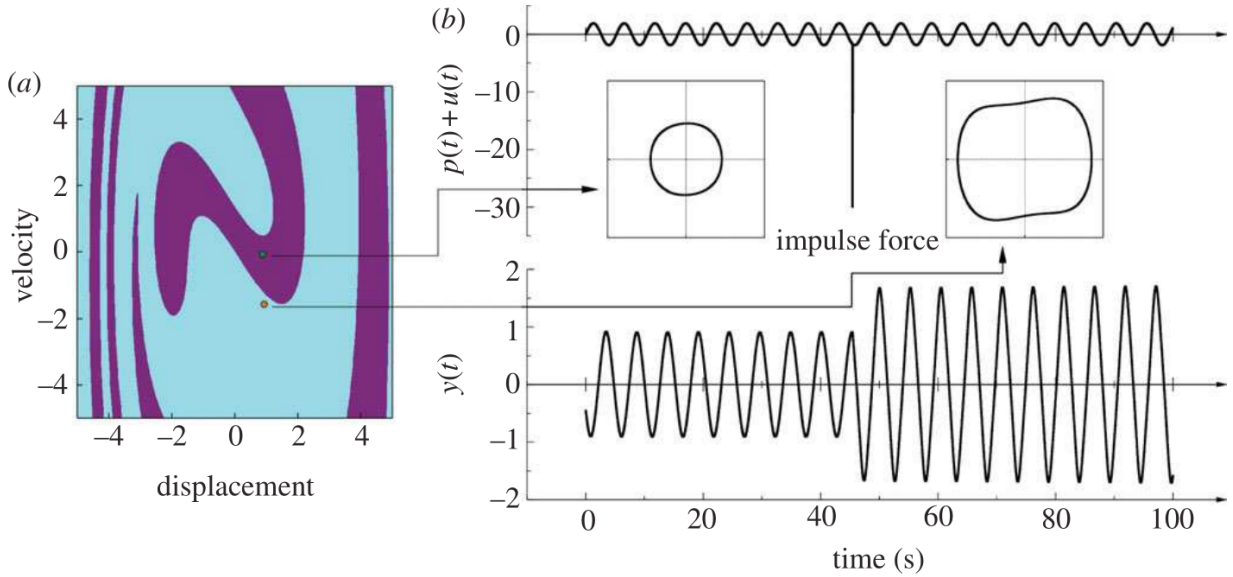

Figure 2.14: Stabilizing trajectories across attractors with a model-based feedback controller [65]

Previous work by Liu et al. has demonstrated the feasibility of an intermittent controller for a classic Duffing oscillator system. Two period-one attractors of small and large amplitude exist concurrently for a specific set of system parameters. The goal of the control algorithm is to minimize the error between the current state in the lower-energy attractor and the desired state in the high-energy attractor for both position and velocity. As the required perturbation is small, a local linear controller is designed near the intersection of the two concurrent attractors. The event-driven, intermittent application of the control law prevents unwanted changes to the underlying dynamics or attractors of the system [65]. When a perturbation is intermittently applied to a state of the system, the system is adjusted onto the higher-energy attractor thus resulting in a larger displacement for the harvester. The same ideology is preserved in the nonlinear harvesting application; however, the starting attractor is chaotic and the periodic large amplitude attractor is stabilized through perturbation.

The proposed design induces chaotic motion through nonlinearity of the piezoelectric-based vibration energy harvester. Time series data from the chaotic motion can be used to isolate points from a dense sea of unstable periodic orbits and fit a control law resulting in stable, large-displacement trajectories of the system. The result is a harvester capable of operating away from resonance with an optimal solution existing across a wide band of frequencies present in an ambient environment. The rest of this dissertation is aimed at assembling the chaotic system and successfully stabilizing large-displacement trajectories of the system; both theoretically and experimentally.

CHAPTER 3: MODEL DEVELOPMENT

The background covered in Chapter 2 frames the harvesting problem, extends the technology towards induced nonlinearity for bandwidth improvements, and details the dynamic solutions present in the system. The strength of the proposed control method is model independence as parameters are fit from time series data of the system. This chapter derives a lumped parameter model for the prototypical bistable energy harvester to then use time series data with the topological mapping techniques for analyzing chaotic systems. Orbit points are isolated using a statistical recurrence technique and a local linear model is then fit within the vicinity of each point for control. State reconstruction is described, reducing the measurement requirements to a single state of the system; i.e. displacement. Additionally, the model-based feedback control method designed is capable of improving the harvesting system further by perturbing the system out of the lower energy chaotic attractor and onto the desirable large amplitude response.

3.1 Bistable Piezoelectric Energy Harvesting Model

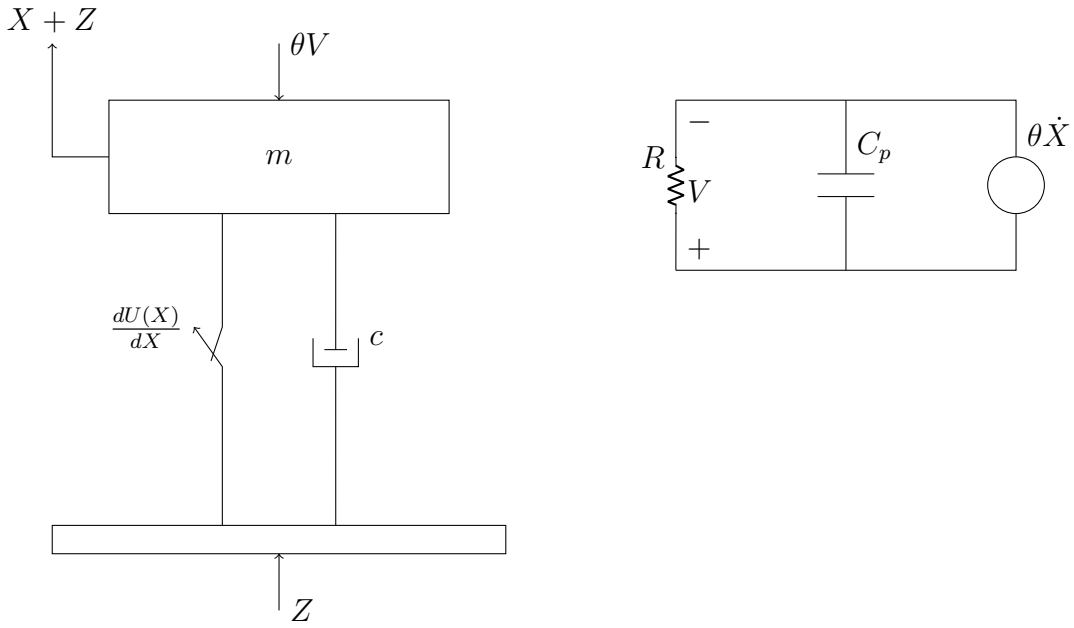

Figure 3.1: Schematic of the lumped parameter representation of the nonlinear harvesting system [16]

It was previously shown that well-separated modes allow a lumped parameter model to sufficiently capture the dynamics of the linear piezoelectric energy harvester. While the nonlinear system is non-resonant, excitation still occurs at some frequency slightly shifted from resonance. Therefore, a similar modeling methodology is possible when deriving the equations of motion for the Duffing-oscillator-based piezoelectric vibration energy harvesting system. Figure 3.1 illustrates how a piezoelectric harvesting element is coupled to the mass-spring-damper system accounting for the electrical energy generated during beam deflection. Summation of forces and Kirchoff's voltage law leads to the following dimensional model of the nonlinear energy harvester:

$$\begin{aligned} m\ddot{X} + c\dot{X} + \frac{dU(X)}{dX} + \theta V &= -m\ddot{Z} \\ C_p\dot{V} + \frac{V}{R} - \theta\dot{X} &= 0 \end{aligned} \tag{3.1}$$

where X represents the relative displacement of a mass m, c represents the linear viscous damping,

θ represents the linear electromechanical coupling, $\ddot{Z}$ represents the base acceleration, C_p represents the capacitance of the piezoelectric element, and V represents the induced voltage measured across an equivalent resistive load R [15,16]. The function $U(X)$ represents the potential energy in the system; its shape depends on the nonlinearity present in the harvester. In general, the potential function can be written as:

$$U(X) = \frac{1}{2}k_1(1-r)X^2 + \frac{1}{4}k_2X^4 \tag{3.2}$$

also known as the Duffing potential leading to cubic nonlinearities in the mechanical oscillator. The coefficients k_1 and k_2 represent the linear and nonlinear stiffness, respectively, and r is a tuning parameter allowing variation in the linear stiffness around its nominal value. By varying the tuning parameter r and the nonlinearity strength $\delta = k_2/k_1$, three different topologies of the harvester can be designed. Setting $\delta = 0$ and $r < 1$ eliminates the nonlinearity and yields a monostable linear cantilevered harvester. When $r \leq 1$, a monostable Duffing oscillator results with a softening nonlinearity when $\delta < 0$ or a hardening nonlinearity when $\delta > 0$ (again, $\delta = 0$ reduces to the linear case). When the tuning parameter $r > 1$ and $\delta > 0$, the central equilibrium destabilizes, resulting in the bistable harvesting system of interest. The locations of the stable equilibria, $\overline{x}$, then depend on the tuning parameter and the strength of the nonlinearity; $\overline{x} = \pm\sqrt{(r-1)/\delta}$ [15]. Figure 3.2 highlights the shape of the potential function as tuning and nonlinearity strength are varied. Introducing terms:

$$x = \frac{X}{l_c} \qquad z = \frac{Z}{l_c} \qquad t = \tau\omega_n \qquad v = \frac{C_p}{\theta l_p}V$$

nondimensionalizes Equation 3.1 where l_c and l_p represent length scales and $\omega_n = \sqrt{k_1/m}$ represents the short circuit nominal frequency when $r = 0$. Applying the transformations above and substituting the derivative of the potential function, the nondimensional equations of motion can

be written as:

$$\begin{aligned} x'' + 2\zeta_n x' + (1-r)x + \delta x^3 + \kappa^2 v &= -z'' \\ v' + \lambda v + \gamma x' &= 0 \end{aligned} \tag{3.3}$$

where $()'$ represents the derivative with respect to nondimensional time τ [15, 16]. The following variables are defined:

$$\zeta_n = \frac{c}{2m\omega_n} \qquad \delta = \frac{k_2 l_c^2}{k_1} \qquad \kappa^2 = \frac{\theta^2}{k_1 C_p} \qquad \lambda = \frac{1}{RC_p\omega_n} \qquad \gamma = \frac{l_c}{l_p} \tag{3.4}$$

where ζ_n represents the mechanical damping ratio, κ represents the linear dimensionless electromechanical coupling coefficient between mechanical and electrical subsystems, λ represents the ratio between time constants of the mechanical and electrical subsystem, and γ represents a length scaling coefficient between the mechanical and electrical subsystems equal to unity under ideal coupling. While the dimensional forms of both κ^2 and γ are equal, the nondimensionalization groups terms differently allowing the coefficients to be split representing the indirect (direct) piezoelectric effect in the mechanical (electrical) equations. Such a representation allows for broader applicability in modeling the system.

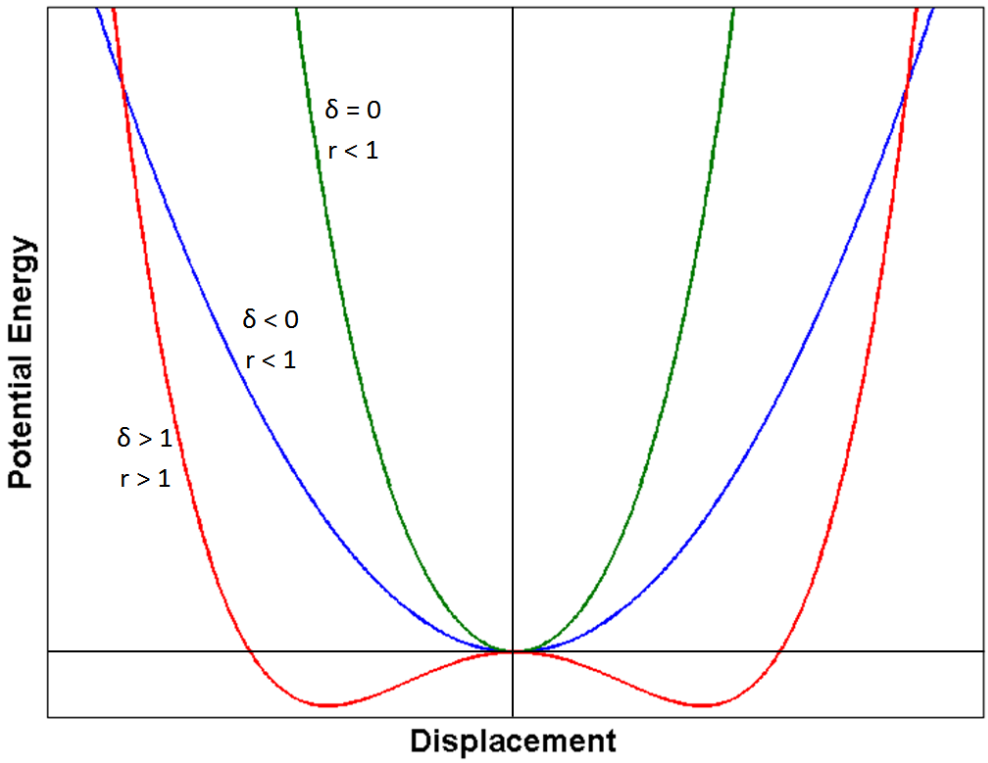

Figure 3.2: Shaping the potential functions of the nonlinear oscillator through manipulation of the nonlinearity

Setting $r > 1$ and $\delta > 0$ to create a bistable dynamic system admits three separate response types. Depending on the initial conditions and the magnitude and frequency of the excitation, the system can oscillate solely in one potential well (intrawell), move periodically between both potential wells (interwell), or move aperiodically between both potential wells (chaos). Aside from frequency matching to ensure resonance excitation, significant bandwidth improvements seen in bistable harvesters are only ensured when the system experiences interwell solutions. Unfortunately, this branch of solutions depends strongly on the initial conditions, harvester system parameters, and excitation strength [16]. If the input excitations are too small, interwell oscillation is never realized, and the system performs marginally better than a linear cantilever. Should proper potential well depth and excitation level be present, limitations can still arise as the favorable, large-amplitude response coexists with chaotic and aperiodic solutions.

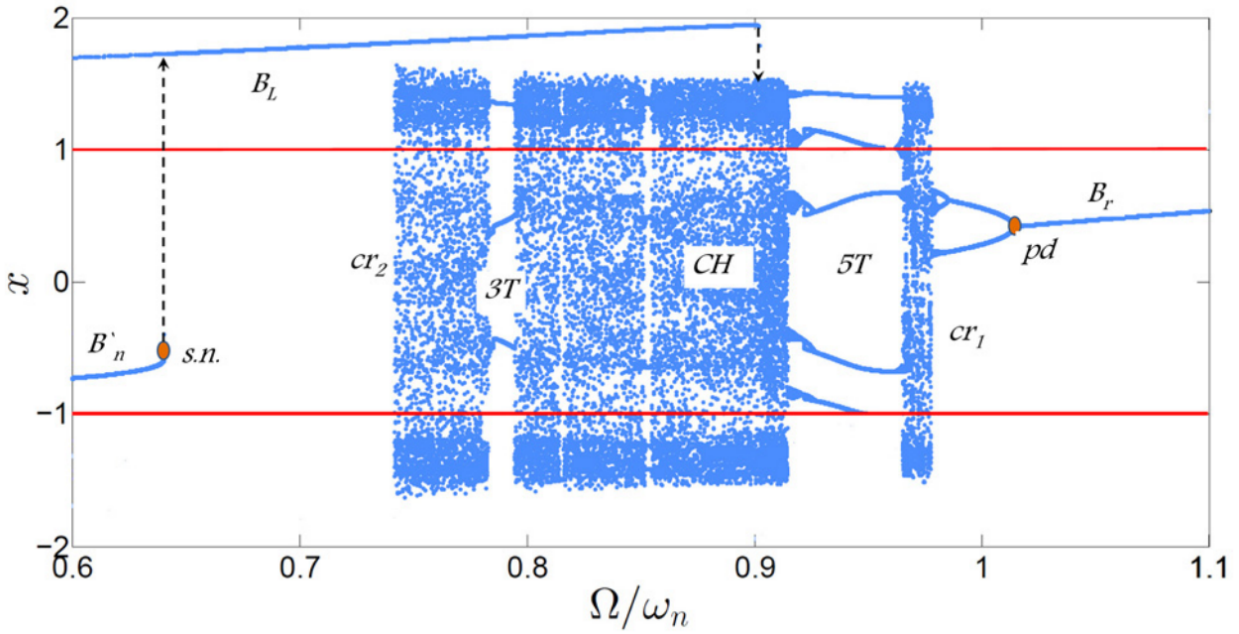

Figure 3.3: Bifurcation diagram capturing the coexistence chaotic and interwell solutions across a range of forcing frequencies [16]

Figure 3.3 presents a bifurcation diagram for the bistable harvesting system. While explained in more detail in Section 3.2, a bifurcation plot illustrates one dimension of a Poincaré map against a swept parameter of the system revealing under what range of the chosen parameter multiple attractors can exist. Figure 3.3 identifies that from frequency range $\frac{\Omega}{\omega}$ between 0.75 and 0.9 both chaotic attractors and large amplitude periodic orbit are present dependent only on initial conditions. While analytical techniques show promise to increase the bandwidth where the periodic interwell solution is unique, improving the system response when in the chaotic regime still merits attention [17, 18, 66].

3.2 Topological Analysis of the Chaotic System

The model described in Equation 3.3 is the foundation on which the chaotic control technique will be developed. In control systems, differential equations of motion are commonly rewritten into

first-order form aligning with standard practice in control design and use with MATLAB solvers:

$$
\begin{aligned}
{x_1}' &= x_2 \\
{x_2}' &= \frac{1}{2}x_1(1 - x_1^2) - 2\zeta x_2 + \kappa^2 x_3 + f\cos\Omega t \\
{x_3}' &= -\gamma x_2 - \lambda x_3
\end{aligned}
\tag{3.5}
$$

System parameters and initial conditions for Equation 3.5 must be chosen so that the solution exists in the chaotic attractor. Using bifurcation plots where displacement is plotted against every parameter in the system can isolate regions where chaotic trajectories occur. To stay consistent with the Duffing-based nonlinear harvester efforts in the literature parameters $\zeta = 0.01$, $\nu = 0.05$, $f = 0.08$, $\Omega = 0.8$, $\lambda = 0.05$, $\gamma = 0.5$, and $\kappa^2 = 0.05$ are selected, corresponding to previously studied chaotic parameters of the harvesting system [58].

Equation 3.5 was solved using MATLAB ode45 to generate a time series for each system state. Figure 3.4 illustrates the four dimensions of the harvesting system: displacement, velocity, voltage, and time as the independent variable. From Equation 3.5 it can be seen that voltage is linearly coupled to the nonlinear Duffing oscillator system. As such, the voltage state remains important but has little use in assisting the visualization of the chaotic system. Removing time as an independent variable and treating voltage as a third dimension of the system projected into the page, a two dimensional plot can be generated showing beam tip velocity against beam tip displacement. The phase portrait in Figure 3.5 begins the topological visualization techniques discussed in Chapter 2; namely Poincaré maps and return maps. These work in harmony to condition the time series data that will be used to isolate unstable periodic orbit points and compute control gains.

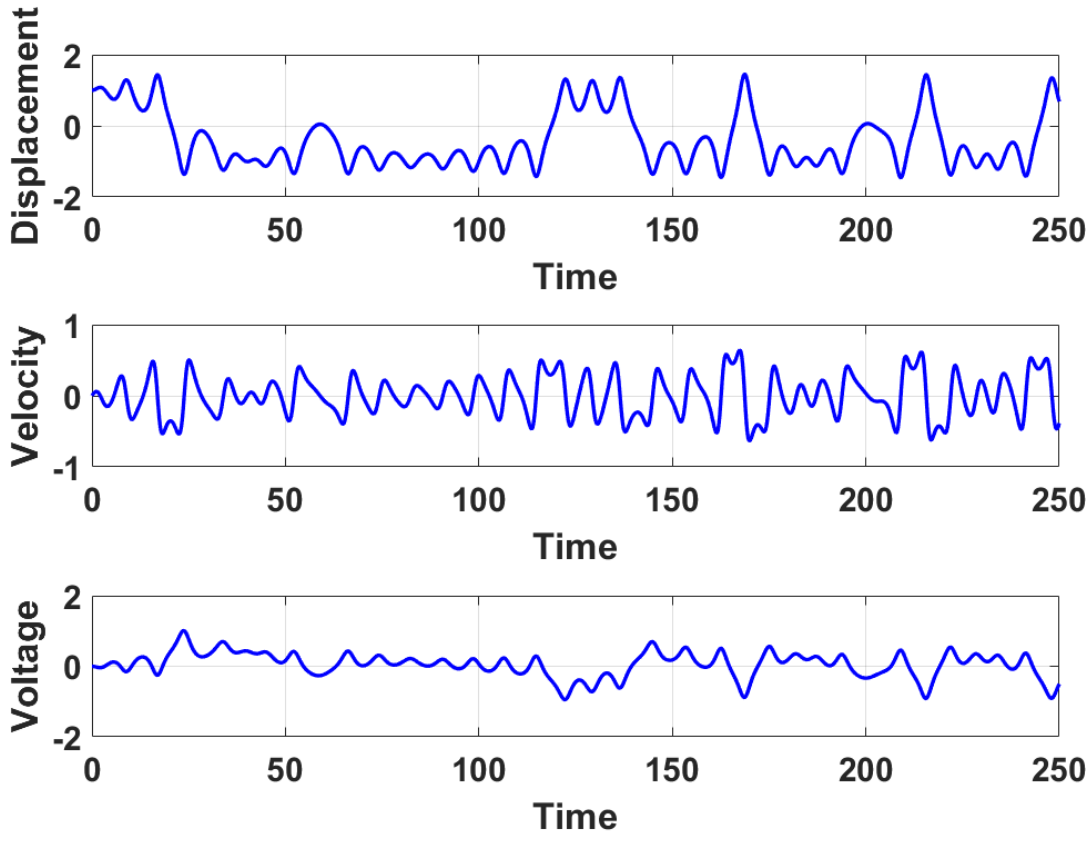

Figure 3.4: Chaotic time series solutions of the nonlinear harvesting system

A bistable equilibrium can be observed by inspecting the trajectories in Figure 3.5. The origin acts as a saddle point, with $x_{\pm} = \pm 1$ forming the stable wells. The existence of these equilibrium conditions indicates the existence of unstable periodic orbits within the system. Both the time series plot and phase portrait show that while dynamic behavior for a Duffing oscillator may appear random, the response is bounded. While more easily interpreted than the time series solutions, the phase portrait still lacks the clarity necessary for analysis. Using the method of visualization developed by Henri Poincaré detailed in Section 2.5.1, a data point within the phase portrait is taken for each state once per period of excitation. The resulting points are then plotted on the same axes as the phase portrait. The result is a more simplified representation of the system preserving periodic behavior. A Poincaré map for the Duffing oscillator harvesting system is shown atop a

complete phase portrait in Figure 3.6.

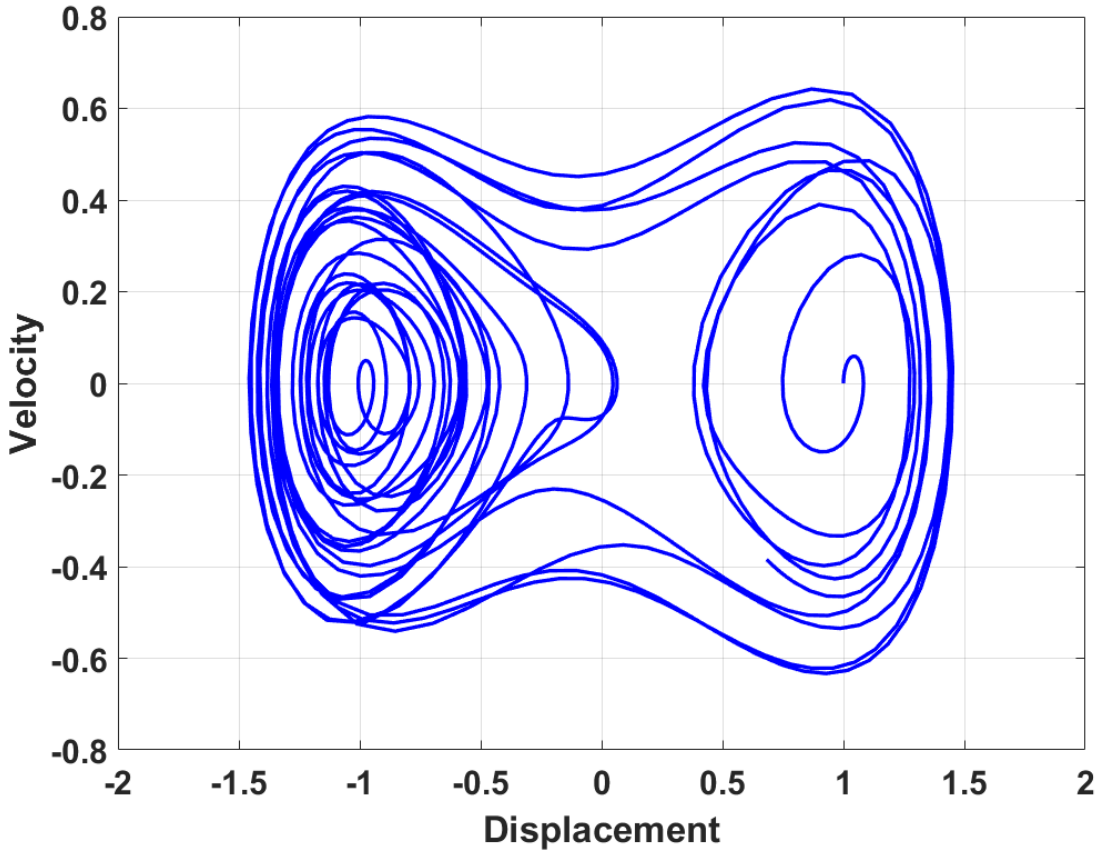

Figure 3.5: A chaotic phase portrait of the nonlinear harvesting system

The presence of many points spread throughout the Poincaré section confirms chaotic behavior of the Duffing oscillator, and the shape of the plot is known as a chaotic attractor. This attractor is the bounded structure on which all of the chaotic trajectories reside. Note, however, that the structure can look different if a Poincaré section is started at a different initial point along the excitation period. Figure 3.7 depicts a different Poincaré section for the same oscillator, but with the initial data point taken at some τ later within the first period. For the control design in this work, all Poincaré sections are sampled at the positive-slope zero crossing of the harmonic excitation. This existence of infinitely many Poincaré sections containing infinitely many unstable periodic orbits points increases the likelihood of isolating desirable large amplitude orbits. Ideal selection of a starting point is not a subject of this work, but a parallel advancement that can be made to the benefit of the field.

With a method visualization for the unstable periodic orbit points of the system defined, a bifurcation plot of the harvesting system can be constructed to highlight the alternate solutions that can arise independent of chaos or the large amplitude response. A typical bifurcation plot sweeps a single parameter of the system across a range of values and computes a Poincaré section for each value of the parameter. A single state from the section is then plotted versus the parameter, creating a side profile of stacked Poincaré sections. The result is used to dictate where chaotic motion exists in addition to any other solution attractor visible in the system. Holding all parameters constant and varying the forcing amplitude from zero to five results in a bifurcation plot shown in Figure 3.8. The vertical-axis corresponds to the beam tip displacement values with the horizontal-axis describing the parameter variation. The results of the bifurcation diagram in Figure 3.8 can be roughly interpreted to illustrate values of forcing amplitude where one point attractors ($f = 0.2$ to $0.4, 2.2$ to 3.2), period doubling regions ($f = 2.2$ to 3.6), and regions of chaotic motion ($f = 0$ to $0.2, 0.4$ to $2.2, 3.6$ to 5) can exist.

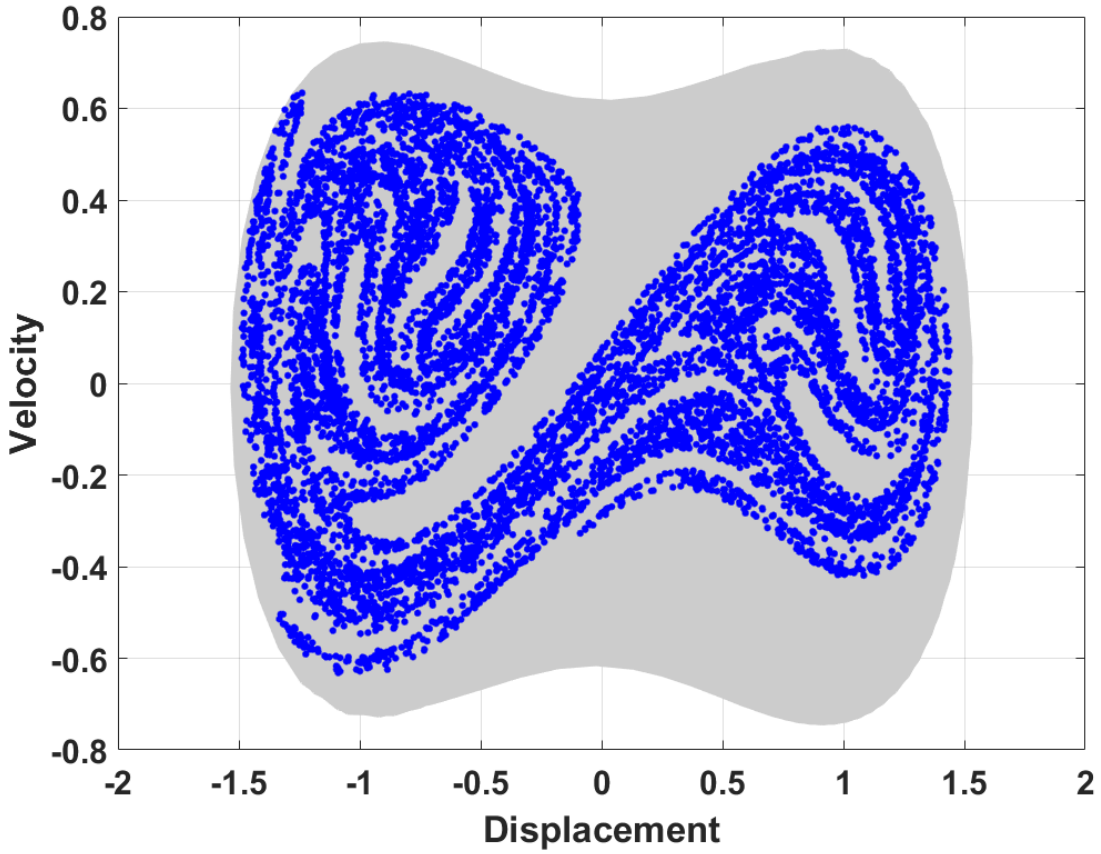

Figure 3.6: A Poincaré Section of an harvesting system sampled every nT

The phenomenon behind bifurcations and how these different attractors are created and destroyed is an active field of research beyond the scope of the energy harvesting problem. Instead, the different solution regions are analyzed solely from the perspective of displacement. Larger displacements cause larger strains in the piezoelectric element, and therefore result in larger power outputs of the system. While in general targeting low forcing amplitudes is desirable for harvesting ambient vibrations, the following analysis is purely for comparative purposes.

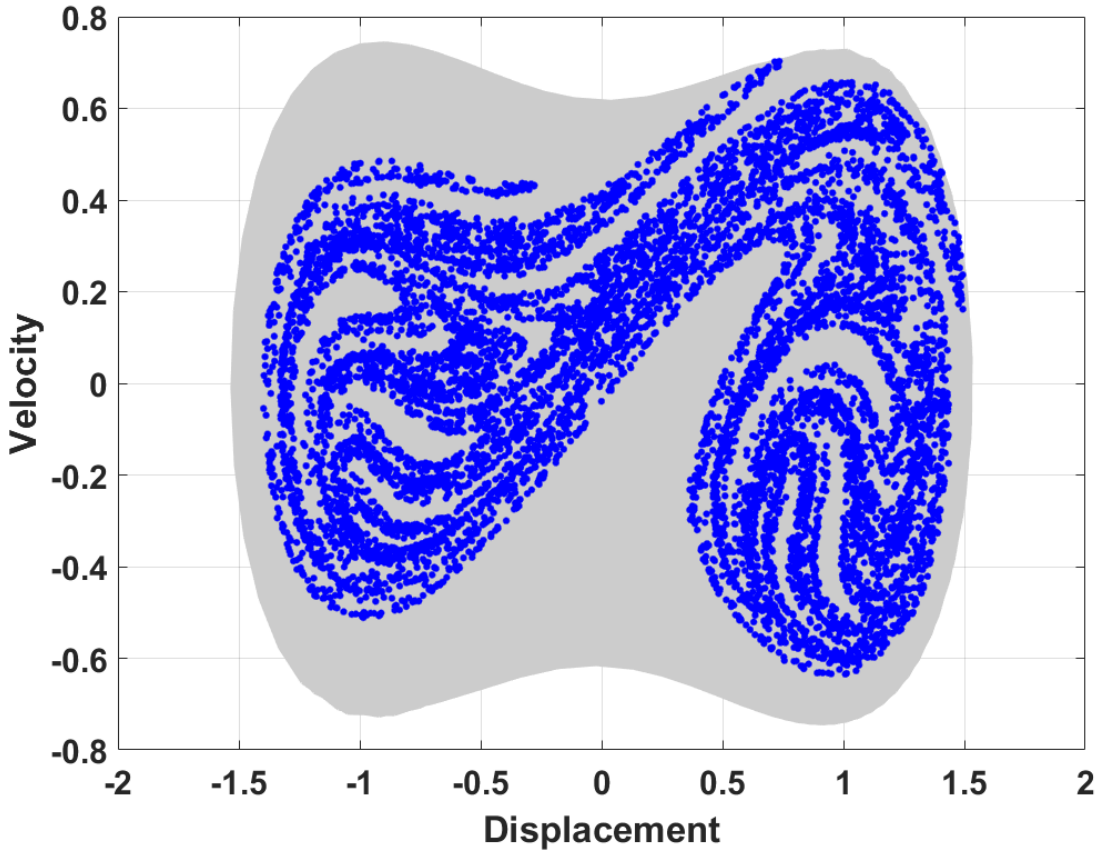

Figure 3.7: A Poincaré Section of an harvesting system sampled every $\tau + nT$

Studying the one point attractor region, a phase portrait and Poincaré section was determined at a forcing amplitude of $f = 0.02$. The existence of one branch in Figure 3.8 at this amplitude illustrates that the Poincaré section consists of a single point. A point in a two dimensional section correlates to a stable limit cycle in the higher dimensional system. Due to excitation outside of the chaotic regime, Figure 3.9 illustrates oscillation around one of the potential wells. Inspecting the Poincaré section, all trajectories evolve to the location of a single stable periodic orbit within the potential well. This is not useful for improving the bandwidth of a piezoelectric energy harvester, and other regions of the bifurcation plot must be analyzed.

Since the end goal is to improve the bandwidth of the harvester, operating on a period-1 orbit within

a single potential well is not beneficial. Stepping over in Figure 3.8, a period doubling region is studied where $f = 3.55$. Figure 3.10 shows a more dynamic phase portrait than the single point attractor; however, the system still biases one potential well. Worse still, the Poincaré section for this period doubling condition shows the beam snapping back and forth repeatedly with a large net displacement of 1.5 but not occupying two specific points as expected for a stable period-2 orbit. Without the clear existence of an orbit, driving the system within the period doubling region can increase the displacement of the system, but will likely interfere with periodicity required for the harvesting circuitry.

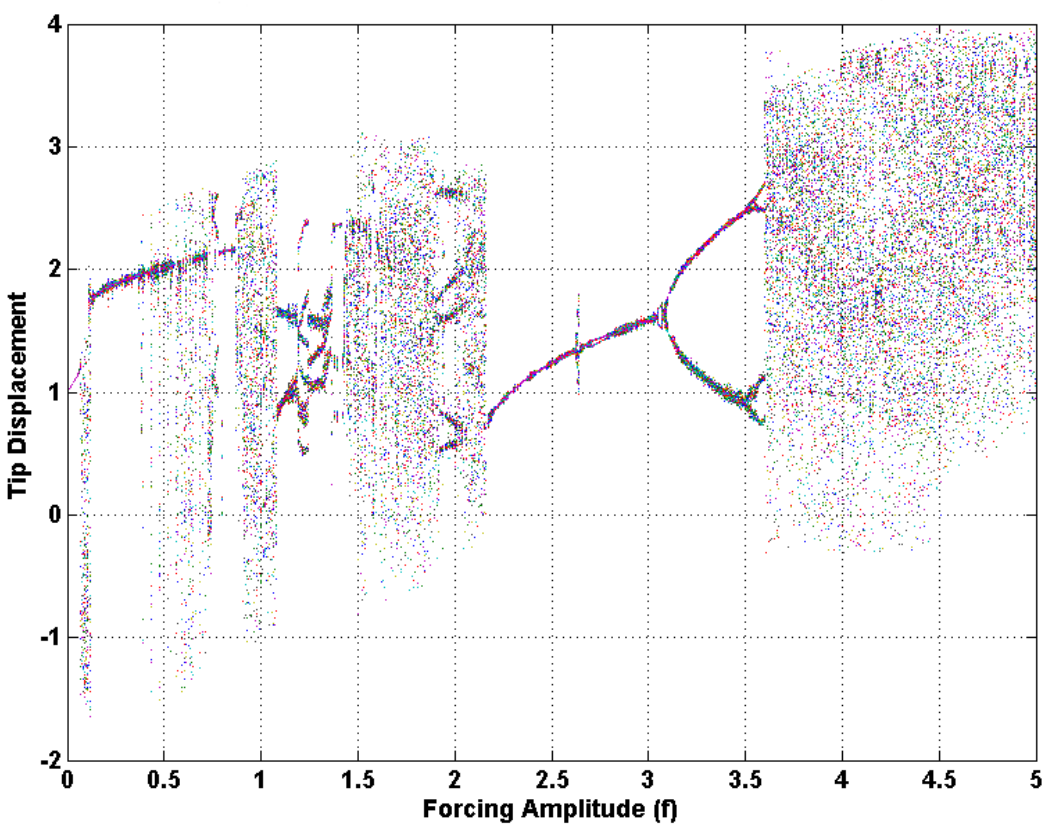

Figure 3.8: Bifurcation plot observing displacement under a sweep of forcing amplitude

Studying the dynamics of other solutions of the Duffing oscillator builds a foundation in the use of the topological analysis tools and highlights the weaknesses that can be mitigated by embracing chaotic motion. By isolating the periodic orbits in the chaotic Duffing oscillator shown in Figure 3.6, large displacement trajectories can be isolated for use in subsequent control towards the goal of improved piezoelectric-based vibration energy harvesting.

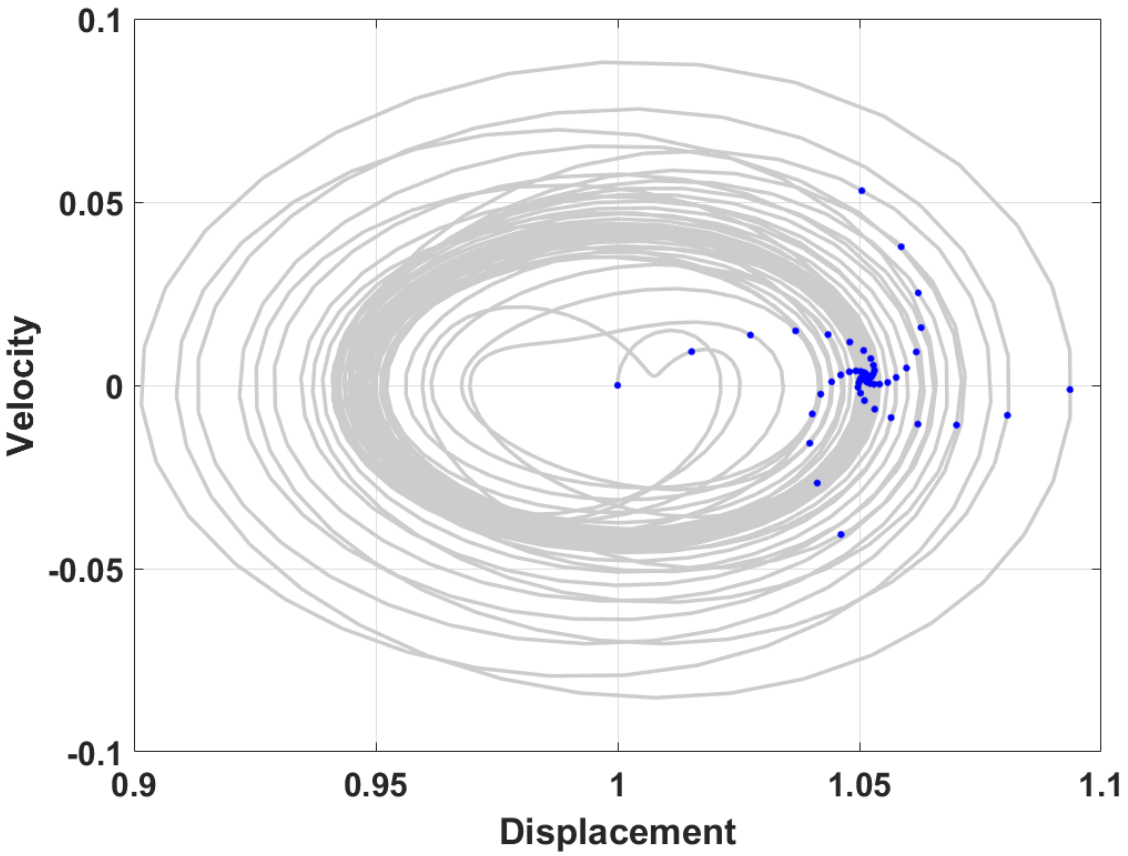

Figure 3.9: Topological representation of a Duffing oscillator acting in a one-point attractor

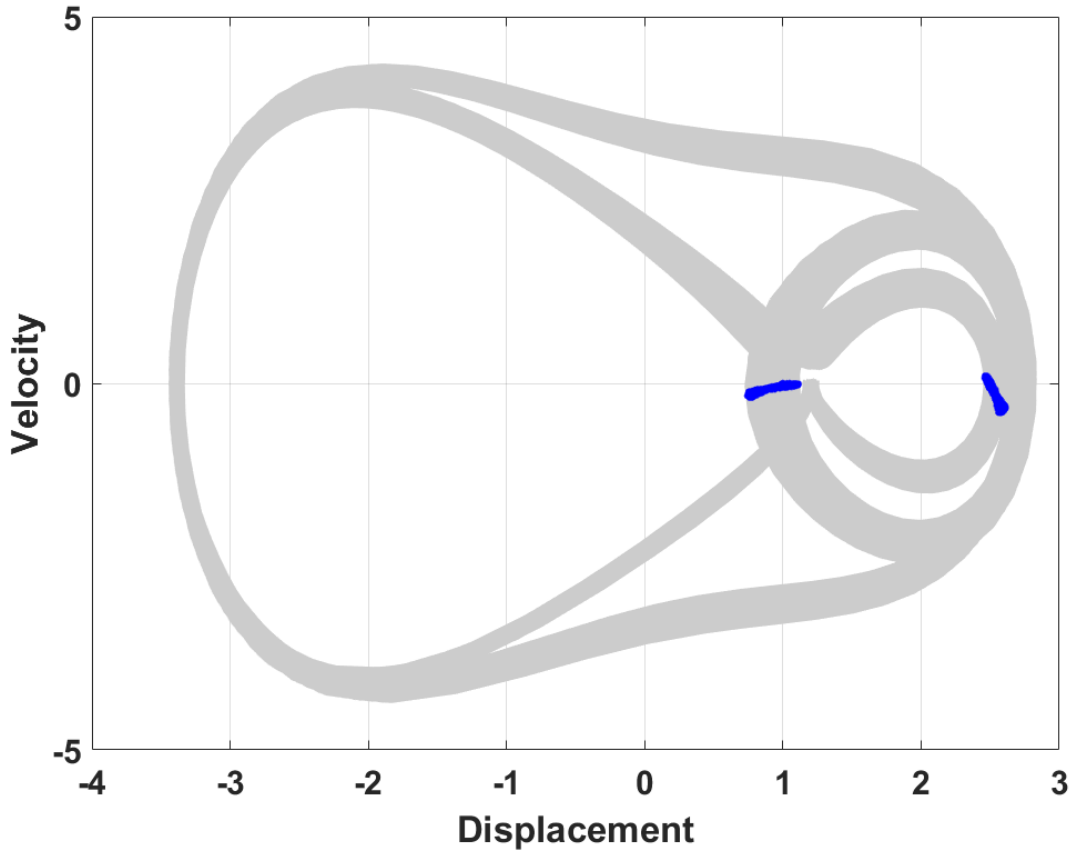

Figure 3.10: Topological representation of a Duffing oscillator during a period doubling route to chaos

3.2.1 Orbit Isolation

While bifurcation plots and Poincaré sections can illustrate the existence of chaotic motion, very little can be said about both the exact location of the orbit points and their respective periodicity. Introduced in Chapter 2, return maps plot a time series from a Poincaré section against itself n periods shifted in time. Since each point in a Poincaré section represents a first return from the previous point, plotting successive Poincaré points against each other is called a first return map. There is no theoretical limitation to what period return map can be created and using larger return times results in higher-period orbits. Return maps of higher periods will contain fewer orbits for the same length time series. Distinguishing between a period-8 orbit, multiple period-2 and period-

4 orbits, or false detection becomes a challenge due to the extreme sensitivity to initial conditions inherent to chaotic systems [67, 68]. Two return maps are created with period-1 and period-4 returns respectively in Figures 3.11 and 3.12. Both horizontal and vertical axes correspond to displacement data; therefore the points occurring along the diagonal line specify unstable orbits where the original and future return are a candidate orbit for control. For a period one return, the return map shows a large cluster of unstable periodic orbits in the attractor. As return time increases, the figures illustrate how return maps lose structure with less unstable periodic orbits accessible in the attractor.

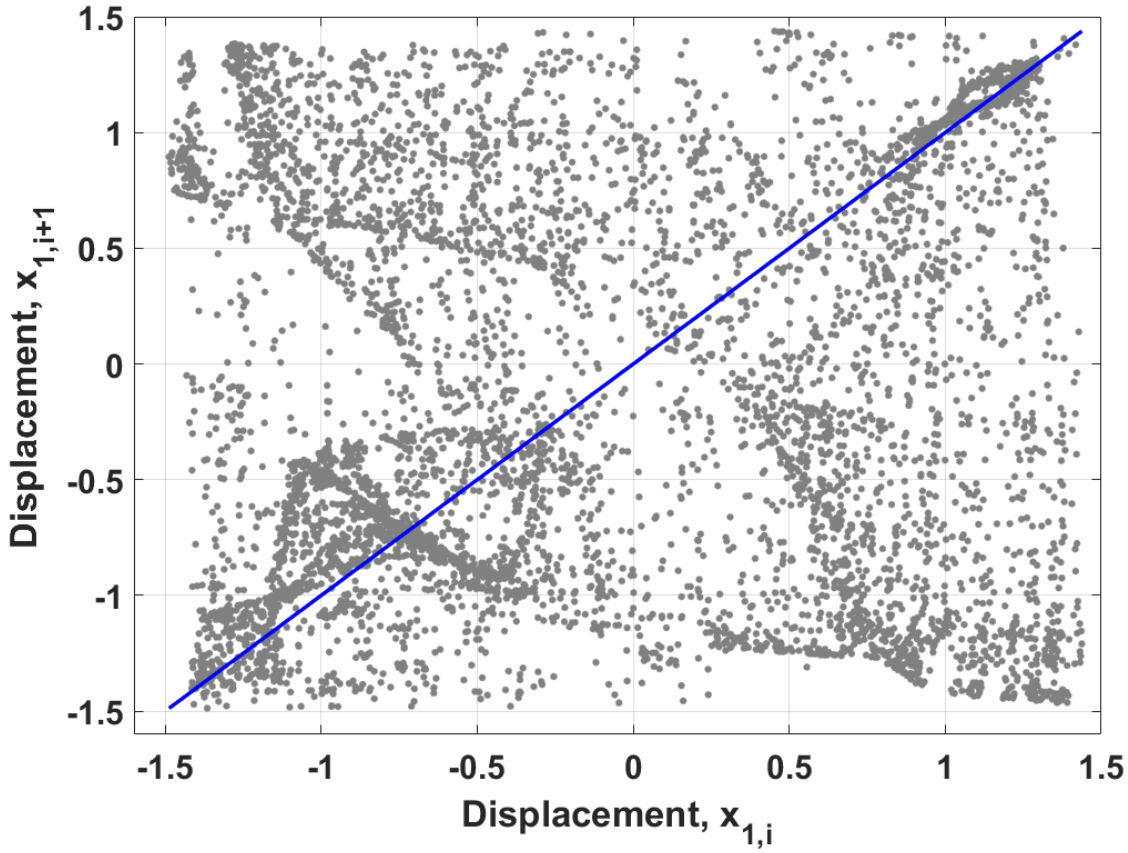

Figure 3.11: First return map of the Duffing oscillator-based energy harvesting system

Compared to the nonlinear analysis of the one point attractor and period doubling Duffing regimes, the benefits of chaos are easily justified. By choosing different harmonic forcing amplitudes, mo-

tion along a chaotic attractor can be quantified, with any one of the infinite unstable periodic orbits becoming a candidate for control. For the Duffing oscillator harvester studied, the ideal chaotic regime is actually accessible through a lower forcing amplitude than many of the other regimes. Not only will a dense set of periodic orbits exist, but the harvester itself can function in lower energy ambient environments and still result in larger deflections made possible through the chaotic controllers.

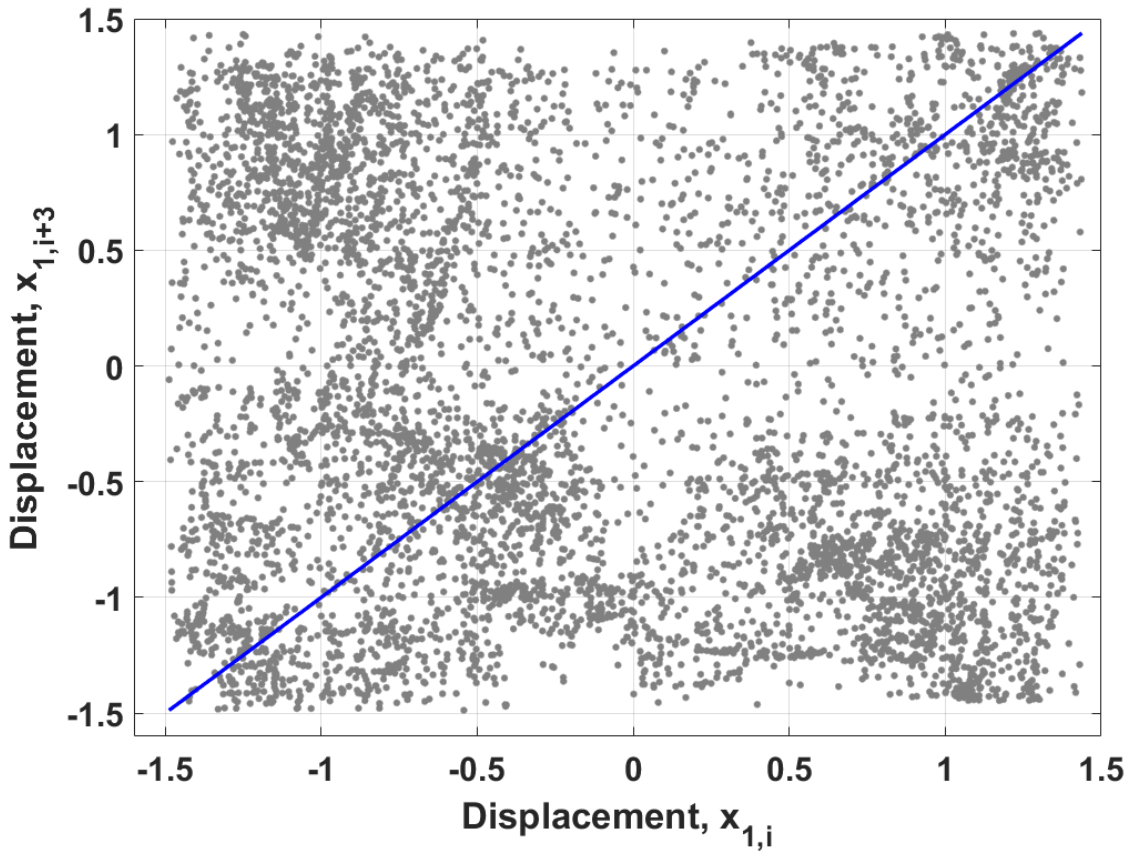

Figure 3.12: First return map of the Duffing oscillator-based energy harvesting system

Visual inspection of a return map is inefficient and fails to shed any light on the intermediate points for orbits of periods larger than one. For instance, a period-5 orbit is made of up five unstable periodic orbit points, yet a period-5 return map only illustrates the first and last orbit of the return. A single point representing a large periodic orbit be good enough in some cases, but a more robust solution captures the intermediate points and uses them during control design for a simultaneous stabilization strategy [69]. To determine the unstable orbit points of the system from the Poincaré section data, a recurrence algorithm was adopted from Lathrop et al. [70].

3.2.1.1 Recurrence Detection

Lathrop et al. devised a method of recurrence detection centered around the observation that as a point x nears an orbit, the trajectory stays in the vicinity of the orbit for some amount of time, moving with roughly the same frequency as the orbit, before eventually deviating due the chaotic nature of the system [70]. This motion is therefore an approximation of the orbit. To isolate the potential orbit points, a large amount of data is gathered at successive Poincaré intersections with x_i as a point on the attractor. Following the observed images, x_{i+1}, x_{i+2}, ..., x_{i+k}, with index k representing the lowest integer $k > i$ where $\|x_k - x_i\| < \epsilon$. The orbit is then defined with period $m = k - i$ where x_i is a (m, ϵ) recurrent point and ϵ represents a small region around the fixed point [70].

The isolated series of orbit points only marks a candidate for a potential orbit. The sensitivity of chaotic systems reduces the likelihood that every isolated sequence is an actual orbit point. Instead, collecting all likely (m, ϵ) recurrent points, grouping them, and computing the average to determine $\bar{x}_1, \bar{x}_2, \ldots, \bar{x}_m$, reasonably estimates the locations of the actual orbit $x_1^*, x_2^*, \ldots, x_m^*$. This grouping, coupled with a smaller region ϵ and larger data sets all work to ensure the likelihood that the estimated orbit points converge to an actual existing unstable periodic orbit of the system.

A MATLAB script used to determine recurrence points for each period is in Appendix B.

The recurrence method can be easily implemented in a chaotic system, with a few potential setbacks. Accuracy improvements made by reducing the size of the ϵ-ball require a much longer time series to make the estimates. The dependence of vector length, ϵ-ball, and orbit accuracy result in a system that may take a significant amount of time to converge on even low period orbits. More specifically, should the algorithm isolate a sub-optimal orbit, repeating the method further increases the amount of time needed before a stabilized orbit can take effect. Improved methods of orbit detection have been shown to shed dependence on an ϵ-ball, converge with data sets as small as 100 samples, versus thousands sometimes needed for recurrence detection, and isolate all possible orbits a specific period as opposed to just the least unstable orbit [71]. For this work the simple recurrence method is used throughout. To demonstrate the method, Figure 3.13 illustrates the isolated unstable periodic orbit points for periods six through ten.

3.2.2 System Model Approximation

Control is centered on the idea of stabilizing a three-dimensional continuous trajectory through periodic perturbation of an unstable orbit point isolated through reduced dimensional mapping onto its stable manifold. Once the unstable periodic orbits have been determined for arbitrary period m, the pole placement control strategies require a linear regression algorithm to fit an approximated state-space model at each orbit point. From this analysis, each point $\bar{x}_1, \bar{x}_2, \ldots, \bar{x}_m$ will have corresponding matrix pairs $(A_1, B_1), (A_2, B_2), \ldots, (A_m, B_m)$ computed from the same data used for recurrence detection. In the next two sections a linear regression algorithm is described with an iterative method to improve the estimated models. In addition, the algorithm has been generalized for arbitrary system dimension n and period p.

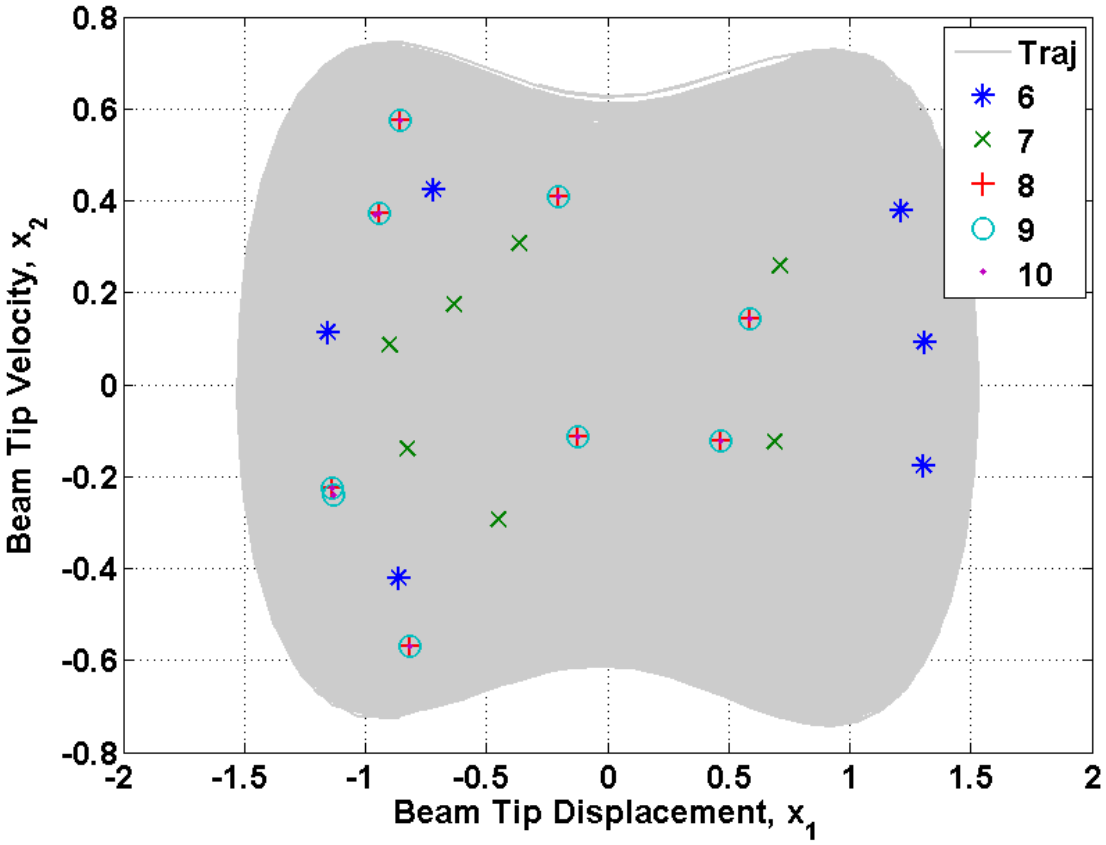

Figure 3.13: Recurrence results on the harvester time series data for orbits of period six through ten

3.2.2.1 Linear Regression

General linear regression uses data pairs $(x_1, y_1), (x_2, y_2), \ldots, (x_p, y_p)$, least squares to fit the coefficients a and c in a function $y = ax + c$. For this case, the best fit line is defined as the line that minimizes the sum of the squared residuals of the linear regression model. Framing the residuals as an error $e_j = y_j - (ax_j + c)$, the algorithm can be written as:

$$\min_{a,c} : \sum_{j=1}^{p} e_j^2 = \sum_{j=1}^{p} [y_j - (ax_j + c)]^2 \tag{3.6}$$

For a general n-dimensional problem, Equation 3.6 expands to:

$$\min_{a_1 \ldots a_k, c} : \sum_{j=1}^{p} e_j^2 = \sum_{j=1}^{p} \left[y_j - (a_1 x_{1,j} + a_2 x_{2,j} + \ldots + a_k x_{k,j} + c) \right]^2 \tag{3.7}$$

The data used in the model fit represent a deviation of a measured data point from the nearby isolated orbit point. Therefore, the points x_k represent the deviation $\delta x_i = x_i - \overline{x}_i$ and y_j represents the image of x_i one Poincaré piercing later $\delta x_{i+1} = x_{i+1} - \overline{x}_{i+1}$. Now, a linear curve is being estimated for $\delta x_{i+1} = f(\delta x_i)$ using data points within $\xi > \epsilon$. Therefore, for every estimated unstable orbit point $\overline{x}_1$, $\overline{x}_2$, ..., $\overline{x}_m$, data pairs (x_i, x_{i+1}) in which both $\|x_i - \overline{x}_i\| < \xi$ and image one Poincaré piercing later $\|x_{i+1} - \overline{x}_{i+1}\| < \xi$ should be found. It is important to ensure proper choice of ξ, as a value too small would result in long run times to gather enough data, but a value too large could yield points in which a linearized model is no longer valid.

For a two-dimensional system, the linear fit for $\partial x_{i+1} = f(\partial x_i)$ takes the form:

$$\begin{aligned}
\delta x_{i+1,1} &= a_{1,1}\delta x_{i,1} + a_{1,2}\delta x_{i,2} + \ldots + a_{1,n}\delta x_{i,n} + c_1 \\
\delta x_{i+1,2} &= a_{2,1}\delta x_{i,1} + a_{2,2}\delta x_{i,2} + \ldots + a_{2,n}\delta x_{i,n} + c_2 \\
&\vdots \\
\delta x_{i+1,n} &= a_{n,1}\delta x_{i,1} + a_{n,2}\delta x_{i,2} + \ldots + a_{n,n}\delta x_{i,n} + c_n
\end{aligned} \tag{3.8}$$

The values c_i form a vector that denotes an offset quantifying how far measured trajectories are from the isolated unstable orbit. Should c_i be equal to zero, then $\overline{x} = x^*$ and the trajectory lies on the orbit perfectly. However, since the vector c_i is often nonzero, an iterative improvement method can be used to correct the estimates, essentially forcing all c_i to zero [72].

3.2.2.2 Improved Linear Regression

Proper approximation assumes that the $\overline{x} = x^*$, implying that all c_i are zero, which is not the case in real-world systems. Including a correction factor through the addition of error terms and subsequent minimization of the error terms through repeated iteration allows the fixed points to be adjusted to their "true" values. For two dimensional Poincaré data the adjusted terms can be defined as $[\overline{x} + dx, \overline{y} + dy] = [x^*, y^*]$ where dx and dy represent the zero offsets. For a period-one orbit the least squares method can be rewritten as:

$$\begin{aligned} [\delta x_{i+1} - dx] &= a_{11}[\delta x_i - dx] + a_{12}[\delta y_i - dx] \\ [\delta y_{i+1} - dy] &= a_{21}[\delta x_i - dy] + a_{22}[\delta y_i - dy] \end{aligned} \tag{3.9}$$

Extending to a period-two orbit, the least squares method with adjustment terms is:

$$\begin{aligned} \delta x_{i+1,1} - a_{11,1}\delta x_{i,1} - a_{12,1}\delta y_{i,1} &= -a_{11,1}dx_1 - a_{12,1}dy_1 + dx_2 \\ \delta y_{i+1,1} - a_{21,1}\delta x_{i,1} - a_{22,1}\delta y_{i,1} &= -a_{21,1}dx_1 - a_{22,1}dy_1 + dy_2 \\ \delta x_{i+1,2} - a_{11,2}\delta x_{i,2} - a_{12,2}\delta y_{i,2} &= -a_{11,2}dx_2 - a_{12,2}dy_2 + dx_1 \\ \delta y_{i+1,2} - a_{21,2}\delta x_{i,2} - a_{22,2}\delta y_{i,2} &= -a_{21,2}dx_2 - a_{22,2}dy_2 + dy_1 \end{aligned} \tag{3.10}$$

Rewriting both into matrix form sheds light on how the algorithms change when considering different periods.

Period 1:

$$\begin{bmatrix} \delta x_{i+1} - a_{11}\delta x_i - a_{12}\delta y_i \\ \delta y_{i+1} - a_{21}\delta x_i - a_{22}\delta y_i \end{bmatrix} = \begin{bmatrix} (1 - a_{11}) & -a_{12} \\ -a_{21} & (1 - a_{22}) \end{bmatrix} \begin{Bmatrix} dx \\ dy \end{Bmatrix} \tag{3.11}$$

Period 2:

$$\begin{bmatrix} \delta x_{i+1,1} - a_{11,1}\delta x_{i,1} - a_{12,1}\delta y_{i,1} \\ \delta y_{i+1,1} - a_{21,1}\delta x_{i,1} - a_{22,1}\delta y_{i,1} \\ \delta x_{i+1,2} - a_{11,2}\delta x_{i,2} - a_{12,2}\delta y_{i,2} \\ \delta y_{i+1,2} - a_{21,2}\delta x_{i,2} - a_{22,2}\delta y_{i,2} \end{bmatrix} = \begin{bmatrix} -a_{11,1} & -a_{12,1} & 1 & 0 \\ -a_{21,1} & -a_{22,1} & 0 & 1 \\ 1 & 0 & -a_{11,2} & -a_{12,2} \\ 0 & 1 & -a_{21,2} & -a_{22,2} \end{bmatrix} \begin{bmatrix} dx_1 \\ dy_1 \\ dx_2 \\ dy_2 \end{bmatrix} \tag{3.12}$$

Each iteration of the augmented regression algorithm results in new estimates given by:

$$\begin{bmatrix} \overline{x}_{\text{new}} \\ \overline{y}_{\text{new}} \end{bmatrix} = \begin{bmatrix} \overline{x}_{\text{old}} \\ \overline{y}_{\text{old}} \end{bmatrix} + \begin{Bmatrix} dx \\ dy \end{Bmatrix} \tag{3.13}$$

with dx and dy becoming incrementally smaller. Iterating until these components are below a certain threshold can essentially ensure $\overline{x} = x^*$ with respect to the measured unstable periodic orbit points [72]. For the harvesting system proposed, it is desirable to consider unstable periodic orbits of arbitrary period. It is also useful to reduce the dimensionality constraint imposed in the formula and derive a function capable of iterating a least squares algorithm regardless of dimension or period. The MATLAB script used to compute the system matrices is based on the following

iterative linear least squares regression of the form $\mathbf{L} = \mathbf{N} * \mathbf{P}$ where:

$$\mathbf{L} = \begin{bmatrix} \delta x_{1_{i+1,1}} - a_{11,1}\delta x_{1_{i,1}} - a_{12,1}\delta x_{2_{i,1}} - \ldots - a_{1n,1}\delta x_{n_{i,1}} \\ \delta x_{2_{i+1,1}} - a_{21,1}\delta x_{1_{i,1}} - a_{22,1}\delta x_{2_{i,1}} - \ldots - a_{2n,1}\delta x_{n_{i,1}} \\ \vdots \\ \delta x_{n_{i+1,1}} - a_{21,1}\delta x_{1_{i,1}} - a_{22,1}\delta x_{2_{i,1}} - \ldots - a_{nn,1}\delta x_{n_{i,1}} \\ \delta x_{1_{i+1,2}} - a_{11,2}\delta x_{1_{i,2}} - a_{12,2}\delta x_{2_{i,2}} - \ldots - a_{1n,2}\delta x_{n_{i,2}} \\ \delta x_{2_{i+1,2}} - a_{21,2}\delta x_{1_{i,2}} - a_{22,2}\delta x_{2_{i,2}} - \ldots - a_{2n,2}\delta x_{n_{i,2}} \\ \vdots \\ \delta x_{n_{i+1,2}} - a_{21,2}\delta x_{1_{i,2}} - a_{22,2}\delta x_{2_{i,2}} - \ldots - a_{nn,2}\delta x_{n_{i,2}} \\ \delta x_{1_{i+1,p}} - a_{11,p}\delta x_{1_{i,p}} - a_{12,p}\delta x_{2_{i,p}} - \ldots - a_{1n,p}\delta x_{n_{i,p}} \\ \delta x_{2_{i+1,p}} - a_{21,p}\delta x_{1_{i,p}} - a_{22,p}\delta x_{2_{i,p}} - \ldots - a_{2n,p}\delta x_{n_{i,p}} \\ \vdots \\ \delta x_{n_{i+1,p}} - a_{21,p}\delta x_{1_{i,p}} - a_{22,p}\delta x_{2_{i,p}} - \ldots - a_{nn,p}\delta x_{n_{i,p}} \end{bmatrix} \tag{3.14}$$

$$\mathbf{N} = \begin{bmatrix} \begin{bmatrix} & & \\ & \mathbf{A}_1 & \\ & & \end{bmatrix} & \begin{matrix} 1 & 0 & \cdots & 0 \\ 0 & 1 & \cdots & 0 \\ \vdots & \vdots & \ddots & \vdots \\ 0 & 0 & \cdots & 1 \end{matrix} & \cdots & \begin{matrix} 0 & 0 & \cdots & 0 \\ 0 & 0 & \cdots & 0 \\ \vdots & \vdots & \ddots & \vdots \\ 0 & 0 & \cdots & 0 \end{matrix} \\ \begin{matrix} 0 & 0 & \cdots & 0 \\ 0 & 0 & \cdots & 0 \\ \vdots & \vdots & \ddots & \vdots \\ 0 & 0 & \cdots & 0 \end{matrix} & \begin{bmatrix} & & \\ & \mathbf{A}_2 & \\ & & \end{bmatrix} & \cdots & \begin{matrix} 1 & 0 & \cdots & 0 \\ 0 & 1 & \cdots & 0 \\ \vdots & \vdots & \ddots & \vdots \\ 0 & 0 & \cdots & 1 \end{matrix} \\ \vdots & \vdots & \ddots & \vdots \\ \begin{matrix} 1 & 0 & \cdots & 0 \\ 0 & 1 & \cdots & 0 \\ \vdots & \vdots & \ddots & \vdots \\ 0 & 0 & \cdots & 1 \end{matrix} & \begin{matrix} 0 & 0 & \cdots & 0 \\ 0 & 0 & \cdots & 0 \\ \vdots & \vdots & \ddots & \vdots \\ 0 & 0 & \cdots & 0 \end{matrix} & \cdots & \begin{bmatrix} & & \\ & \mathbf{A}_p & \\ & & \end{bmatrix} \end{bmatrix} \qquad \mathbf{P} = \begin{Bmatrix} dx_{1_1} \\ dx_{2_1} \\ \vdots \\ dx_{n_1} \\ dx_{1_2} \\ dx_{2_2} \\ \vdots \\ dx_{n_2} \\ \vdots \\ dx_{n_p} \end{Bmatrix} \tag{3.15}$$

and:

$$\mathbf{A}_p = \begin{bmatrix} -a_{11,p} & -a_{12,p} & \cdots & -a_{1n,p} \\ -a_{21,p} & -a_{22,p} & \cdots & -a_{21,p} \\ \vdots & \vdots & \ddots & \vdots \\ -a_{n1,p} & -a_{n2,p} & \cdots & -a_{nn,p} \end{bmatrix} \tag{3.16}$$

Note that the result of the estimation thus far only represents the $(\mathbf{A})$ matrix in the $(\mathbf{A}, \mathbf{B})$. The matrix $\mathbf{B}$ is computed the same way, but the maximum allowable system perturbation must be applied at alternating periods of excitation. This new time series is then split into two arrays with and without the applied perturbation, and run through the least squares algorithm.

It is important to ensure that local linearity of the model is preserved. To determine if the choice

of ξ is successful, Figure 3.14 illustrates the points selected in the linear regression algorithm. Successful choice of ξ confirms that the isolated points lie on intersecting flat planes. There is no drawback to using too small a value for ξ other than array size and computation time. However, if too large a value for ξ is used then the planes shown in Figure 3.14 start to curve, violating the constraint of local linearity and preventing the control algorithm from performing as expected.

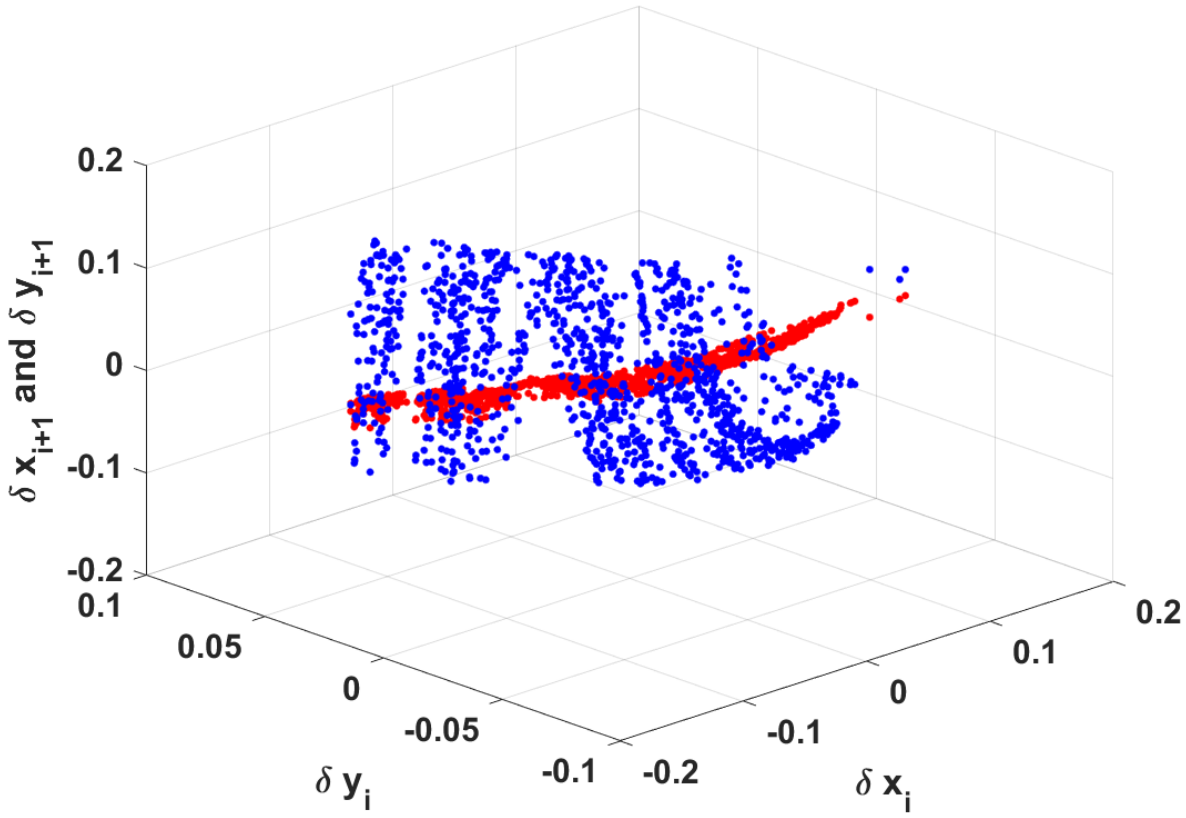

Figure 3.14: Poincaré points used in the linear least squares regression

3.3 Control Design

Successful isolation of the unstable periodic orbit points and a local state-space model constrained in a linear region of each orbit point complete the required steps before the chaotic control laws can be derived. This section presents three separate control techniques. The first two methods preserve model independence and stabilize a large displacement trajectory within the boundary of the chaotic attractor. The third method uses a model dependent continuous feedback control law that tracks both the current chaotic trajectories and the desired large amplitude response. Control then lifts the system from the lower-energy attractor to the higher-energy attractor consistent with the response shown in the literature for nonlinear bistable systems in vibration energy harvesting [15, 16, 58].

3.3.1 Ott, Grebogi, and Yorke Control

A time-invariant representation of the system can be defined as:

$$\begin{aligned}
\Delta \mathbf{x}_{k+1} &= \mathbf{A}_k \Delta \mathbf{x}_k + \mathbf{B}_k \Delta q_k \\
\mathbf{A}_k &= \left. \frac{\partial f\left(\mathbf{x}_k, q_k\right)}{\partial \mathbf{x}_k} \right|_{\overline{\mathbf{x}}_k, q_0} \\
\mathbf{B}_k &= \left. \frac{\partial f\left(\mathbf{x}_k, q_k\right)}{\partial q_k} \right|_{\overline{\mathbf{x}}_k, q_0} \\
\Delta \mathbf{x}_k &= \mathbf{x}_k - \overline{\mathbf{x}}_k \\
\Delta q_k &= q_k - q_0 = \mathbf{K}_k^T \Delta \mathbf{x}_k
\end{aligned} \tag{3.17}$$

where $\mathbf{A}_k$ and $\mathbf{B}_k$ represent the linear fit models in the vicinity of the periodic orbit points $\overline{\mathbf{x}}_k$, and both $\Delta \mathbf{x}_k$ and Δq_k are bounded to ensure any designed control law is only activated when the system trajectory enters the region in which the linear approximation is valid [73]. Periodicity of

the desired orbit requires $\mathbf{A}_{k+np} = \mathbf{A}_{k+p} = \mathbf{A}_k$ where n is any positive integer. This requirement also holds for matrices $\mathbf{B}$ and $\mathbf{K}$, meaning that a properly stabilized orbit will continuously cycle through the approximated linear regions for all future time.

During control of a period-p orbit with u unstable directions determined from the eigenvalues and eigenvectors of Equation 3.46, u small parametric perturbations $\{q_k, q_{k-1}, \ldots, q_{k+u-1}\}$ are applied when the trajectory is in a pre-specified control region dictated by a maximum allowable perturbation δq_{max}. These perturbations would act to control the modified state dynamics onto the stable subspace of the desired periodic orbit.

To solve for the control perturbations directly, consider u iterates of Equation 3.45 correlating to the number of unstable directions:

$$\begin{aligned}\mathbf{Y}_{k+u} - \overline{\mathbf{Y}}_{k+u} = \mathbf{\Phi}_{k,0}\left[\mathbf{Y}_k - \overline{\mathbf{Y}}_k\right] + \mathbf{\Phi}_{k,1}\mathbf{B}_k\left(q_k - \overline{q}\right) + \mathbf{\Phi}_{k,2}\mathbf{B}_{k+1}\left(q_{k+1} - \overline{q}\right) \\ + \ldots + \mathbf{B}_{k+(u-1)}\left(q_{k+(u-1)} - \overline{q}\right)\end{aligned} \tag{3.18}$$

where

$$\mathbf{\Phi}_{k,j} = \mathbf{A}_{k+u-1}\mathbf{A}_{k+u-2}\ldots\mathbf{A}_{k+j+1}\mathbf{A}_{k+j} \tag{3.19}$$

for $j = 1, 2, \ldots, (u-1)$ and $\mathbf{\Phi}_{k,u} \equiv \mathbf{I}$. Similar to classical control system theory, a controllability matrix can be formulated:

$$\mathbf{C}_k = [\mathbf{\Phi}_{k,1}\mathbf{B}_k \vdots \mathbf{\Phi}_{k,2}\mathbf{B}_{k+1} \vdots \cdots \vdots \mathbf{\Phi}_{k,u-1}\mathbf{B}_{k+u-2} \vdots \mathbf{B}_{k+u-1} \vdots \nu_{k+u,1} \vdots \nu_{k+u,2} \vdots \cdots \vdots \nu_{k+u,s+r}] \tag{3.20}$$

where $\nu_{i+u,1}$, $\nu_{i+u,2}$, and $\nu_{i+u,s+r}$ represent any set of linearly independent unit vectors spanning the linearized stable subspace. Note that u represents the number of unstable directions in Equation 3.46, $s = d - u$ represents the number of stable directions in Equation 3.46, d is the system dimension, and r is a product of Poincaré piercings. To guarantee stability of $\overline{\mathbf{Y}}$, the matrices $\mathbf{C}_k$

must be invertible. The control parameter can now be solved with:

$$q_k = \overline{q} - \mathbf{K}_k^T \left[\mathbf{Y}_k - \overline{\mathbf{Y}}_k \right] \tag{3.21}$$

where control gains $\mathbf{K}_k^T$ are found from:

$$\mathbf{K}_k^T = \chi \mathbf{C}_k^{-1} \mathbf{\Phi}_{i,0} \tag{3.22}$$

and χ represents a row vector whose first element is one and the remaining elements are zero [74]. The chosen control gains can then be implemented by computing perturbations for each period point, selecting the smallest perturbation, determining if the smallest perturbation is within the acceptable region where the linear approximation is valid, and if so, then applying the selected perturbation to the system.

3.3.2 Sliding Mode Control

While the high-dimensional OGY controller can work for the harvesting system, implementing a control law centered around invariant principles may act to reduce computational time as stable and unstable manifold directions do not need to be determined. In fact, certain high-dimensional nonlinear problems pose great difficulty in computing these directions for cases where the system Jacobians possess complex eigenvalues. Starting again from the state matrices developed through linear regression, the controlled harvesting system within the approximated linear regions can be represented as:

$$\Delta \mathbf{x}_{k+p} = \left(\prod_{i=1}^{p} \left(\mathbf{A}_i + \mathbf{B}_i \mathbf{K}_i^T \right) \right) \Delta \mathbf{x}_k \tag{3.23}$$

Paskota et al., theorized developing p unique controllers for simultaneous stabilization of large period orbits with a chaotic system, but determined that it is not enough to ensure $\left| \text{eig} \left(\mathbf{A}_k + \mathbf{B}_k \mathbf{K}_k^T \right) \right| <$

$\mathbf{1}$ for each $k = 1, 2, \ldots, p$ [69]. To guarantee stability of the desired periodic orbit, it is necessary and sufficient to ensure:

$$\left| \text{eig} \left(\prod_{i=1}^{p} \left(\mathbf{A}_i + \mathbf{B}_i \mathbf{K}_i^T \right) \right) \right| < 1 \tag{3.24}$$

Note that simply applying the typical OGY prescribed perturbation at every p^{th} piercing of the Poincaré section theoretically works, but requires long wandering times and is highly susceptible to disturbances and noise in application. The stability criterion in Equation 3.24 gives rise to the idea that it may be possible to prescribe a time-invariant matrix $\mathbf{F}$ such that [73]:

$$\mathbf{A}_k + \mathbf{B}_k \mathbf{K}_k^T = \mathbf{F}, \quad \forall\, k = 1, 2, \ldots, p \tag{3.25}$$

If so, since $\text{eig}(\mathbf{F}^p) = (\text{eig}(\mathbf{F}))^p$, proving that:

$$|\text{eig}(\mathbf{F})| < \mathbf{1} \tag{3.26}$$

would guarantee that Equation 3.24 is satisfied.

3.3.3 Defining the Invariant Manifold

With multiparameter control, an arbitrary closed-loop matrix $\mathbf{F}$ can be achieved through Equation 3.25, as long as the number of controllable parameters meets or exceeds the number of states. While several implementations for controlling the harvesting system are possible, consider a perturbation applied solely through the velocity state of the system. In this case, an arbitrary $\mathbf{F}$ cannot be achieved in the ordinary state space. By transforming the system into controllable canonical form, a time-invariant closed-loop representation for $\mathbf{F}$ can be realized [73]. The transformed system can be represented by:

$$\Delta \mathbf{x}_{\text{CF},k} = \mathbf{T}_k \Delta \mathbf{x}_k \tag{3.27}$$

where $\mathbf{T}_k$ are the transformation matrices used for formulating equivalent systems in controllable canonical form (subscript CF). The transformed linear region(s) of the chaotic system can be represented by:

$$\Delta \mathbf{x}_{\text{CF},k+1} = \mathbf{A}_{\text{CF},k} \Delta \mathbf{x}_{\text{CF},k} + \mathbf{B}_{\text{CF},k} \Delta q_k \tag{3.28}$$

where

$$\mathbf{A}_{\text{CF},k} = \begin{bmatrix} 0 & 1 & 0 & \dots & 0 \\ 0 & 0 & 1 & \dots & 0 \\ \vdots & \vdots & \vdots & \ddots & \dots \\ 0 & 0 & 0 & \dots & 1 \\ a_{\text{CF1},k} & a_{\text{CF2},k} & a_{\text{CF3},k} & \dots & a_{\text{CF}N,k} \end{bmatrix}$$

and

$$\mathbf{B}_{\text{CF},k} = [0, \dots, 0, 1]^T \tag{3.29}$$

are in controllable canonical form. In computing the transformation matrices $\mathbf{T}_k$, the following relations can be used for second-order periodic systems [73]:

$$\mathbf{C}_{k+p} = \mathbf{C}_k = [\mathbf{B}_{k+p-1}, \mathbf{A}_{k+p-1}\mathbf{B}_{k+p-2}] \tag{3.30}$$

$$\mathbf{t}_k^T \mathbf{C}_k = [0, 1] \tag{3.31}$$

$$\mathbf{T}_k = \begin{bmatrix} \mathbf{t}_k^T \\ \mathbf{t}_{k+1}^T \mathbf{A}_k \end{bmatrix} \tag{3.32}$$

Matrices $\mathbf{C}_k$ are again correlated to the controllability matrix in linear systems, but this time do not rely on the number of unstable and stable manifolds and do not require the inclusion of arbitrary

unit vectors spanning the stable subspace of the system. Applying the transformation:

$$\mathbf{A}_{\text{CF},k} = \mathbf{T}_{k+1}\mathbf{A}_k\mathbf{T}_k^{-1} \tag{3.33}$$

$$\mathbf{B}_{\text{CF},k} = \mathbf{T}_{k+1}\mathbf{B}_k \tag{3.34}$$

control gains $\mathbf{K}_{\text{CF},k}$ can be computed from the invariant formulation of the transformed system:

$$\mathbf{A}_{\text{CF},k} + \mathbf{B}_{\text{CF},k}\mathbf{K}_{\text{CF},k}^T = \mathbf{F} \tag{3.35}$$

where $\mathbf{F}$ is also in controllable canonical form:

$$\mathbf{F} = \begin{bmatrix} 0 & 1 & 0 & \dots & 0 \\ 0 & 0 & 1 & \dots & 0 \\ \vdots & \vdots & \vdots & \ddots & \vdots \\ 0 & 0 & 0 & \dots & 1 \\ f_1 & f_2 & f_3 & \dots & f_N \end{bmatrix} \tag{3.36}$$

Upon computing $\mathbf{K}_{\text{CF},k}$, the control gains can be transformed back into the physical phase space coordinates and implemented through the same method described in the OGY method:

$$\mathbf{K}_k = \mathbf{K}_{\text{CF},k}\mathbf{T}_k \tag{3.37}$$

In the absence of multiparameter control the invariant matrix, $\mathbf{F}$, cannot be made identically equal to zero. To compute a best alternative to reduce control effort and ensure stability of the chaotic

system, the controlled system can be written in physical coordinates:

$$\mathbf{A}_k + \mathbf{B}_k \mathbf{K}_k^T = \mathbf{T}_{k+1}^{-1} \mathbf{F} \mathbf{T}_k \tag{3.38}$$

with the following optimization applied:

$$\min_{\mathbf{F}} \min_{k} \left|\left| \mathbf{T}_{k+1}^{-1} \mathbf{F} \mathbf{T}_k \right|\right| \tag{3.39}$$

The controllable canonical form defining $\mathbf{F}$ allows the optimization to be performed over the eigenvalues λ_k:

$$z^N + \sum_{k=1}^{N} -f_k z^{k-1} = \prod_{k=1}^{N} (z - \lambda_k) \tag{3.40}$$

but must be solved on a case-by-case basis depending on the system in question [73].

3.4 Delay Reconstruction from Measured Times Series Data

The two control methods derived so far use time series data to fit local models that are then used in discrete perturbation-based control laws. An aside from the presented work in this dissertation, but an additional strength of the control method, is the ability to use delay reconstructed time series data. When using delay coordinates, the linearization in Equation 3.17 must to be modified to account for past parameter variations. Assuming that the time between two successive Poincaré piercings is analogous to the forcing period of the system, $T_f = \frac{2\pi}{\Omega}$, it is clear that when $\sigma\tau > T_f$, the delay coordinate $\mathbf{Z}_k$ will contain information about the previous Poincaré piercing(s) at time $t_k - T_f$. All parameter values $\{q_k, q_{k-1}, \ldots, q_{k-r}\}$ will have an influence on the delay coordinate Z_k, where r is the smallest integer such that $\sigma\tau < rT_f$ [72, 74]. The formed delay representation

$\mathbf{Z}_{k+1}$ must then depend on r previous values of the applied perturbation:

$$\mathbf{Z}_{k+1} = f(\mathbf{Z}_k, q_k, q_{k-1}, \dots q_{k-r}) \tag{3.41}$$

leading to an extended form of the linearization including the dependence on previous parameters:

$$\mathbf{Z}_{k+1} - \overline{\mathbf{Z}}_{k+1} = \mathbf{A}_k(\mathbf{Z}_k - \overline{\mathbf{Z}}_k) + \mathbf{B}_k^{\mathbf{1}}(q_k - \overline{q}) + \mathbf{B}_k^{\mathbf{2}}(q_{k-1} - \overline{q}) \dots + \mathbf{B}_k^{\mathbf{r+1}}(q_{k-r} - \overline{q}) \tag{3.42}$$

where:

$$\mathbf{B}_k^{\mathbf{j}} = \mathbf{B}_{k+p}^{\mathbf{j}} = \frac{\partial f(\mathbf{Z}, q_k, q_{k-1}, \dots, q_{k-r})}{\partial q_{k-(j-1)}} \tag{3.43}$$

Note that all quantities discussed thus far can be approximated solely from discrete data in the system. Matrices $\mathbf{A}_k$ are approximated through typical least squares regression, which is computationally cheap. The collection of matrices $\mathbf{B}_k^{\mathbf{j}}$, $1 \leq j \leq r+1$ are also obtained from the time series by turning on the perturbation to the full prescribed amount at each $(r+1)^{th}$ piercing of the Poincaré section. Then, the method continues identically to the least squares regression estimates of matrices $\mathbf{A}_k$ [75].

To frame the controlled system in a more compact form, the delay coordinate vector $\mathbf{Z}_n$ and the r previous parametric values are incorporated into a new state vector $\mathbf{Y}_k$, where the $\overline{()}$ indicates nominal parameters at the orbit point:

$$\mathbf{Y}_k = \begin{pmatrix} \mathbf{Z}_k \\ q_{k-1} \\ q_{k-2} \\ \vdots \\ q_{k-r} \end{pmatrix} \qquad \overline{\mathbf{Y}}_k = \overline{\mathbf{Y}}_{k+T} = \begin{pmatrix} \overline{\mathbf{Z}}_k \\ \overline{q} \\ \overline{q} \\ \vdots \\ \overline{q} \end{pmatrix} \tag{3.44}$$

This state vector can be formed into a new linearization including both state and parameter dependence between Poincaré piercings [74]:

$$\mathbf{Y}_{k+1} - \overline{\mathbf{Y}}_{k+1} = \widetilde{\mathbf{A}}_k(\mathbf{Y}_k - \overline{\mathbf{Y}}_k) + \widetilde{\mathbf{B}}_k(q_k - \overline{q}) \tag{3.45}$$

Matrices $\widetilde{\mathbf{A}}$ and $\widetilde{\mathbf{B}}$ are redefined as:

$$\widetilde{\mathbf{A}}_k = \begin{pmatrix} \mathbf{A}_k & \mathbf{B}_k^{\mathbf{2}} & \mathbf{B}_k^{\mathbf{3}} & \dots & \mathbf{B}_k^{\mathbf{r}} & \mathbf{B}_k^{\mathbf{r+1}} \\ \mathbf{0} & 0 & 0 & \dots & 0 & 0 \\ \mathbf{0} & 1 & 0 & \dots & 0 & 0 \\ \mathbf{0} & 0 & 1 & \dots & 0 & 0 \\ \vdots & \vdots & \vdots & \ddots & \vdots & \vdots \\ \mathbf{0} & 0 & 0 & \dots & 1 & 0 \end{pmatrix} \tag{3.46}$$

$$\widetilde{\mathbf{B}}_k = \begin{pmatrix} \mathbf{B}_k^{\mathbf{1}} \\ 1 \\ 0 \\ \vdots \\ 0 \end{pmatrix} \tag{3.47}$$

The new $\widetilde{\mathbf{A}}$ and $\widetilde{\mathbf{B}}$ are then used in place of the $(\mathbf{A}, \mathbf{B})$ pairs in the previous control design equations.

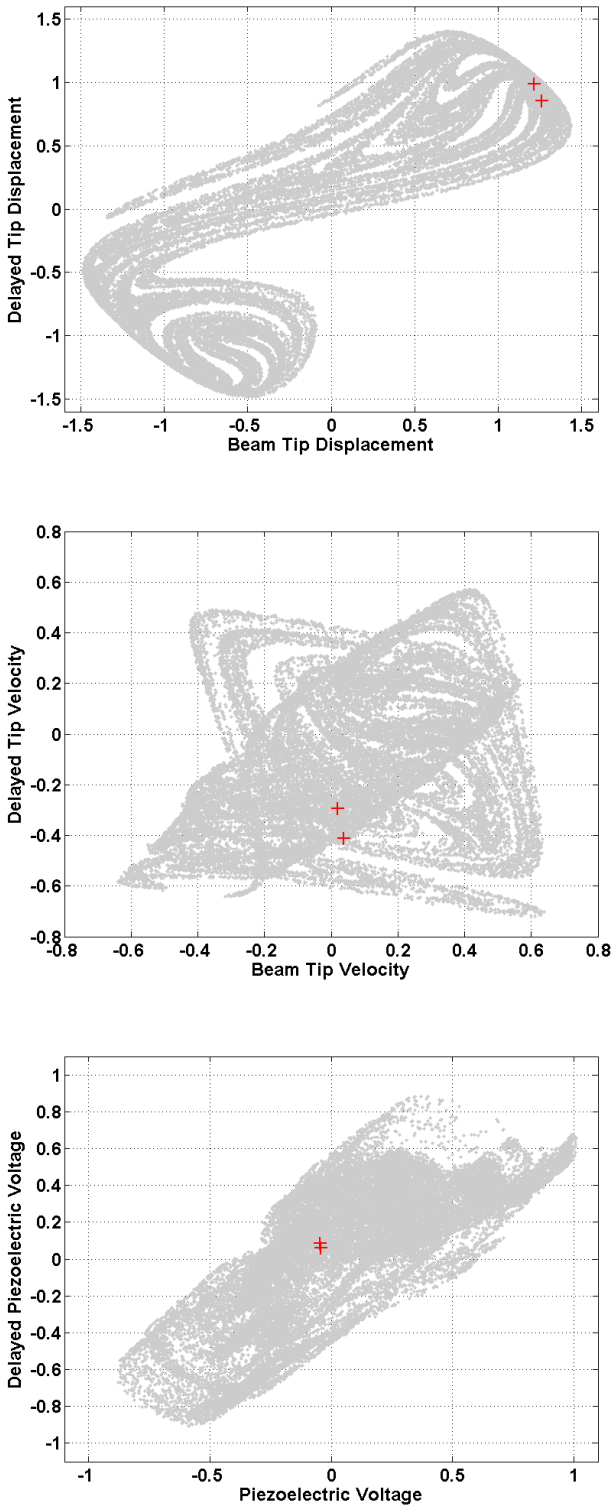

Figure 3.15: Delay reconstruction of the chaotic attractor from individual measured states

The delay reconstruction method is nondiscriminatory with respect to which state is originally used for the embedding. In lieu of measuring displacement and/or velocity of the system, it is possible that the orbit points, local linear models, and control algorithms can be described purely from measurement of the voltage state. Sensing only voltage could reduce device costs and make a chaotic control method more attractive for energy harvesting applications. Figure 3.15 illustrates the reconstruction of a chaotic attractor using each of the three states of the system: displacement, velocity, and voltage, respectively. Unfortunately, without further advancements the recurrence detection algorithm is unable to accurately detect unique period-two orbit points. Nonetheless, this idea is mentioned as a long term goal for additional improvements to chaotic control-based energy harvesting.

3.5 Control Across Attractors

To more readily match the state of the art in current nonlinear bistable-based piezoelectric vibration energy harvesters, a control approach capable of jumping between attractors as opposed to simply optimizing motion within an attractor was investigated. The foundation of the controller centers on tracking the current trajectory of the system against the desirable large amplitude response, then perturbing the system at times of minimal error [65]. For a general non-autonomous system:

$$x'' = f(x, x') + p(t) + u(t) \tag{3.48}$$

where x is the state variable, $f(x, x')$ is the nonlinear system, $p(t)$ represents the harmonic excitation, $u(t)$ represents the external control input and $()'$ is used to denote the derivative with respect to a nondimensional time. It is assumed for the system parameters chosen that multiple stable solutions exist, and the desirable solution can be attained through proper choice of initial conditions

in the absence of control:

$$x_d'' = f(x_d, x_d') + p(t). \tag{3.49}$$

The control technique is a simple tracking controller where state differences can be expressed as:

$$\begin{aligned} e_1 &= x - x_d \\ e_2 &= x' - x_d'. \end{aligned} \tag{3.50}$$

A general error equation can be formulated by subtracting Equation 3.49 from Equation 3.48:

$$e_2' = f(x, x') - f(x_d, x_d') + u(t) \tag{3.51}$$

The intermittent tracking control law is then written as:

$$u(t) = \begin{cases} 0 & |e_1| > \delta \\ -f(x, x') + f(x_d, x_d') - k_p e_1 - k_d e_2 & |e_1| \leq \delta \end{cases} \tag{3.52}$$

where k_p and k_d are positive linear gains of the controller, and δ represents the neighborhood boundary of the displacement error between the actual and desired trajectories. Note only a single error term was needed for sufficient control of the system, but theres no reason the norms of both error terms could not have been included in the analysis [65].

3.5.1 Stability Analysis of the Proposed Control Law

The control law is designed to guarantee asymptotic convergence towards the desired orbit trajectory whenever $|e_1| \leq \delta$ and the control gains are selected properly [65]. To prove stability, the following positive-definite Lyapunov function is formulated dependent on the state errors and

control gains of the system:

$$V(e_1, e_2) = \frac{1}{2}(e_2 + \psi e_1)^2 + \frac{1}{2}(k_p + \psi k_d - \psi^2)e_1^2. \tag{3.53}$$

A positive scalar ψ leads to a sufficiency condition for a positive definite Lyapunov function:

$$0 < \psi < k_d. \tag{3.54}$$

Applying the intermittent control law in Equation 3.52 to the error equation in Equation 3.51 yields:

$$e_2' = \begin{cases} f(x, x') - f(x_d, x_d') & |e_1| > \delta \\ -k_p e_1 - k_d e_2 & |e_1| \leq \delta. \end{cases} \tag{3.55}$$

Taking the time derivative of Equation 3.53 and substituting Equation 3.55 yields

$$V'(e_1, e_2) = (\psi - k_d)e_2^2 - \psi k_p e_1^2 \tag{3.56}$$

for $|e_1| \leq \delta$. The derivative $V'(e_1, e_2)$ is indeterminate for $|e_1| > \delta$. Since the sufficiency condition in Equation 3.54 ensures that ψ is positive and less than k_d, Equation 3.56 is negative definite, guaranteeing asymptotic convergence for the closed loop system under intermittent feedback control. Liu et al. deliver a more in-depth analysis of the proposed controller, with a critical difference being application towards control between two period-one attractors [65]. This work extends the foundation towards application in which one of the system attractors is chaotic in nature.

3.5.2 Controlling the Piezomagnetoelastic System

To efficiently track the desired trajectory in relation to the actual trajectory, the differential equations of motion in Equation 3.3 were transformed into their state-space equivalent and discretized using a finite different technique with step size $\Delta = 0.01$. Discretization easily allows for simultaneous solution of the system for both chaotic motion as well as the desired large amplitude response in MATLAB. The new equations of motion, with the introduction of the control parameter $u(t)$ from Equation 3.52 are then rewritten as:

$$\begin{aligned} x_1(i+1) &= \Delta x_2 + x_1 \\ x_2(i+1) &= \Delta\left(\frac{1}{2}x_1(1-x_1^2) + -2\zeta x_2 + \kappa^2 x_3 + f\cos\Omega t + u(t)\right) + x_2 \\ x_3(i+1) &= \Delta\left(-\lambda x_3 - \gamma x_2\right) + x_3 \end{aligned} \tag{3.57}$$

In order to test the proposed control laws, MATLAB was used to simulate both the chaotic system and the desired large amplitude system. Real time error between the states was calculated, and the control law enabled whenever $e_1 < \delta$. Shown in the next chapter, control is initiated at $t = 250$, with $k_p = 1$, $k_d = 20$, and $\delta = 0.05$. The feedback controller is quick to stabilize the system, yet requires sizable perturbations in its current form, detrimental to the power output of the harvesting system. To mitigate the sizable perturbations required, the control law from Equation 3.52 can be modified to include a maximum allowable perturbation of $u_{\text{max}} = 1$:

$$u(t) = \begin{cases} 0 & |e_1| > \delta \\ -f(x,x') + f(x_d,x_d') - k_p e_1 - k_d e_2 & |e_1| \le \delta \ \text{ and } \ |u| < u_{max} \\ \text{sign}(u) * u_{max} & |e_1| \le \delta \ \text{ and } \ |u| \ge u_{max} \end{cases} \tag{3.58}$$

CHAPTER 4: EXPERIMENTAL DATA AND MODEL VALIDATION

Theoretically, chaos control allows large displacement trajectories to be stabilized from a dense sea of unstable periodic orbits within a chaotic attractor. The three control techniques described all successfully stabilize large displacement periodic orbits from low-energy chaotic oscillations. Two methods are model independent and use time series data to fit a local linear model and apply small perturbations to stabilize a trajectory. The third method uses two identical system models at different initial conditions to simultaneously solve both the chaotic system and the desired large amplitude trajectory. A feedback controller is then used to minimize the error between solutions and perturb the system from the low energy attractor to the more desirable high energy solution.

This chapter first covers the simulation results of the two model-independent controllers for a stable orbit within the same attractor as well as the result of the model-dependent feedback controller with unconstrained and constrained control effort. The latter half of the chapter describes the model validation conducted with a hardware test stand. Because chaotic systems are highly sensitive to their initial conditions, an equivalent solution between theory and experiment is challenging to attain. Instead, validation is confirmed by successful control of different periodic orbits in the theoretical and experimental cases. A hardware test stand is developed from common over the counter components, instrumented, and connected through data acquisition cards to a National Instruments LabVIEW interface. To the best of the authors knowledge, this is the first modular platform for testing chaotic control algorithms.

4.1 Controlled Response Within the Same Attractor

The OGY and sliding mode controllers use different approaches, but both control identical trajectories of the system. Selecting a period-two orbit, recurrence detection from the theoretical time series isolated points:

$$\overline{x}_k = \begin{bmatrix} 0.4394 & -1.2259 \\ -0.4695 & 0.4864 \end{bmatrix}$$

where each column is the displacement and velocity of a single orbit point, respectively. Figure 4.1 illustrates the phase portrait of the chaotic trajectories, the isolated orbit points, and the controlled response from both algorithms.

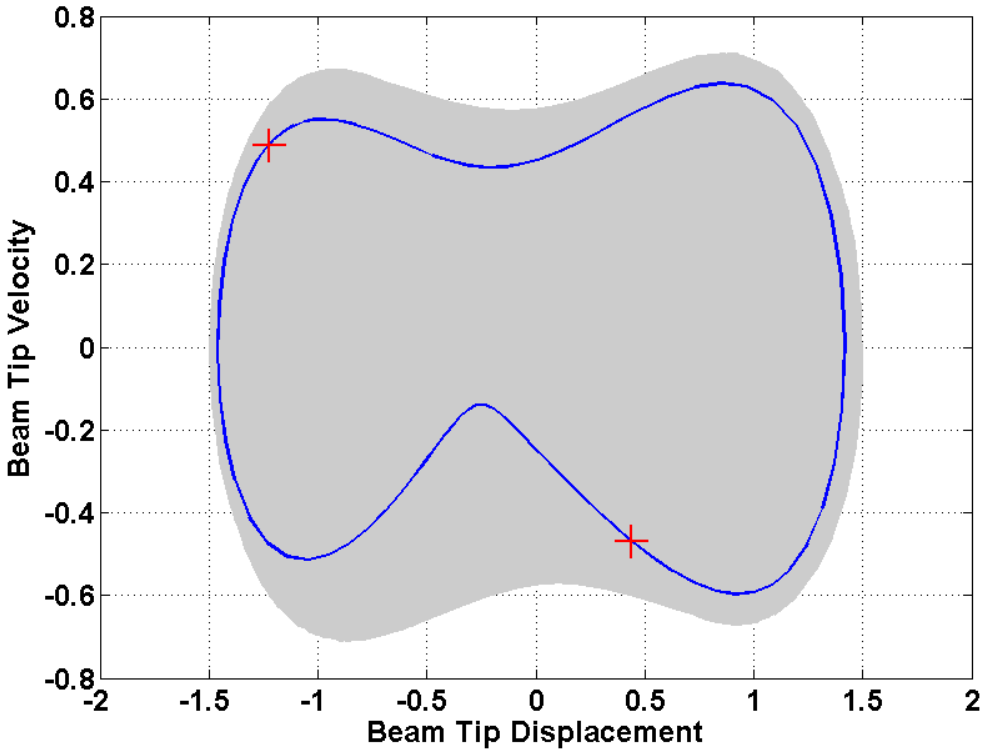

Figure 4.1: A stable trajectory from the chaotic attractor using the model independent control techniques [76, 77]

It should be noted that while the displacement attained is desirable, such a result is not guaranteed in either theory or practice. Recurrence detection isolates the least unstable orbit of a specified period. The controller then ensures that the trajectories pass through these points. Nothing is known regarding the path the trajectory takes between the points and, under the current control paradigm, accounting for specific trajectories would not be possible.

Another caveat of chaos control is the waiting period for the system trajectories to enter the vicinity of the fixed point before any control action is specified. Figure 4.2 illustrates a side profile of the Poincaré section progressing forward in time. Both algorithms attempt to stabilize the same isolated points and trajectory, however, the guiding principles in how the response is attained are fundamentally different. Therefore, not only do stable responses happen over a different time horizon, the steady-state control action post stabilization is different as well. The takeaway from the two control models is that sliding mode control relaxes the need to compute a Jacobian, which is computationally challenging for high-dimensional chaotic systems.

4.2 Control Across Attractors

The third control strategy departs from the previous techniques in that a system model is preserved and control successfully elevates the energy in the system from the chaotic attractor onto the large-displacement attractor. The chaotic solution is computed in parallel to the desired larger trajectory solution, and an error term tracks the difference between the identical states of each attractor. A feedback controller is then used to minimize the error, thus perturbing the system between attractors and stabilizing the large amplitude trajectory from the lower-energy attractor. Figures 4.3 and 4.4 illustrates the phase portrait and time series of the unconstrained and constrained control approaches when control is turned on at $T = 250$ seconds.

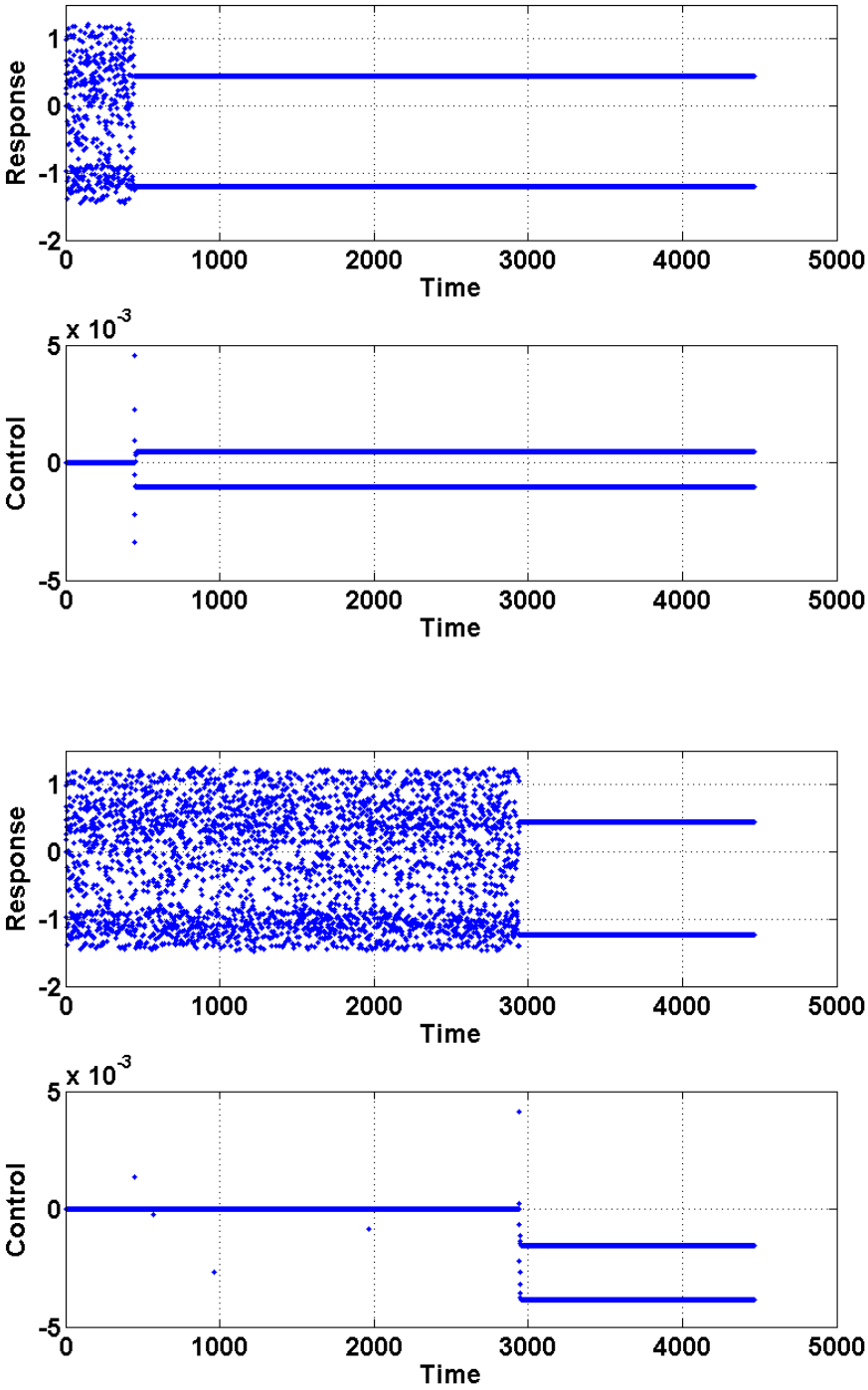

Figure 4.2: Observed displacement compared to control effort for the OGY and sliding mode controllers [76, 77]

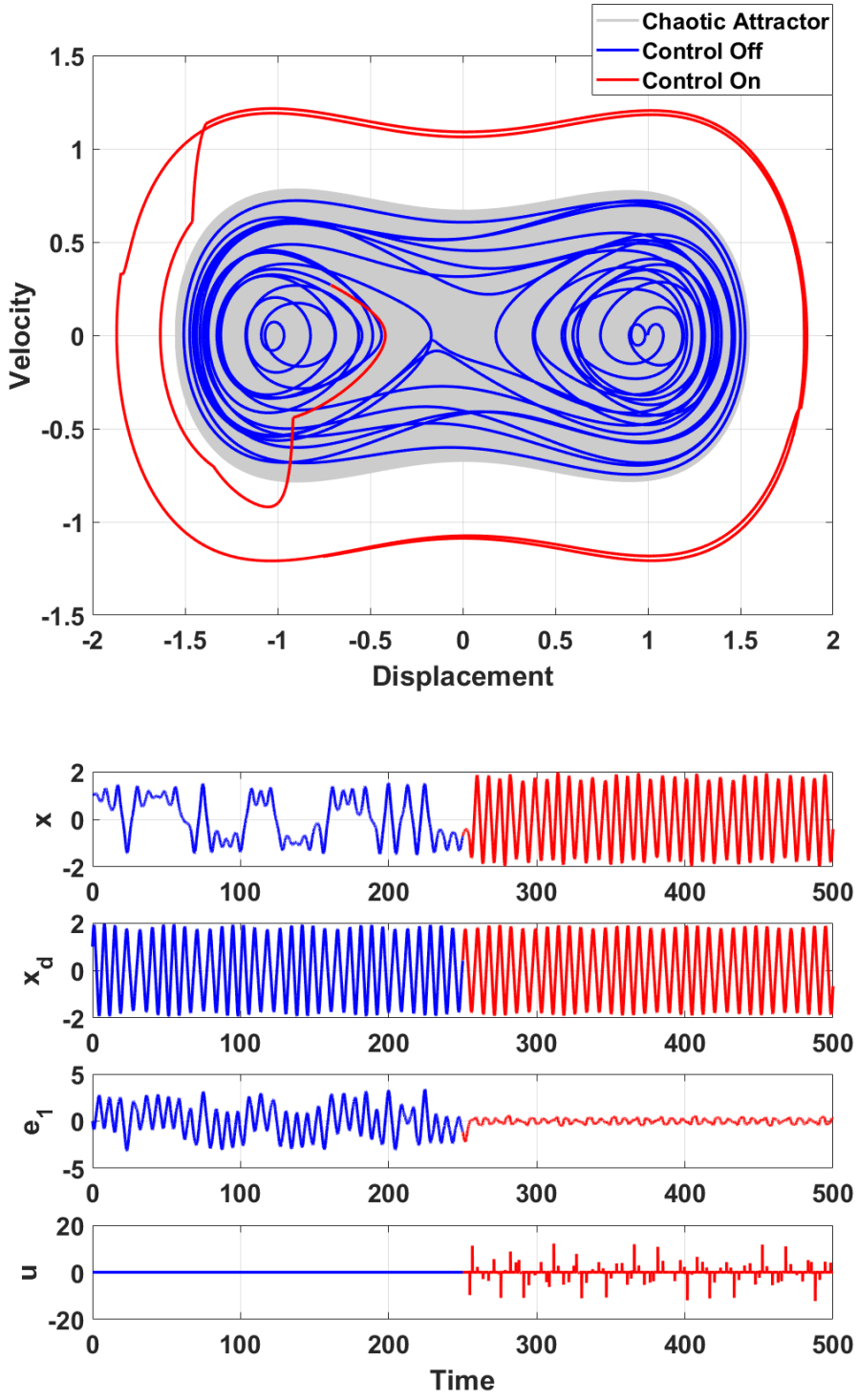

Figure 4.3: Stable response across attractors with unbounded control input [78]

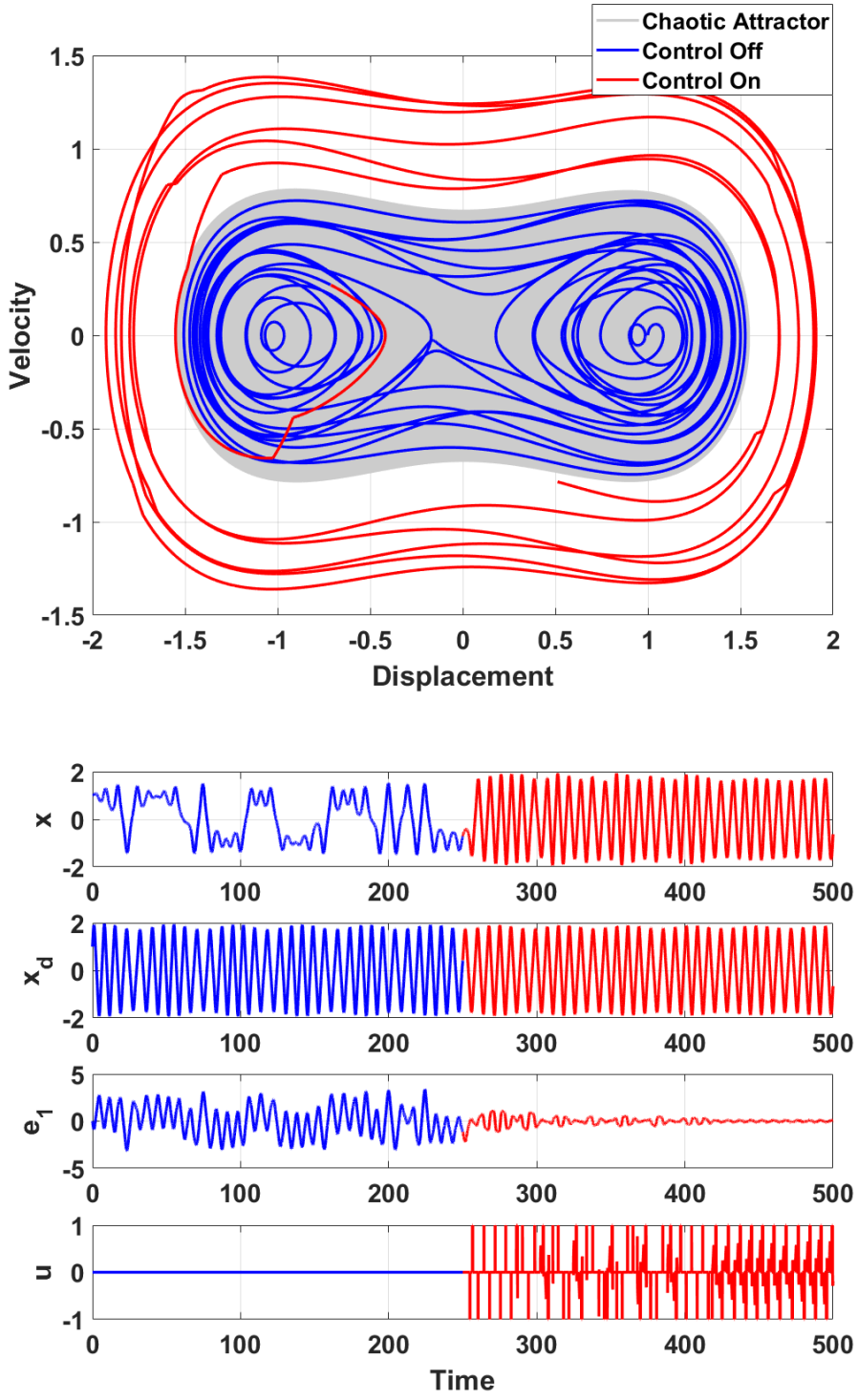

Figure 4.4: Stable response across attractors with bounded control input [78]

As expected when compared to the other control strategies, control perturbations need to be larger to add enough energy to the system to bounce between attractors. Larger perturbations have the inverse effect of reducing the net power output of the harvester, crippling these algorithms in practical use. As an experiment, the control effort was constrained to investigate if a stable response is still attainable. Run under identical conditions, the controller is able to reach the attractor with larger displacement, though the state error decreases over a noticeably longer time horizon. For widespread implementation of this technique, control perturbation would need to be reduced further, and the time series based approximation techniques extended to hybridize the two methods, preserve low perturbations, and remain independent of a system model.

Typically, experimental validation of theoretical findings sets up a system in an attempt to produce identical results to the theoretical cases. However, the nature of chaos makes such a comparison challenging. Instead, an experimental test stand was used to verify the techniques, though the response is not identical and repeatability between runs poses a significant problem. To confirm the validity of a chaotic control algorithm for improved performance of bistable, nonlinear energy harvesters, an experimental test stand was constructed to mimic the lumped-parameter Duffing oscillator model of Equation 3.3. The remainder of this chapter details the hardware used to assemble the bistable structure, bonding of the piezoelectric elements to the ferrous cantilever beam, and the hybrid MATLAB/LabVIEW software elements used for data collection, model approximation, control design, and actuation.

4.3 Experimental Setup

Physical implementation of the harvesting system involves setting up a vertically suspended cantilever beam symmetrically within a magnetic field about the beam tip and instrumenting that beam with sensors and actuators. Then a data acquisition interface is needed to both process the

raw measurements and implement the control law. National Instruments CompactRIO was chosen as the ideal platform for implementation of a real-time controller for the chaotic system. This decision was made when considering the sensitivity of chaotic systems and the requirement for perturbations to be made precisely once per period of excitation. The CompactRIO platform takes advantage of Field Programmable Gate Array architecture that allows an integrated circuit to be reprogrammed and run on an independent processor built into the chassis. This division of labor allows critical components to execute at precise clock speeds leaving the host PC available for low-level computations like visualization and data transfer.

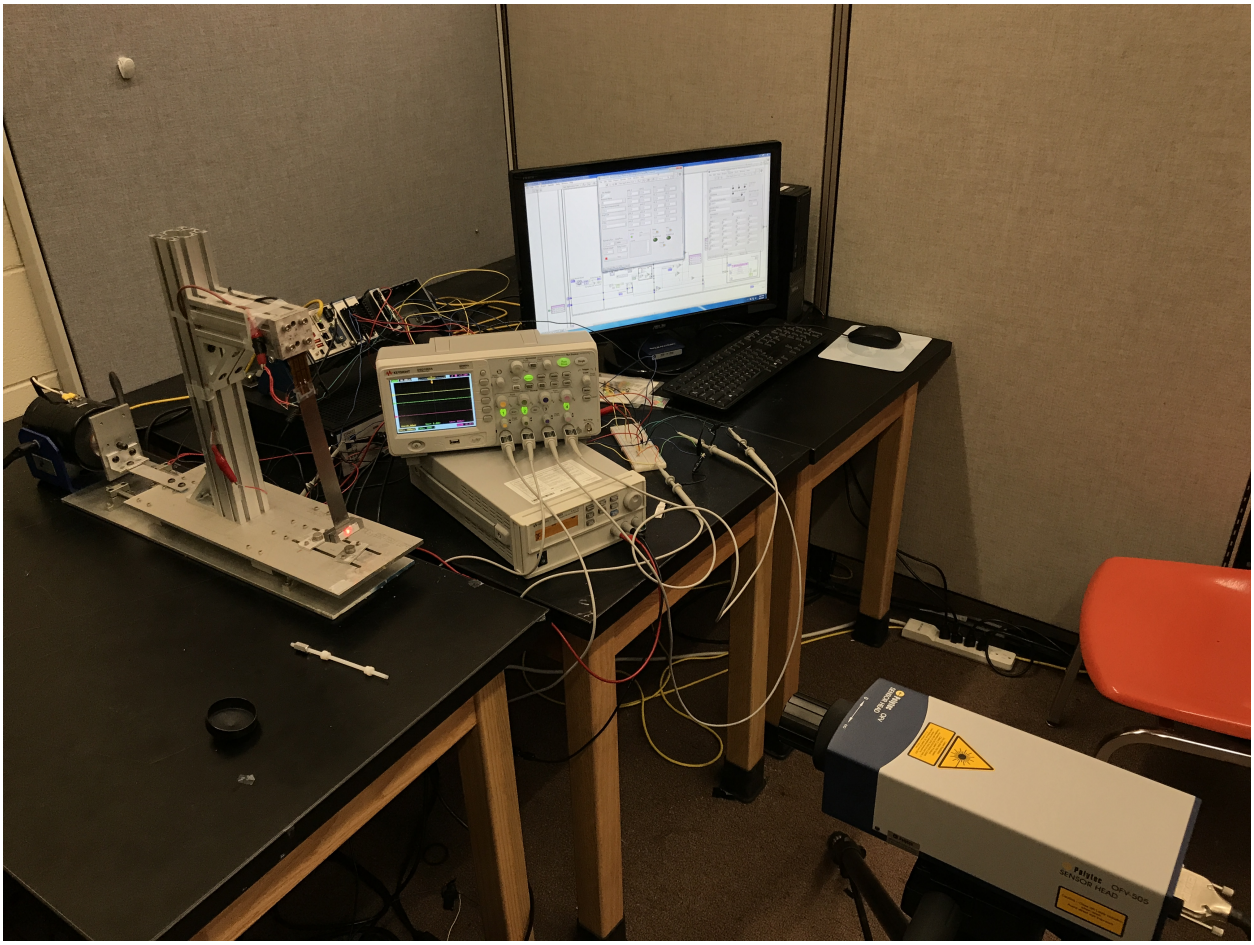

Figure 4.5: The bench top experimental test stand used throughout this work

4.3.1 The Piezomagnetoelastic Structure

The experimental test stand is built similar to Figure 1.6 and uses an aluminum frame to suspend a steel beam vertically between two symmetrically-placed magnets. The vertical orientation of the system eliminates gravity effects in the direction of primary displacement and both beam height and magnet spacing are adjustable to reflect tuning parameters h and d. A proof mass is placed at the tip of the cantilever beam to increase compliance and reduce the natural frequency of the system. Note that while the nonlinear techniques are non-resonant, the system's fundamental frequencies allows the harvester to work at lower frequencies more desirable for the target applications. Two Midé piezoelectric patches are bonded at the clamped end of the beam using a high-shear epoxy and wired together in parallel. The entire assembly oscillates on low friction linear rails, driven by a Modal Shop 2025E shaker powered by the 2100E21 amplifier. A Polytec OFV-505 sensor head and OFV-5000 vibrometer controller is used to measure displacement and velocity at the tip of the cantilever beam. A National Instruments CompactRIO 9035 chassis with NI 9263 analog output and NI 9221/9229 analog input data acquisition cards are used to collect data and produce the required control effort. Figure 4.5 illustrates the bench-top setup. The use of the FPGA again allows a dedicated on-board processor to carry out control-specific computations while the host computer manages the less time-critical data transfer for post-processing and visualization tasks to be performed independently; i.e., at no penalty to the control logic timing. The system is designed to be modular meaning a variety of methods for approximation and control design can computed in MATLAB and input into LabVIEW without changing the interface. The system also allows for relative ease in computing control perturbations for orbits of varying periods. More details regarding the interface is shows in Appendix A.2. Significant effort was placed into preserving a robust, modular system so the working prototype can then be used for rapid implementation of controllers and approximation techniques as subsequent optimization occurs.

4.3.2 Harvesting Circuitry

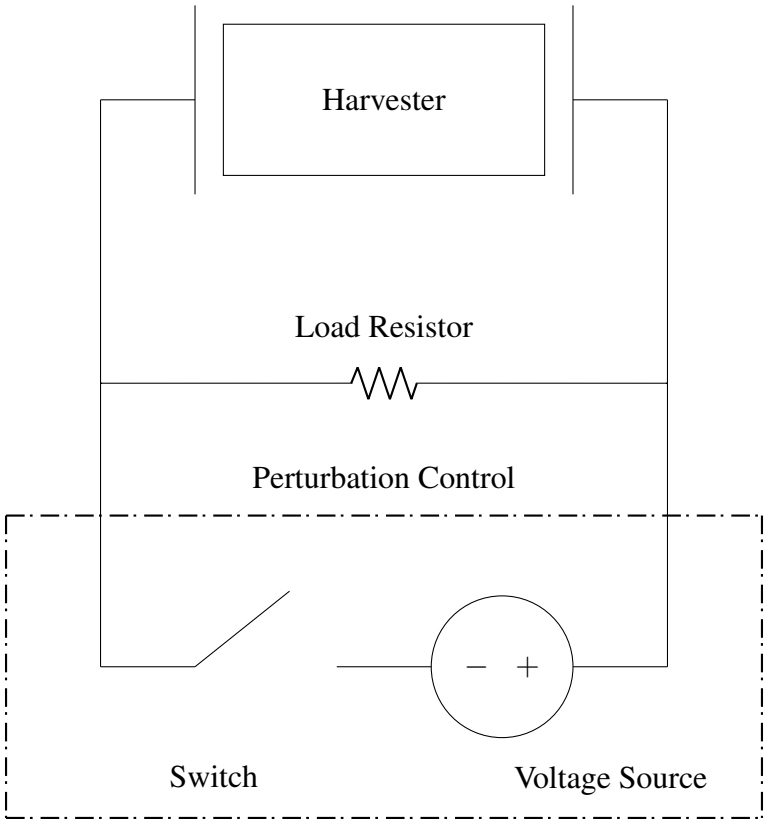

Figure 4.6: Electrical harvesting circuit diagram used during direct perturbation to the load resistance

When benchmarking performance of a piezoelectric energy harvesting, the storage medium is typically represented by the inclusion of a resistive load. Power dissipation across some determined optimal resistance forms the standard performance metric of the harvesting capability for a proposed design [79]. The same format was used when developing the harvesting circuitry for the chaotic system and voltage across this resistor was measured using an input channel of the LabVIEW data acquisition card. Chaotic control of a Duffing oscillator typically applies the control perturbation through the shaker amplitude to stabilize the system [80]. However, this approach is impossible in the current energy harvesting application: to do so would require changing the ambient environment in such a way to control orbits of the system. Instead, a switch-based circuit allows for control perturbations to be moved from the shaker amplitude to the harvesting system

itself. Synced to the harmonic excitation frequency, a switch closes for a short specified amount of time, and a potential difference is introduced governed by the control law. This instantaneous voltage change to the parallel circuit architecture ideally acts as a short transient perturbation to the nominal load resistor. Figure 4.6 shows the schematic for the control circuitry and attached harvesting circuit, which is approximated here with a load resistor.

4.3.3 Experimental Results

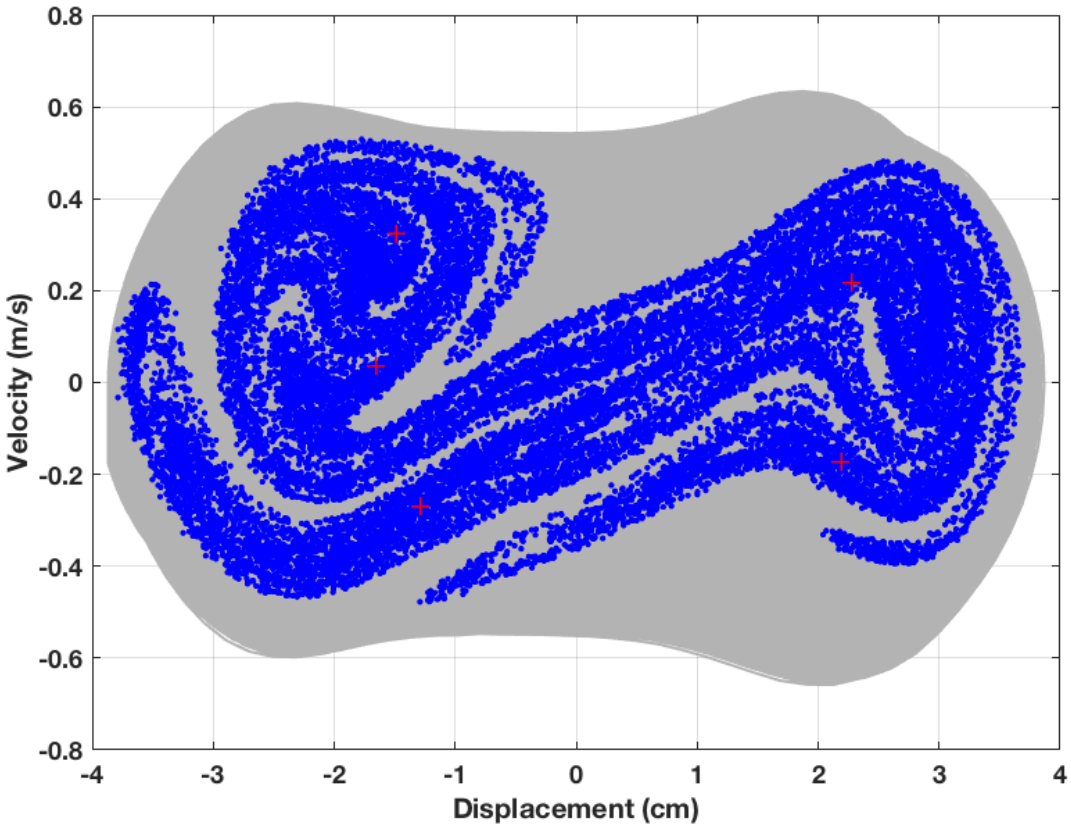

Figure 4.7: Results of recurrence detection from measured time series data of the physical system

The CompactRIO chassis has two analog output cards of different connector types, and one analog input card. The analog outputs of the LabVIEW interface are used to send shaker commands, send

a pulsed DC voltage signal responsible for closing the relay circuit timed to the positive-slope zero crossing of the harmonic input for a fixed duration of time, and apply a dynamic voltage signal computed by the control logic. The analog inputs are used to acquire beam displacement, beam velocity, voltage across the load resistance, and voltage applied to the circuit for control. Under operation, $50,000$ Poincaré intersection points were measured to determine the system model and design a controller under application of a 5 Hz harmonic driving signal. The orbit points determined from recurrence detection and computed control gains are then run in a separate LabVIEW VI with the results shown in Figures 4.8 for a period-5 orbit.

Ergodic wandering of the chaotic system prevents immediate stabilization of the orbit. As trajectories naturally wander into the specified vicinity near an orbit point, the control turns on and stabilizes the system. Figure 4.8 displays one example showing periodic trajectories for all system states. Since the isolated orbit points are computed independent of control application, control via shaker amplitude or circuit perturbations stabilize identical orbits. Controllability is nominally ensured within LabVIEW by determining if the chosen state of the system for control actually results in a controllable system using classic linear control system theory. Figure 4.8 illustrates the phase portrait of the experimental controlled chaotic response. Once the trajectories entered the vicinity of the experimentally isolated orbit points, the period-5 orbit was successfully stabilized for 56 cycles. The perturbations shown in Figure 4.8 emphasizes that the control effort is constrained to not violate linearity of the model around the orbit points.

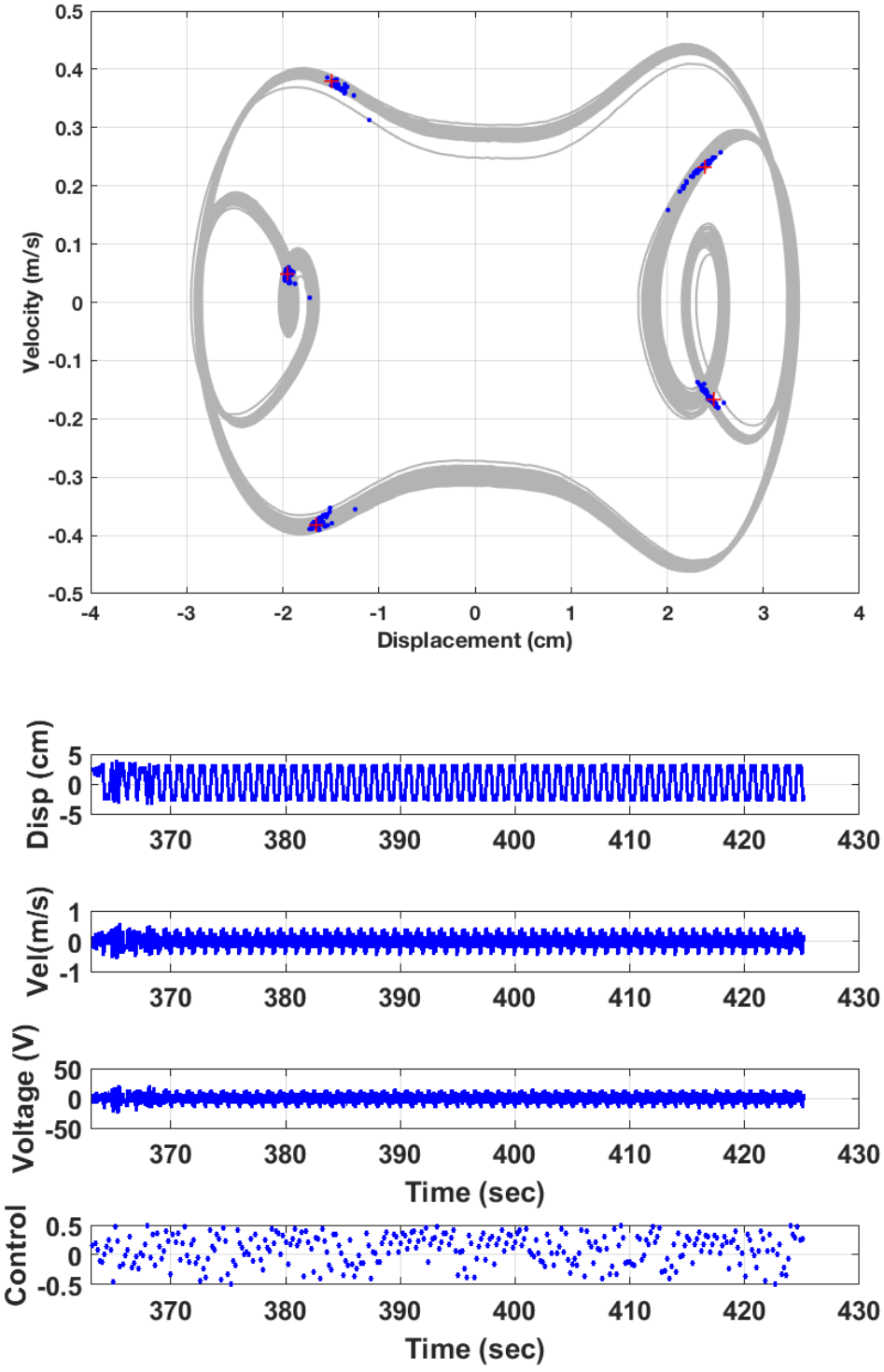

Figure 4.8: Phase portrait and time series of a stable period-5 orbit in the experimental system

CHAPTER 5: CONCLUSIONS AND FUTURE WORK

Piezoelectric-based vibration energy harvesters can successfully be used as a source of power for small-scale sensors across a range of applications. Current harvester technology places small piezoelectric patches at the location of maximum strain on a cantilever beam and uses the ambient environment to induce transverse vibration of the beam. This deflection strains the piezoelectric material, generating charge separation that can be conditioned as power through appropriate circuitry. Cantilever beams are unfortunately limited to peak deflection around the fundamental resonance frequency, reducing potential operating environments to those with known dominant frequencies. Induced nonlinearity has been successful in improving the operating bandwidth, especially when oscillation occurs in the large-amplitude attractor of a Duffing oscillator system. Though commonly ignored, these solutions coexist with a lower-energy chaotic attractor and the desirable solution is not always guaranteed. This work set out to counterintuitively induce chaotic oscillations and then periodically apply a low-power controller to stabilize larger displacement solutions isolated within the attractor. Recurrence detection algorithms in addition to least squares estimation successfully fit a model to time series data of the chaotic system. A controller then selected a perturbation that was applied through both the shaker amplitude and the piezoelectric patch directly. Note relocating the perturbation aligns with a real-world system and the inability to affect change directly to the environment. While nonlinear systems in energy harvesting and chaos control are not new ideas, marrying the methods together had not been explored prior to this research effort. This work stepped through the design challenges of implementing a real-time chaotic control algorithm both through simulation and with a physical test stand. The experimental system marks the first effort of building a modular platform for rapid prototyping of various chaotic systems and control strategies.

No singular research effort is truly exhaustive and significant questions remain. This work set the

groundwork for an energy harvesting strategy not previously considered. It is not an omission on behalf of the author to fore go power computations in a work detailing performance improvements of vibration based energy harvesters. While literature exists describing power expectations in each solution attractor of a nonlinear energy harvester, these analyses would not be complete when accounting for power expended by the control logic itself [58]. Further work is needed in quantifying power expenditure for recurrence detection, model fitting, and control application for each algorithm considered. Power usage is also dependent on the micro-controller selected, and various implementations of the hardware would need to be studied and quantified before a representation power profile of the chaotic nonlinear energy harvesting can be given. Instead, the key research findings and remaining questions are outlined both stating the successes of this study and parallel accomplishments needed before power output can be quantified and widespread implementation of the proposed energy harvester is possible.

5.1 Key Research Findings

5.1.1 Large Amplitude Responses are Attainable from Chaotic Attractors

In the energy harvesting literature, chaos is typically ignored as the aperiodic oscillations result in less accessible energy than the coexistent large-amplitude attractor. More so, even very low intrawell periodic oscillations are preferred over chaotic oscillation as harvesting circuitry requires a periodic voltage signal for optimal operation. A cornerstone of this work is to embrace the sensitivity inherent to chaotic systems. Between the three algorithms presented and implementation of a physical test stand, various large displacement periodic trajectories were stabilized both in and out of the chaotic attractor for improved performance of the vibration response in low-energy ambient environments. Recurrence detection isolates the least unstable orbit of a specified period, and control ensures trajectories pass through those points as indicated by the Poincaré map. It is therefore

not possible to enforce the trajectory taken by the system between orbit points. If an interwell response is attained, displacement is ensured to be larger than both intrawell periodic motion and an equivalent linear harvester excited away from resonance. Larger periodic displacements yield more power from the harvester due to larger strains across the piezoelectric element and also preserve periodicity requirements of the harvesting circuitry. Preservation of a dynamic model when controlling across attractors solves the trajectory limitations by using a feedback controller to minimize the error between the existing trajectory and the desired large displacement orbit. While the true optimal response is attained for nonlinear harvesting systems, a continuous controller utilizes more power in sensing, and the energy injection required to jump between solution attractors can be quite large.

5.1.2 A Model Independence Solution Reduces Tuning before Implementation

Linear, resonant, vibration energy harvesters must be tuned to a dominant frequency in the environment. Inherently low damping for thin beam cantilever systems allows for large oscillations of the beam tip, but a narrow band of operating frequencies. Shifting to a nonlinear strategy that benefits from chaos largely reduces any prior tuning. Chaotic motion typically exists across a wide spectrum of the frequency response, and all multistable systems will pass through chaos at lower frequencies than the desired large-amplitude response studied in the literature [81]. With chaotic oscillations ensured, a key strength of this work is the reduction of tuning due to model independence of the control strategy. Time series data about the system is used with recurrence and least squares approximation techniques to isolate the orbit points, fit a local linear model in a small vicinity of each orbit point, and perturb the system from its unstable manifold onto its stable manifold.

5.1.3 Experimental Chaos Control is Achieved through A Modular Platform

The literature mentions experimental control techniques, but none to date has outlined an exact sequence of steps needed to build a real-time chaos controller [20, 80]. With LabVIEW FPGA the real-time chaotic system can be controlled through a dedicated clock not tied to the host computer's processor. The separate processor ensures the periodic perturbations occur exactly when needed in time with the harmonic excitation of the environment. Time delays in the control application are prone to exist when the controller is fighting for resources with an operating system and, when coupled with sensitivity inherent to chaotic systems, can worsen performance and prevent convergence to a stable response. Splitting the LabVIEW interface into two experiments allows data acquisition and control application to be separated. The first experiment gathers data for a specified number of periods tied to the rising edge of the harmonic excitation zero-crossing. This VI then writes data to a file that can be used through the various MATLAB functions that specify control. A second VI reads the derived control law while running the same data acquisition to stabilize the system onto a more desirable trajectory. Since the controller accepts gains and orbit points, the user can use any technique of their choosing for these independent computational processes. The result is a fully modular platform for chaos control with direct application towards piezoelectric vibration energy harvesting.

5.2 Remaining Questions

5.2.1 Iterative Learning can Reduce Time to Control

The algorithms used in fitting a model require a large number of data points sampled once per excitation period for operation. In a simulation environment, this task can be seen as trivial as 10,000 data points can easily be generated. Shifting to an experimental platform at low frequen-

cies, 10,000 data points at a 5 Hz excitation frequency is not an inconsequential amount of time. Harvesters under the current framework would need more than 30 minutes before enough data was gathered to fit an initial control. The controller would then require an unknown additional amount of time before the trajectories approached a vicinity significantly close to the isolated orbit. Such preprocessing for a system meant to power itself using large-amplitude oscillations could pose a problem to any initial on-board temporary power source. Developing algorithms that can fit control to an iteratively growing data set can likely expedite attempts at a stable response, and also more readily update to changing environmental conditions over time. Incorporating work in machine learning and neural networks can teach these algorithms to better recognize orbit candidates and reduce the time horizon needed for a controlled large displacement response. Also, while the targeted environments are non-resonant, implementation still depends on sampling aligned with a harmonic excitation. Further research into stochastic systems can lead to new sampling techniques, further reducing the dependence on any sort of regularity in the ambient environment.

5.2.2 Optimization is Required to Ensure Repeatability

Chaotic attractors form as a result of stretching and folding in the phase portrait trajectories over time. The chaotic attractor is a consequence of the system being both stable and unstable, and as a result yield unpredictable trajectories at any specific instant in time. Ergodicity of the attractor, however, ensures all possible trajectories within a finite region of the phase portrait are traversed in finite time. In simulation, MATLAB solvers execute repeated runs more accurately only limited by rounding accuracy across machines. In reality, however, the system does not start from an identical initial condition between runs. Thus two consecutive runs can take vastly different trajectories while still remaining within identical attractors. The potential for divergence impedes model approximation for control and inhibits consecutive stable orbits from being attainable. The recurrence detection algorithm proved robust in finding period-five orbits repeatedly in the same

vicinity over the $10,000$ data points collected. A stable result based on similar prediction was not guaranteed within the time horizon as small disturbances can affect the ergodic wandering prior to control and thus ensure control action is not implemented within the time horizon studied. Therefore, even if repeated runs isolated the same orbits, disturbances unique to each run can delay the trajectories from entering the vicinity of the isolated orbit points. To combat this, future work in iterative learning may alleviate this challenge, and the addition of targeting techniques can force trajectories to desired regions of the phase space where control can be successfully implemented.

5.2.3 Real-Time Selection of the Control Strategy can Improve Bandwidth

When chaotic dynamics exist uniquely in the system, the chaos control strategy presents the only way of reaching an optimal condition for energy harvesting. When chaotic solutions exist concurrently with large-amplitude periodic solutions and low-energy periodic intrawell solutions, chaos control provides a way to ensure an optimal response is attained, regardless of the attractor the system originated in. Bifurcation analysis proves that there are frequency bands where only a single attractor exists, and it may be chaotic or interwell periodic. It has been shown that interwell periodic responses are optimal whenever possible and an algorithm has been presented in this work to bump trajectories into the higher-energy attractor. In highly dynamic environments attractors may be created and destroyed, and a truly optimal system needs to account for this. Should large-amplitude interwell solutions exist uniquely, then no active control is needed. If both attractors exist concurrently, the techniques documented herein can mitigate the issue of low-energy chaotic oscillation. Should chaos exist uniquely, as is common at very low frequencies, than again the methods presented in this research can optimize the final trajectory. Should these situations become interchangeable, it would be ideal for the algorithm to sense this and adapt ensuring that the optimal periodic orbit is always present.

5.2.4 The Perturbation Circuitry Warrants Parallel Improvements

This work performed direct perturbation of the piezoelectric element through a switch circuit timed to the excitation period using a LabVIEW data acquisition card to provide the positive or negative voltage. For widespread implementation, a robust data acquisition system will likely not be accessible and perturbations will need to be handled solely at the device level. Additional components like capacitors will need to be added to the device allowing for both energy injection and energy drain as specified by the control logic. Shunting is an active research topic in the piezoelectric smart material community, but proper implementation of this technique would require variable shunting and energy injection within a finite bound..

5.2.5 Power Drain from Control Must be Quantified

Though not a primary focus of this work, power output remains the most important metric of a technique's success in the energy harvesting community. There are well known publications demonstrating that the large-amplitude periodic orbit yields an average voltage output three times larger than an equivalent linear system under the same operating conditions. Chaotic oscillations without control have a larger instantaneous voltage, but a similar average voltage to a linear harvester. Control of these trajectories to a large periodic orbit within the attractor is theorized to possess an average voltage twice that of the linear system. At present claiming this as fact is trivial at best as the output voltage does not take into account power drain needed by the active control element itself. Using LabVIEW for data acquisition and actuation allows for a flexible platform, but does not make quantifying power a straightforward problem. Sensing position and performing low-level computations to fit a local linear model require power and are ultimately dependent on the processor used. Applying the perturbation again requires power and is connected to where the perturbation is made, and what upper bound is placed on the system. There is no "one size

fits all" technique for control implementation and future power comparisons will likely be dependent on the hardware used. That said, it is still an important issue to quantify before widespread implementation of the documented techniques in piezoelectric-based energy harvesting.

APPENDIX A: ILLUSTRATIONS OF THE EXPERIMENTAL TEST STAND

A.1 Hardware Assembly

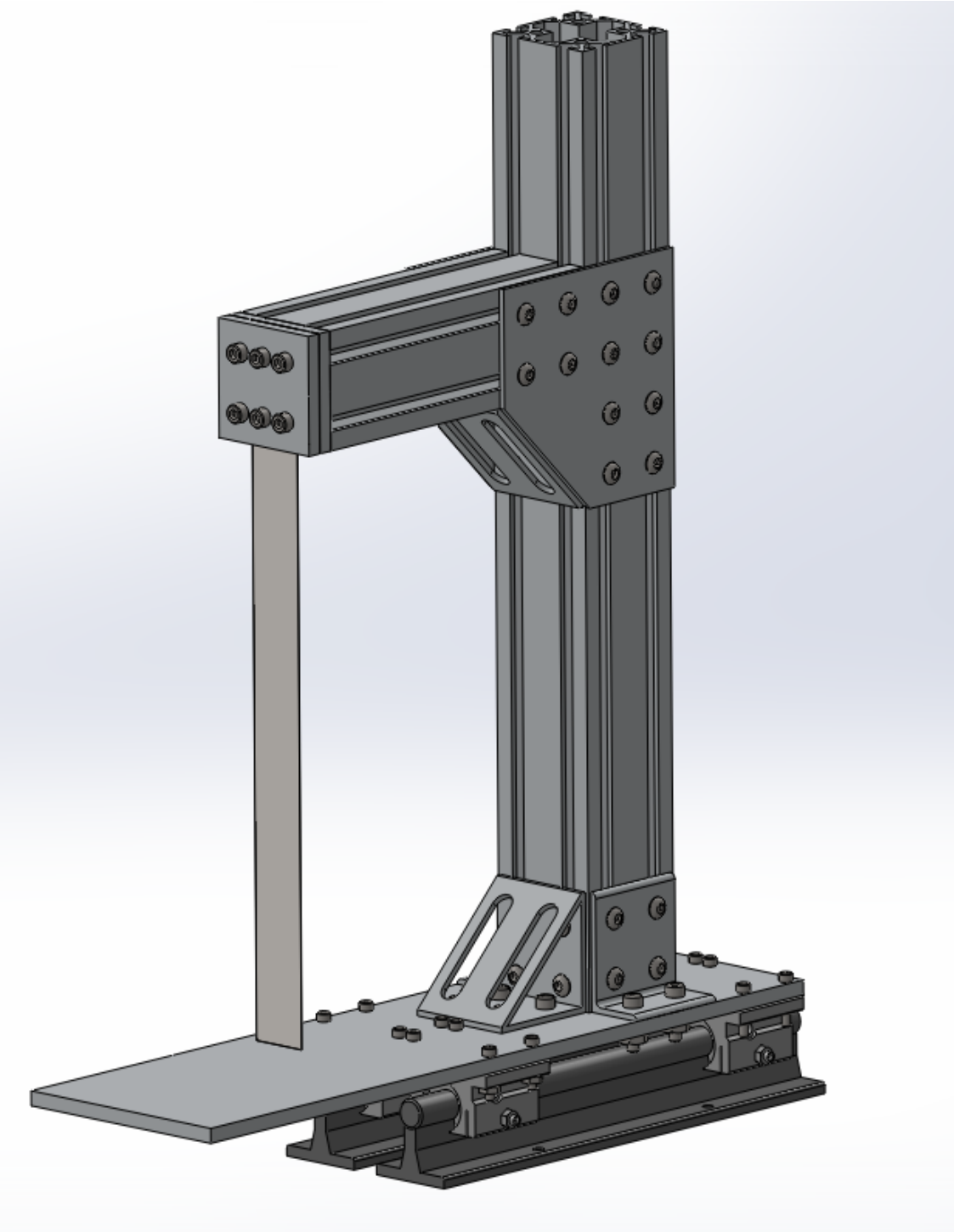

Figure A.1: Three dimensional rendering of the experimental test stand used for the development of the physical harvesting system

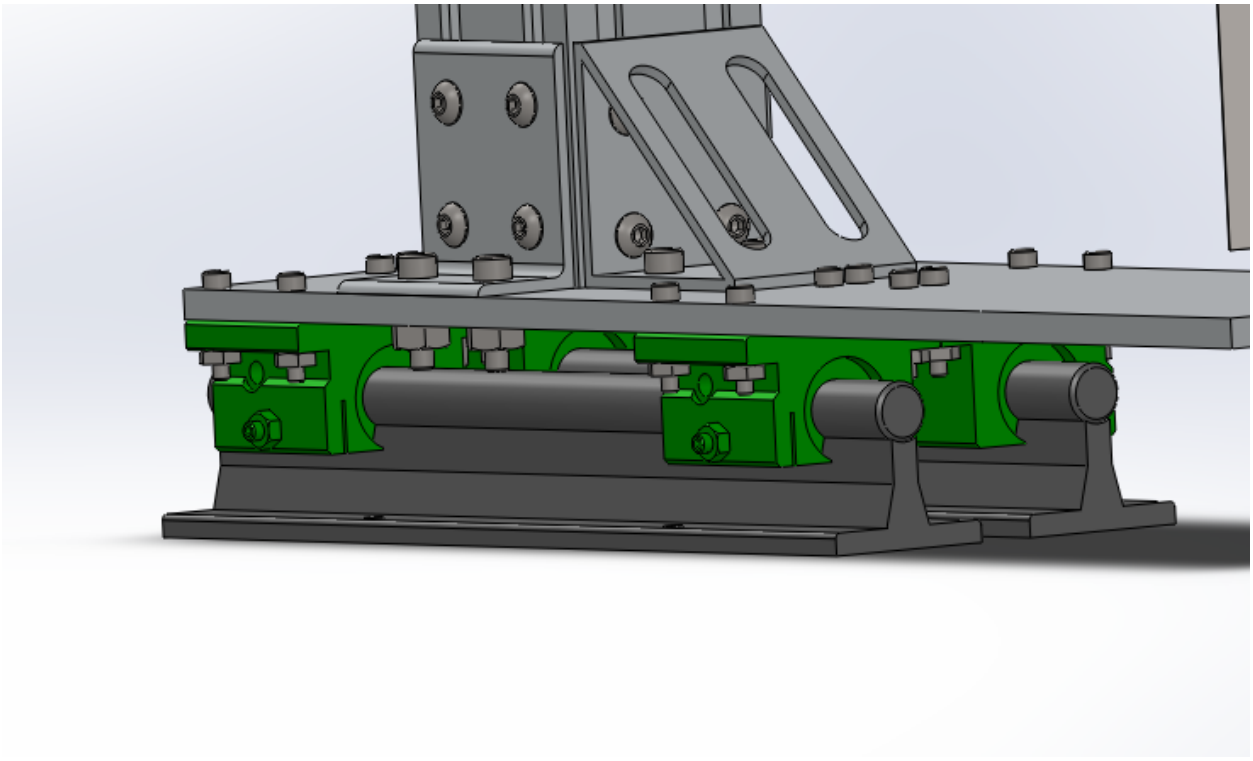

Figure A.2: Three dimensional rendering of the low-friction linear rails used to constrain displacement of the frame in a purely transverse direction

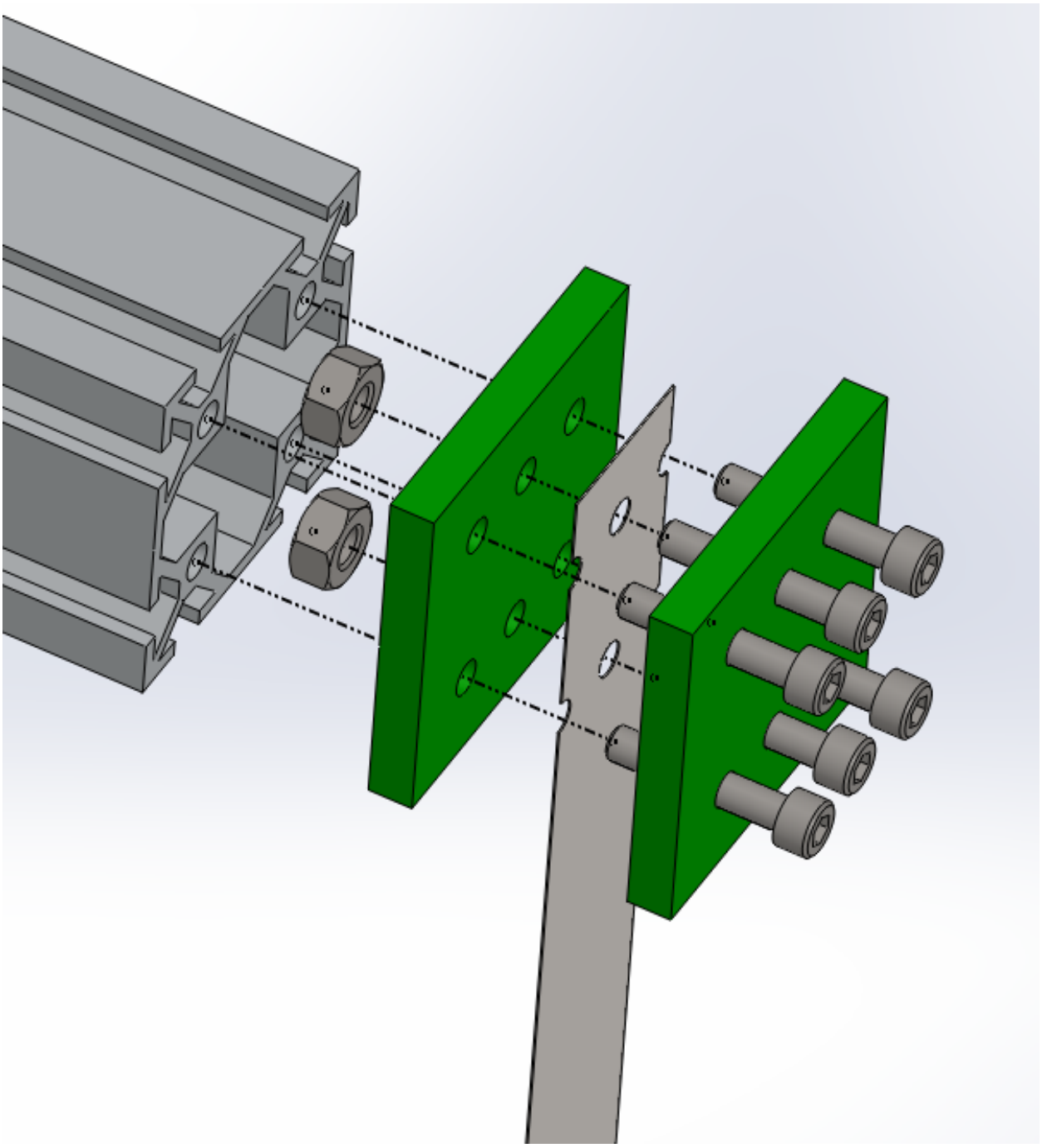

Figure A.3: Three dimensional rendering of the clamped end of the beam simulating base excitation of the harvester

A.2 LabVIEW Interface

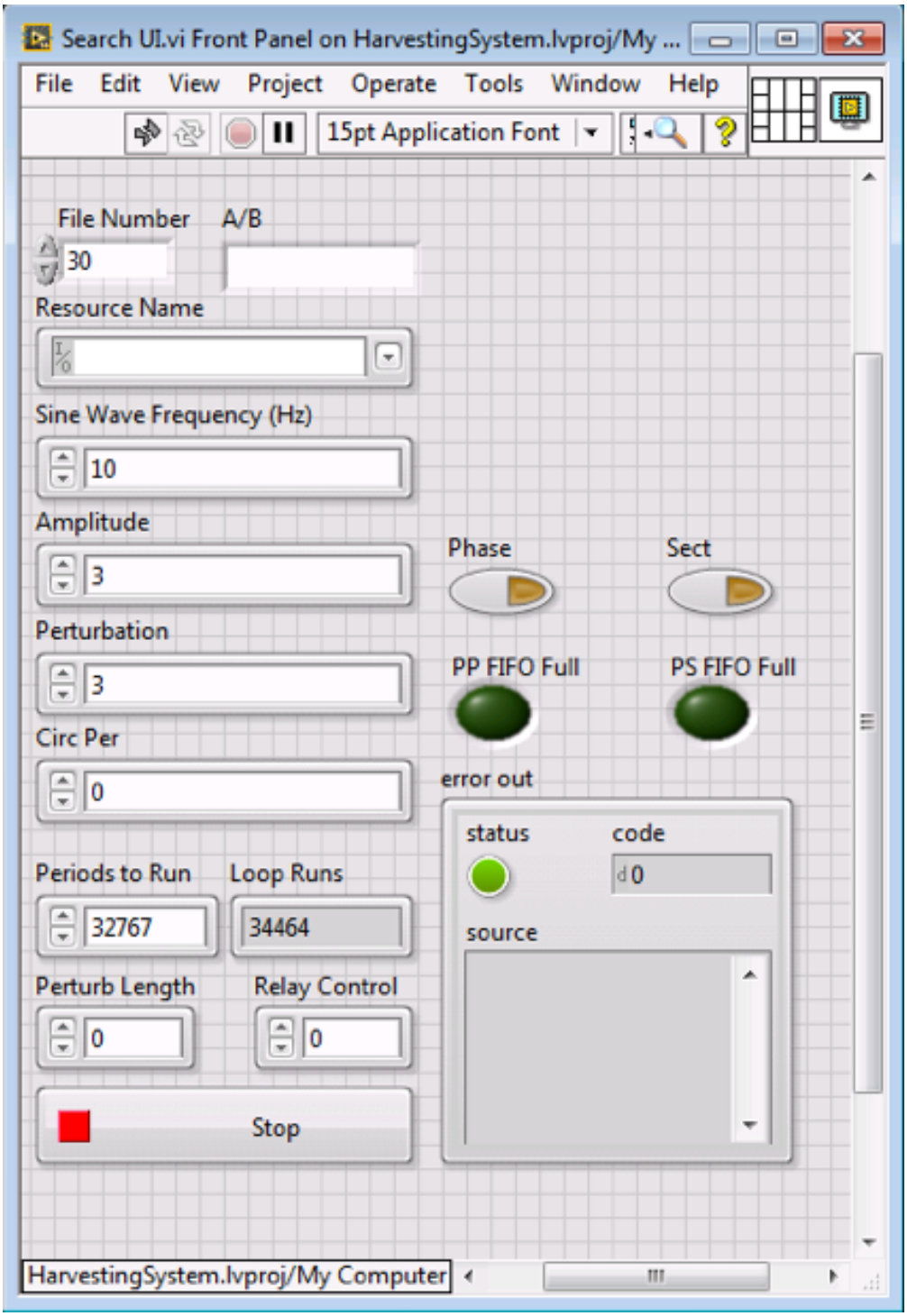

Figure A.4: Front Panel of the LabVIEW VI used in acquiring time series data for further processing in MATLAB

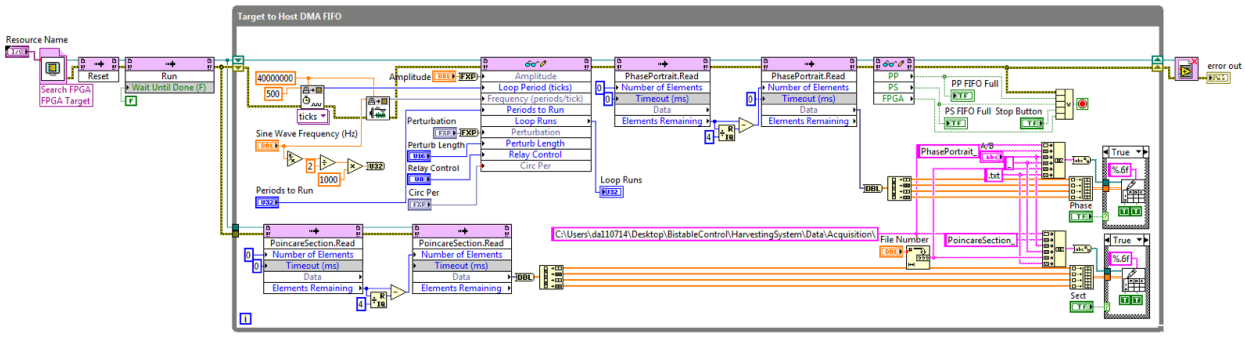

Figure A.5: LabVIEW graphical programming logic for the front panel display during acquisition

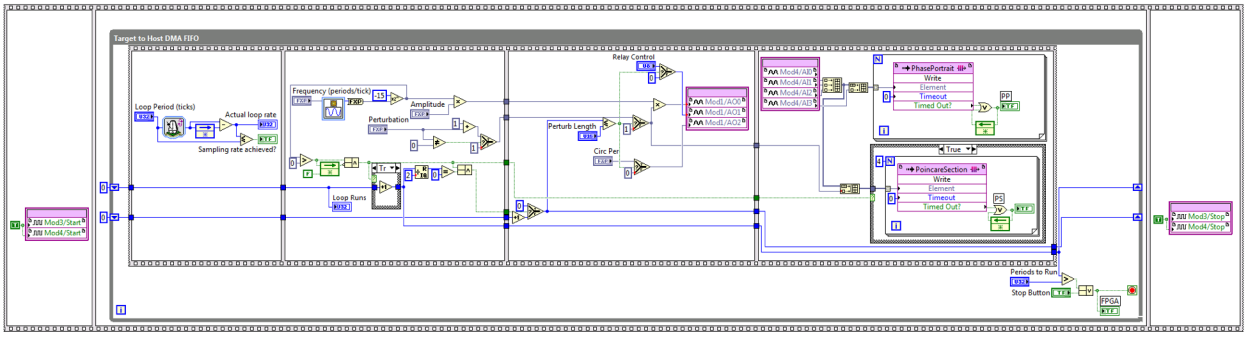

Figure A.6: LabVIEW FPGA VI for data acquisition

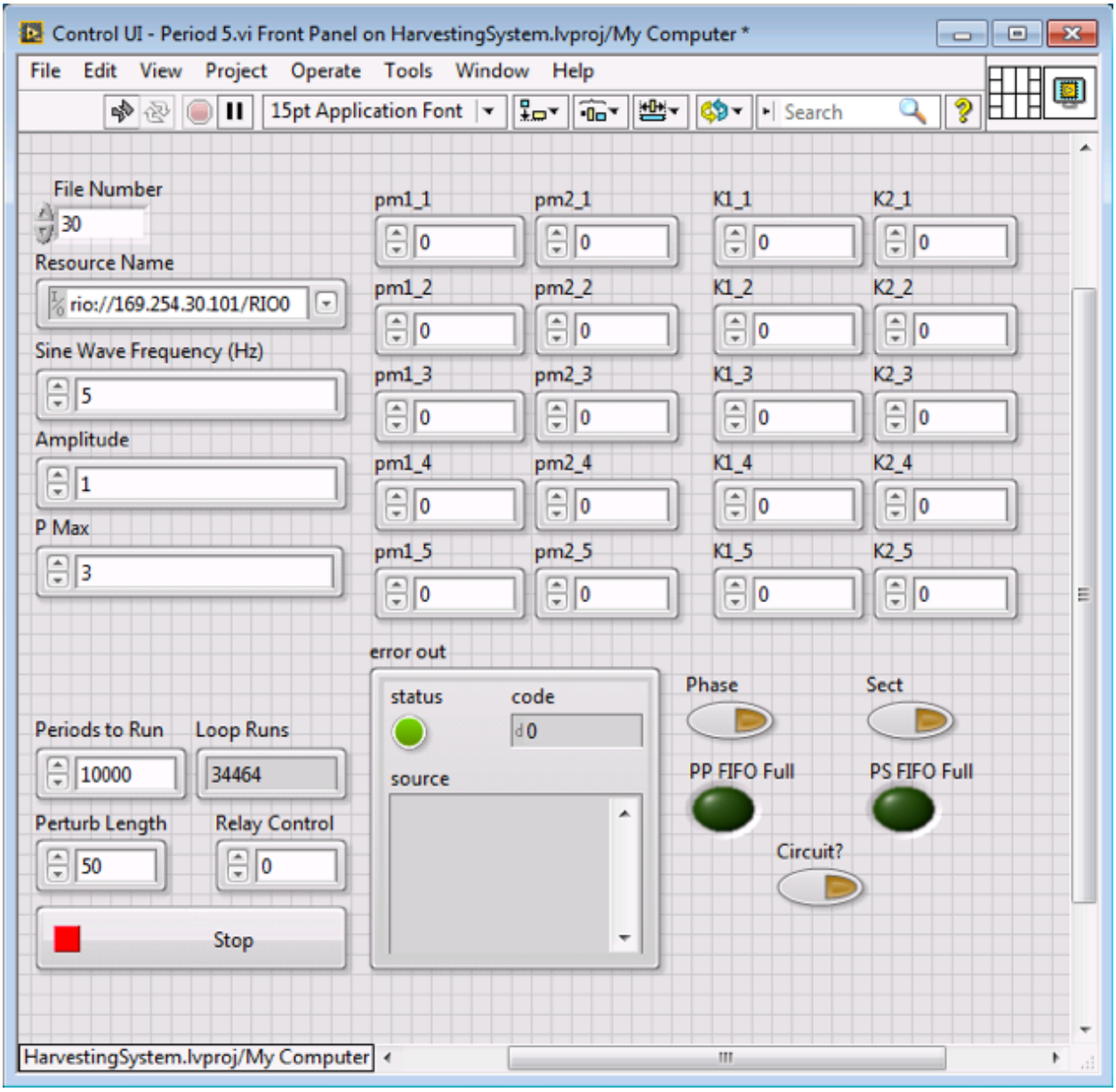

Figure A.7: Front Panel of the LabVIEW VI used in control of a period-5 orbit

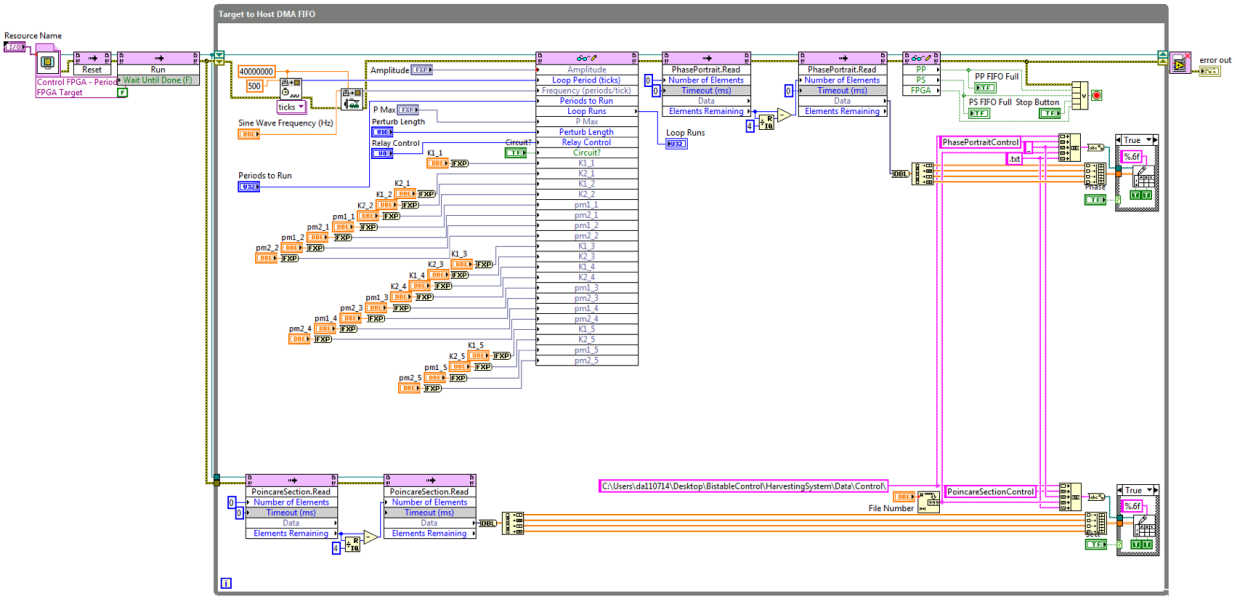

Figure A.8: LabVIEW graphical programming logic for the front panel display during control

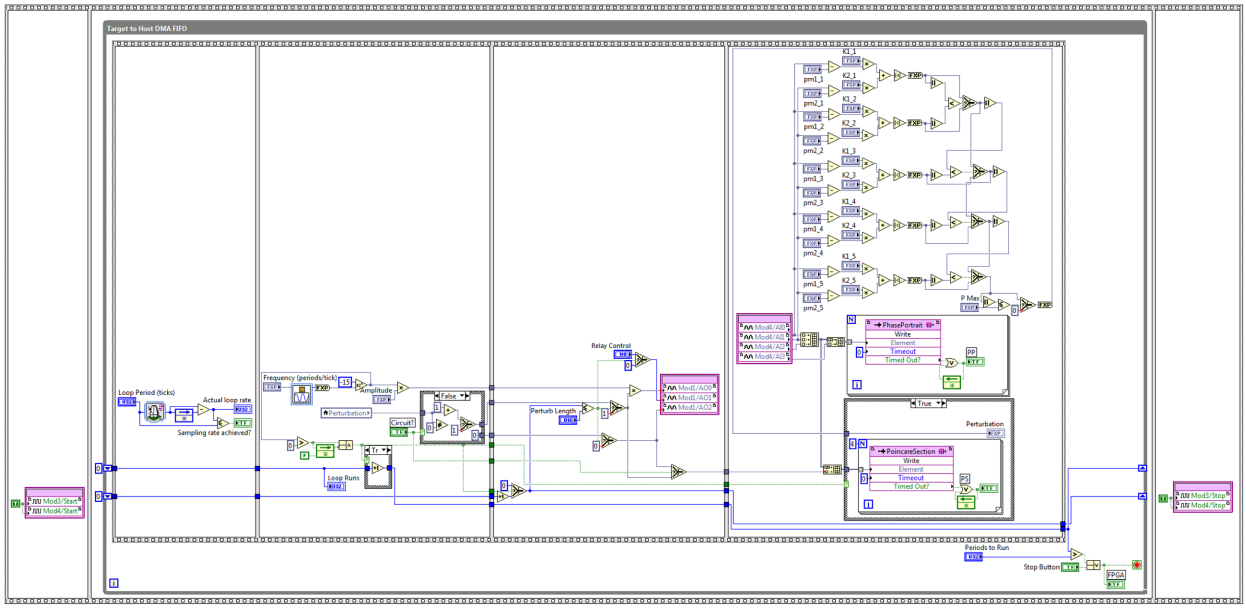

Figure A.9: LabVIEW FPGA VI for control of a period-5 orbit

APPENDIX B: MATLAB SCRIPTS

B.1 General analysis functions

B.1.1 Solving the system of ordinary differential equations both with and without control

```
1  function dx = Duffing(t,x,u)
2
3  % Represents the continuous time system in state-space form
4  % Inputs are initial conditions and the time step vector and
       perturbation
5  % Outputs are the three state equations derivatives
6
7  % zeta: mechanical damping ratio
8  % kappa2: coupling coefficient
9  % gamma: length scaling coefficient between electrical/mechanical
       subsystems
10 % lambda: reciprocal of time constant
11 % omega: excitation frequency
12 % f: excitation amplitude
13
14 global omega gamma lambda kappa2 zeta f
15     dx = zeros(3,1);
16     dx(1) = x(2);
17     dx(2) = f*omega^2*sin(omega*t) - 2*zeta*x(2) - 0.5*x(1)^3 +
           0.5*x(1) + kappa2*x(3) + u;
18     dx(3) = -lambda*x(3) - gamma*x(2);
19 end
```

B.1.2 Determining a Poincaré section through periodic sampling

```
function [Dx, Dy, Dz] = Poincare_Time(x, t, omega, C)
%Poincare
%   Computed the Poincare section from a dataset x
%   omega: excitation frequency
%   C: starting point within first period for sampling

i = 1;
l = 1;
%Input C represents the starting point along the wavelength
%Omega is the forcing frequency of the Duffing Oscillator
%Section computed by progressing forward in time
period = (2*pi)/omega;
k = 0;
if 0 <= C <= period
while i < length(t)-1
    %Compare sign of current and future point, only concerned
       when not
    %equal
     if sign(t(i) - (period*k + C)) ~= sign(t(i+1) - (period*k + C
        ))
         %If first point positive and future point at C
          if sign(t(i) - (period*k + C)) == -1 && sign(t(i+1) - (
             period*k + C)) == 0
              %Creates new variable storing point coordinate on
```

```
                section
22              Dx(l) = x(i+1,1);
23              Dy(l) = x(i+1,2);
24              Dz(l) = x(i+1,3);
25              l = l + 1;
26              k = k + 1;
27          elseif sign(t(i+1) - (period*k + C)) == 1
28              %If first point positive and second point negative
29              %Add to section variable by interpolating value at C
30              Dx(l) = x(i,1) + (x(i+1,1) - x(i,1))*(((period*k + C)
                    -t(i))/(t(i+1)-t(i)));
31              Dy(l) = x(i,2) + (x(i+1,2) - x(i,2))*(((period*k + C)
                    -t(i))/(t(i+1)-t(i)));
32              Dz(l) = x(i,3) + (x(i+1,3) - x(i,3))*(((period*k + C)
                    -t(i))/(t(i+1)-t(i)));
33              l = l + 1;
34              k = k + 1;
35          end
36      end
37      i = i + 1;
38  end
39  else
40      sprintf('Entered start point is larger than 1 period, enter a
            start point less than %d.', period)
41  end
```

B.1.3 Recurrence detection to isolate points of an unstable periodic orbit

```
function pm = RecurrenceMethod(data,m,eps)

%   data: Three time series states of the harvesting system
%   m: desired periodic orbit to consider
%   eps: vicinity around each orbit point to consider as recurrence of
%        future orbit points

dim = 3;
xrange = max(data(1,:)) - min(data(1,:));
yrange = max(data(2,:)) - min(data(2,:));
zrange = max(data(3,:)) - min(data(3,:));

% Loop through Poincare data and determine if successive points are in the
% vicinity set above. If the norm fulfills the criteria, store the period
% into a sparse matrix. Break the loop once desired period is reached.

veld = zeros(1,length(data));

for i = 1:(length(data)-1)
    for j = i+1:length(data)
```

```
21          ddata = data(:,i) - data(:,j);
22          ddata = [ddata(1,:)/xrange ; ddata(2,:)/yrange ; ddata
               (3,:)/zrange];
23          crit = norm(ddata,2);
24
25          if crit < eps
26              veld(1,i) = j-i;
27              break
28          elseif j-i >= m
29              break
30          end
31      end
32  end
33
34  % For each period, separate out all the recurrent points specific
        to that
35  % period in the matrix rec. rec_num is only used after all 15
       periods are
36  % sorted to make a histogram plot of recurrence points.
37
38  for period = 1:m
39      [i,j] = find(veld==period);
40      for n = 1:length(j)
41          rec(1,n) = j(n);
42          rec(2:dim,n) = data(:,j(n));
```

```
43      end
44  %       rec_num(period) = length(j);
45
46      % This section systematically steps through the recurrent
            points
47      % finding the longest sequence of indices. If an initial
            sequence is 2
48      % elements, but a later one is 5, the initial sequence is
            overwritten
49      % with the later one. Conversely, shorter sequences found
            later in the
50      % data set are discarded. When saving sequence data values,
            the start
51      % and finish indices are saved as well.
52
53      currLength = 1;
54      maxLength = 0;
55
56      for n = 1:length(rec(1,:))-1
57          if rec(1,n+1)-rec(1,n) == 1
58              currLength = currLength + 1;
59          elseif currLength > maxLength
60              maxLength = currLength;
61              currLength = 1;
62              start = n+1-maxLength;
```

```
63              finish = n;
64          else
65              currLength = 1;
66          end
67          if currLength > maxLength
68              maxLength = currLength;
69              start = n+2-maxLength;
70              finish = n+1;
71          end
72      end
73
74      % From the start and finish indices of the longest sequence,
            the data
75      % is saved into an array along with a vector of ones used in
            the
76      % averaging scheme later on.
77
78      maxSeq = rec(2:end,start:finish);
79      sd = ones(1,maxLength);
80
81      % Since the end goal is to have a sequence of points along
            the orbit
82      % equal in length to the orbit, the array would need to be
            filled in
83      % should there not be enough points. The logic behind this
```

```
        step is that
84      % if 5 consecutive points in a period 7 orbit meet the
            vicinity
85      % criteria, than the subsequent two points in the data set
            cannot be
86      % too far outside the vicinity. (Not sure this is completely
            valid).
87      % The new ammended sequence is saved as well as the
            lengthened vector
88      % of ones used in averaging.
89
90      if maxLength < period
91          n = [rec(1,finish)+1 : rec(1,finish)+period-maxLength];
92          maxSeq(:,maxLength+1:period) = data(:,n);
93          sd(1,maxLength+1:period) = ones(1,period-maxLength);
94          maxLength = period;
95          finish = start+period-1;
96      end
97
98      % While the longest sequence yields a strong correlation to
            the
99      % existence of an orbit of that period, the other recurrence
            points cannot be
100     % ignored. This step augments the max sequence to include
            points not in
```

```
101     % the longest sequence, but still within the vicinity of the
            sequence points.
102
103     for n = [1:start-1 , finish+1:length(rec(1,:))]
104         for mm = 1:maxLength
105             dx = rec(2:end,n) - maxSeq(:,mm);
106             dx = [dx(1,:)/xrange ; dx(2,:)/yrange ; dx(3,:)/
                    zrange];
107             if norm(dx,2) < eps
108                 sd(1,mm) = sd(1,mm) + 1;
109                 maxSeq(:,mm,sd(1,mm)) = rec(2:end,n);
110                 break
111             else
112             end
113         end
114     end
115
116     % The segment takes the new sequence including the added
            points in the
117     % vicinity of the original sequence stored in a 3rd dimension
            of the
118     % original sequence array. All recurrent points are then
            averaged to
119     % result in a sequence the same length as the period with a
            strong
```

```
120     % correlation of being located on the orbit. Fixed_pts is a
            cell
121     % structure that stores the orbit sequence for each period to
            be
122     % used in the later control algorithm.
123
124     newSeq = maxSeq(:,1:period,:);
125     newSD = sd(1,1:period);
126     for n = 1:maxLength-period
127         ratio = ceil(n/period)-1;
128         extra = newSD(1,n-ratio*period);
129         newSD(1,n-ratio*period) = extra + sd(1,n+period);
130         newSeq(:,n-ratio*period,1+extra:newSD(1,n-ratio*period))
                = maxSeq(:,n+period,1:sd(1,n+period));
131     end
132
133     for n = 1:period
134         pm(:,n) = sum(newSeq(:,n,1:newSD(1,n)),3)/newSD(1,n);
135     end
136 end
137 end
```

B.1.4 Fit model using linear least squares and adjust location of predicted orbit points

```
1  function [A,C,pm,orig,afb] = StateMatrixApproximation(data,m,tol,
       pm,eps,vicinity)
2  % Adapted from Witvoet 2005
3
4  dpm = ones(2*m,1); % Initial fixed point adjustment (dx,dy)
5
6  % Estimate A by Minimizing C
7  while max(abs(norm(dpm))) > tol
8      yn = [];
9      xn = [];
10     xn_tot = [];
11     for i = 1:m
12         [orig,afb] = Search_A(data,pm,eps,vicinity);
13         n = size(orig(:,:,i),2);
14         x = [ones(1,n) ; orig(:,:,i)]';
15         y = afb(:,:,i)';
16         c = x\y;
17         A(:,:,i) = c(2:end,:)';
18         C(:,:,i) = c(1,:)';
19     end
20     for i = 1:m
21         for j = 1:2
22             yn = vertcat(yn, [(afb(j,:,i)-A(j,:,i)*orig(:,:,i))
                   ']);
```

```
23            end
24            xn(2*i-1:2*i  , 2*i-1:2*i) = -A(:,:,i);
25        end
26        if m > 1
27            xn = xn + diag(ones(2*m-2,1),2);
28            xn(end-1:end,1:2) = eye(2);
29        else
30            xn = eye(2) + xn;
31        end
32
33        for i = 1:2*m
34            xn_tot = vertcat(xn_tot, [repmat(xn(i,:),n,1)]);
35        end
36
37        dpm = xn_tot\yn;
38
39        if max(abs(norm(dpm))) > tol
40            dp_vec = [dpm(1:2:end)'; dpm(2:2:end)'];
41            pm(1:2,:) = pm(1:2,:) + dp_vec;
42        end
43    end
44    end
```

B.2 Internal functions used in linear least squares approximation

B.2.1 Function to find points for A approximation near an orbit point

```
function [orig,afb] = Search_A(data,pm,eps,vicinity)
% Adapted from Witvoet 2005

xrange = max(data(1,:))-min(data(1,:));
yrange = max(data(2,:))-min(data(2,:));

    % Searching points within 'eps'
    orbit_points = [ pm , pm(:,1) ];
    k = ones(size(pm,2),1);

    for i = 1:(length(data)-1)
        for j = 1:size(orbit_points,2)-1
            ddata = data(:,i) - orbit_points(:,j);
            ddata = [ddata(1,1)/xrange ; ddata(2,1)/yrange];
            ksi1 = norm(ddata,2);
            clear ddata

            if ksi1 < vicinity(j)*eps
                ddata = data(:,i+1) - orbit_points(:,j+1);
                ddata = [ddata(1,1)/xrange ; ddata(2,1)/yrange];
                ksi2 = norm(ddata,2);
                clear ddata
```

```
23
24                      if ksi2 < vicinity(j)*eps
25                          orig(:,k(j),j) = data(:,i) - orbit_points(:,j
                                );
26                          afb(:,k(j),j) = data(:,i+1) - orbit_points(:,
                                j+1);
27                          k(j) = k(j)+1;
28                          break
29                      else
30                      end
31                  else
32                  end
33              end
34          end
35      end
```

B.2.2 Function to find points for B approximation near an orbit point

```
function [orig,afb] = Search_B(data_dp,pm,eps,vicinity)
% Adapted from Witvoet 2005

xrange = max(max(data_dp(1,:,:)))-min(min(data_dp(1,:)));
yrange = max(max(data_dp(2,:,:)))-min(min(data_dp(2,:)));

    orbit_points = [ pm , pm(:,1) ];
    k = ones(size(pm,2),1);

    for i = 1:(length(data_dp)-1)
        for j = 1:size(orbit_points,2)-1
            ddata_d = data_dp(:,i,1) - orbit_points(:,j);
            ddata_d = [ddata_d(1,1)/xrange ; ddata_d(2,1)/yrange
               ];
            ksi1 = norm(ddata_d,2);
            clear ddata_d

            if ksi1 < vicinity(j)*eps
                ddata_d = data_dp(:,i,2) - orbit_points(:,j+1);
                ddata_d = [ddata_d(1,1)/xrange ; ddata_d(2,1)/
                   yrange];
                ksi2 = norm(ddata_d,2);
                clear ddata_d

```

```
23                  if ksi2 < vicinity(j)*eps
24                      orig(:,k(j),j) = data_dp(:,i,1) -
                            orbit_points(:,j);
25                      afb(:,k(j),j) = data_dp(:,i,2) - orbit_points
                            (:,j+1);
26                      k(j) = k(j)+1;
27                      break
28                  else
29                  end
30              else
31              end
32          end
33      end
34
35  end
```

B.2.3 Function to estimate the B matrix

```
function [B,orig,afb] = Estimate_B(data_dp,pm,A,eps,dp_eps,
    vicinity)
% Adapted from Witvoet 2005

    period = size(pm,2);
    % Looking for points close to the orbits
    [orig,afb] = Search_B(data_dp,pm,eps,vicinity);
    % Estimating B
    for i = 1:period;
        temp_afb = afb(:,:,i);
        while temp_afb(:,end) == [0;0];
            temp_afb = temp_afb(:,1:(end-1));
        end
        temp_orig = orig(1:2,1:size(temp_afb,2),i);
        n = size(temp_orig,2);
        x = temp_orig';
        y = temp_afb';
        ball = temp_afb - A(:,:,i)*temp_orig;
        nul = zeros(1,n);
        bave = mean(ball,2);
        B(:,:,i) = bave/dp_eps;
    end
end
```

B.3 Control computation for OGY control and sliding mode gains

B.3.1 Create the matrix formed through multiplication of all A matrices

```
function phi = MakePhi(A,u,i,j)
% Adapted from Witvoet 2005

m = size(A,3);
if j > u-1
    phi = zeros(0,size(A,1));
else
    while i+j > m
        i = i-m;
    end
    phi = A(:,:,i+j);
    while j < u-1
        j = j+1;
        while i+j > m
            i = i-m;
        end
        phi = A(:,:,i+j) * phi;
    end
end
```

B.3.2 Create the modified controllability matrix

```
function [C,u] = MakeC(A,B)
```

```
% Adapted from Witvoet 2005

m = size(A,3);

% Calculation number of stable and unstable eigenvectors
prod = A(:,:,m);
for i = 1:m-1
    prod = prod*A(:,:,m-i);
end
clear i

d = eig(prod);
s = 0; u = 0;
for i = 1:length(d)
    if abs(d(i)) < 1
        s = s+1;
    elseif abs(d(i)) > 1
        u = u+1;
    else
    end
end
clear i prod d

% Calculation stable eigenvectors for every point
for i = 1:m
```

```
27      stab = A(:,:,i);
28      j = i-1;
29      for n = 1:m-1
30          if j == 0
31              j = m;
32          else
33          end
34          stab = stab*A(:,:,j);
35          j = j-1;
36      end
37      [v,d] = eig(stab);
38      z=1;
39      for n=1:length(d)
40          if abs(d(n,n)) < 1
41              vs(:,z,i) = v(:,n);
42              z=z+1;
43          else
44          end
45      end
46  end
47  clear i j n z v d stab
48
49  % Creation of C (by using makephi)
50  for i = 1:m
51      iu = i+u;
```

```
52      iumin = i+u-1;
53      while iu > m
54          iu = iu-m;
55      end
56      while iumin > m
57          iumin = iumin-m;
58      end
59      temp = [ B(:,:,iumin) , vs(:,:,iu) ];
60      if u-1 < 1
61      else
62          for j = 1:u-1
63              temp = [MakePhi(A,u,i,u-j) , temp];
64          end
65      end
66      C(:,:,i) = temp;
67  end
68  clear i j temp
```

B.3.3 Compute the control gains for the OGY controller

```
function K = MakeK(A,C,u)
% Adapted from Witvoet 2005

    m = size(C,3);
    kappa = zeros(1,size(C,1));
    kappa(1,1) = 1;
    for i = 1:m;
        temp = kappa*inv(C(:,:,i))*MakePhi(A,u,i,0);
        K(:,:,i) = temp';
    end
end
```

B.3.4 Compute control gains using the sliding mode controller

```
function [K, K_T, A_CCF, B_CCF, T] = SlidingModeGains(A,B,m,F)

% Duplicate A and B to 2p

for i = 1:m
    A(:,:,m+i) = A(:,:,i);
    B(:,:,m+i) = B(:,:,i);
end
% Calculate components of t if matrix controllable
for i = 1:m
    if m == 1
        U(:,:,i) = [B(:,:,i), A(:,:,i)*B(:,:,i)];
    else
        U(:,:,i) = [B(:,:,(i+m-1)), A(:,:,(i+m-1))*B(:,:,(i+m-2))
            ];
    end
    if det(U(:,:,i)) == 0
        disp('System is not controllable')
    else
        t(:,:,i) = [0,1]/U(:,:,i);
    end
end
% Group together to determine components of T
for i = 1:m
```

```
24      t(:,:,m+i) = t(:,:,i);
25  end
26  for i = 1:m
27     T(:,:,i) = [t(:,:,i); t(:,:,i+1)*A(:,:,i)];
28  end
29  % Duplicate T for Controllable Canonical Form Conversion
30  for i = 1:m
31      T(:,:,m+i) = T(:,:,i);
32  end
33  % Compute Canonical Form
34  for i = 1:m
35      A_CCF(:,:,i) = T(:,:,i+1)*A(:,:,i)*inv(T(:,:,i));
36      B_CCF(:,:,i) = T(:,:,i+1)*B(:,:,i);
37  end
38  K_CCF(:,:,1) = [-A_CCF(2,1,1); -A_CCF(2,2,1)];
39  K_CCF(:,:,2) = [-A_CCF(2,1,2); -A_CCF(2,2,2)];
40  for i = 1:m
41      K_T(:,:,i) = ((inv(T(:,:,i+1))*F*T(:,:,i)) - A(:,:,i))/B(:,:,
            i)';
42  %      K_CCF(:,:,i) = (F - A_CCF(:,:,i))/B_CCF(:,:,i)';
43      K(:,:,i) = (K_CCF(:,:,i)'*T(:,:,i))';
44  end
45  end
```

B.4 Master scripts to initialize functions and process intermediate data

B.4.1 Standalone script for control within the chaotic attractor

```
%%%%%%%%%%%%%%%%%%%%%%%%
%%%%%%%%%%%%%%%%%%%%%%%%
% Tunable Parameters
%%%%%%%%%%%%%%%%%%%%%%%%
%%%%%%%%%%%%%%%%%%%%%%%%
global omega zeta f kappa2 gamma lambda
omega = 0.8; zeta = 0.01; f = 0.08; lambda = 0.05; gamma = 0.5; kappa2 = 0.05;
period = 2*pi/omega;

% Initial conditions and time vectors
begin = [1 0 0];
time_cont = [0 250000];

% Orbit considered for stabilization
m = 2;

% Vicinity and Perturbation amount for prediction and control
eps = 0.025;          % Used in orbit selection, and region surrounding fixed points
eps = 0.1;
dp_eps = 0.0051;      % Used in perturbation of the map for
```

```
    selecting B
p = 0;                % For use in applying control should steady
    state value be different
du_eps = dp_eps;      % Region for control application (same as B)
F = [0 1; 1 0];       % Invariant matrix for Sliding Mode Control

% Compute vicinity for individual orbit points in A, B estimation
vicinity = ones(1,m)*2;

% Stopping criteria for A and fixed point correction
tol = 1e-4;

%%%%%%%%%%%%%%%%%%%%%%%%%%%%%%%%%%%%%%%%%%%%%%%%%%%%%%%%%%%%%%%%%%%%%%%%
%%%%%%%%%%%%%%%%%%%%%%%%%%%%%%%%%%%%%%%%%%%%%%%%%%%%%%%%%%%%%%%%%%%%%%%%
% Compute Duffing Data Sets and Fixed Points
%%%%%%%%%%%%%%%%%%%%%%%%%%%%%%%%%%%%%%%%%%%%%%%%%%%%%%%%%%%%%%%%%%%%%%%%
%%%%%%%%%%%%%%%%%%%%%%%%%%%%%%%%%%%%%%%%%%%%%%%%%%%%%%%%%%%%%%%%%%%%%%%%

eind = time_cont(2);
nop_end = ceil(eind/period);
time_poincare = [0:period:nop_end];

% Compute time series and Poincare data
[t_cont,x_cont] = ode45(@Duffing_Piezo_3D,time_cont,begin);
% [t_lar,x_lar] = ode45(@Duffing_Piezo_3D,time_cont,[1,1.3,0]);
```

```
[tp,xp] = ode45(@Duffing_Piezo_3D,time_poincare,begin);
% data_total = [xp(:,1),xp(:,2),xp(:,3)]';
% data = [xp(:,1),xp(:,2)]';

[Dx, Dy, Dz] = Poincare_Time(x_cont, t_cont, omega, 0);
data = [Dx; Dy]';

%%%%%%%%%%%%%%%%%%%%%%%%%%%%%%%%%%%
% Initial Estimate of Fixed Point
%%%%%%%%%%%%%%%%%%%%%%%%%%%%%%%%%%%
pm = RecurrenceMethod(data,m,eps);

%%%%%%%%%%%%%%%%%%%%%%%%%%%%%%%%%%%%%%%%%%%%%%%%%%%%%%%
% Iterated Improvements of A,B, and Fixed Points
%%%%%%%%%%%%%%%%%%%%%%%%%%%%%%%%%%%%%%%%%%%%%%%%%%%%%%%

[A,C,pm,orig_a,afb_a] = StateMatrixApproximation(data,m,tol,pm,
    eps,vicinity);

for i = 1:m
figure(i),plot3(orig_a(1,:,i),orig_a(2,:,i),afb_a(:,:,i),'.'),
    grid
end

data_perturb = begin;
```

```
67 begin_per = begin;
68
69 for k = 1:length(data)
70     if rem(k,2) ~= 0
71         u_per = p + dp_eps;
72     else
73         u_per = p;
74     end
75     timedc = [(k-1)*period k*period];
76     [t_per,x_per] = ode45(@Duffing_Perturbed_3D,timedc,begin_per
           ,[],u_per);
77     begin_per = [x_per(end,1) x_per(end,2) x_per(end,3)];
78     data_perturb = vertcat(data_perturb, begin_per);
79
80 end
81
82 data_perturb = data_perturb';
83
84 j = 1;
85 for i = 1:2:length(data_perturb)
86     dp_sep(:,j,1) = data_perturb(:,i);
87     j = j+1;
88 end
89 j = 1;
90 for i = 2:2:length(data_perturb)
```

```
    dp_sep(:,j,2) = data_perturb(:,i);
    j = j+1;
end

dp_sep_2D = dp_sep(1:2,:,:);

[B,orig_b,afb_b] = Estimate_B(dp_sep_2D,pm,A,eps,dp_eps,vicinity);

for i = 1:m
figure(m+i),plot3(orig_b(1,:,i),orig_b(2,:,i),afb_b(:,:,i),'.'),grid
end

%%%%%%%%%%%%%%%%%%%%%%%%%%%%%%%%%%%%%%
% Sliding Mode Control Gains
%%%%%%%%%%%%%%%%%%%%%%%%%%%%%%%%%%%%%%

[K, K_A, A_CCF, B_CCF, T] = SlidingModeGains(A,B,m,F);
K = -K;

[Cc,u] = MakeC(A,B);
K_B = MakeK(A,Cc,u);

%%%%%%%%%%%%%%%%%%%%%%%%
```

```
%%%%%%%%%%%%%%%%%%%%%%%%
% Apply Control
%%%%%%%%%%%%%%%%%%%%%%%%
%%%%%%%%%%%%%%%%%%%%%%%%

data_tot = [];
rdata = begin';

for i = 1:length(data)
    for j = 1:m
        if norm((rdata(1:2,end) - pm(:,j)),2) < eps
            dp(j,1) = -K_B(:,:,j)'*(rdata(1:2,end) - pm(:,j));
            if abs(dp(j,1)) > du_eps
                dp(j,1) = 0;
            end
        else
            dp(j,1) = 0;
        end
    end
    test = find(dp);
    [e,d]=min(abs(dp(test)));
    dp=dp(test(d));
        if isempty(dp)
        dp = 0;
    else
```

```
139     end
140         u_dp(i) = p + dp;
141         timedc = [(i-1)*period i*period];
142         u_c = u_dp(i);
143         [tdc,xdc] = ode45(@Duffing_Piezo_Control_3D,timedc,begin
                ,[],u_c);
144         temp = [tdc xdc];
145         data_tot = vertcat(data_tot, temp);
146         rdata(:,i+1) = [xdc(end,1); xdc(end,2); xdc(end,3)];
147         begin = xdc(end,:);
148 end
```

B.4.2 Standalone script for control across attractors

```
%%%%%%%%%%%%%%%%%%%%%%%%%%
%%%%%%%%%%%%%%%%%%%%%%%%%%
% Tunable Parameters
%%%%%%%%%%%%%%%%%%%%%%%%%%
%%%%%%%%%%%%%%%%%%%%%%%%%%

global omega gamma lambda kappa2 zeta f
omega = 0.8; zeta = 0.01; chi = 0.05; kappa = 0.5; lambda = 0.05;
    f = 0.08;
period = 2*pi/omega;

%%%%%%%%%%%%%%%%%%%%%%%%%%%%
% Set initial conditions
%%%%%%%%%%%%%%%%%%%%%%%%%%%%
x1(1) = 1;
x2(1) = 0;
x3(1) = 0;
x1d(1) = 1;
x2d(1) = 1.3;
x3d(1) = 0;

dt = 1E-2;
tk = 0:dt:500;
u_max = 1;
```

```
24 for i = 1:length(tk)-1
25
26     % Error Calculation
27     e1(i) = x1(i) - x1d(i);
28     e2(i) = x2(i) - x2d(i);
29
30     if tk(i) > tk(end)/2 && abs(e1(i)) < 0.05 % e1(i) >= 0 && e1(
           i) < 0.05 %
31         u(i) = -19.1*e2(i) - 2*e1(i) - x1(i)^3 - x1d(i)^3;
32         if abs(u(i)) < u_max
33             % Starting Trajectory
34             dx1dt(i) = x2(i);
35             dx2dt(i) = -2*zeta*x2(i)+(1/2)*x1(i)*(1-x1(i)^2)+chi*
                   x3(i)+f*cos(omega*tk(i)) + u(i);
36             dx3dt(i) = -lambda*x3(i)-kappa*x2(i);
37         else
38             u(i) = sign(u(i))*u_max;
39             dx1dt(i) = x2(i);
40             dx2dt(i) = -2*zeta*x2(i)+(1/2)*x1(i)*(1-x1(i)^2)+chi*
                   x3(i)+f*cos(omega*tk(i)) + u(i);
41             dx3dt(i) = -lambda*x3(i)-kappa*x2(i);
42         end
43     else
44         u(i) = 0;
45         % Starting Trajectory
```

```
46          dx1dt(i) = x2(i);
47          dx2dt(i) = -2*zeta*x2(i)+(1/2)*x1(i)*(1-x1(i)^2)+chi*x3(i
                )+f*cos(omega*tk(i));
48          dx3dt(i) = -lambda*x3(i)-kappa*x2(i);
49      end
50
51      x1(i+1) = dt*dx1dt(i) + x1(i);
52      x2(i+1) = dt*dx2dt(i) + x2(i);
53      x3(i+1) = dt*dx3dt(i) + x3(i);
54
55      % Desired Trajectory
56      dx1dtd(i) = x2d(i);
57      dx2dtd(i) = -2*zeta*x2d(i)+(1/2)*x1d(i)*(1-x1d(i)^2)+chi*x3d(
            i)+f*cos(omega*tk(i));
58      dx3dtd(i) = -lambda*x3d(i)-kappa*x2d(i);
59
60      x1d(i+1) = dt*dx1dtd(i) + x1d(i);
61      x2d(i+1) = dt*dx2dtd(i) + x2d(i);
62      x3d(i+1) = dt*dx3dtd(i) + x3d(i);
63  end
```

LIST OF REFERENCES

[1] Elvin N, Erturk A (2013) *Advances in energy harvesting methods*, Springer. doi:10.1007/978-1-4614-5705-3.

[2] Mitcheson P, Yeatman E, Rao G, Holmes A, Green T (2008) "Energy harvesting from human and machine motion for wireless electronic devices," *Proc. of IEEE* 96 (9): 1457–1486. doi:10.1109/JPROC.2008.927494.

[3] Bennett D, Selfridge R, Humble P, Harb J (2001) "Hybrid power systems for autonomous mems," *Proc. SPIE* 4334: 354–362. doi:10.1117/12.436621.

[4] Bottner H (2002) "Thermoelectric micro devices: Current state, recent developments, and future aspects for technological progress and applications," *Proc. 21st International Conference on Thermoelectronics* pages 511–518. doi:10.1109/ICT.2002.1190368.

[5] Mantiply E, Pohl K, Poppell S, Murphy J (1997) "Summary of measured radiofrequency electric and magnetic fields (10 khz to 30 ghz) in the general and work environment," *Bioelectromagnetics* 18 (8): 563–577.

[6] Glynne-Jones P, Tudor M, Beeby S, White N (2004) "An electromagnetic, vibration-powered generator for intelligent sensor systems," *Sensors and Actuators A* 110: 344–349. doi:10.1016/j.sna.2003.09.045.

[7] Mitcheson P, Miao P, Stark B, Yeatman E, Holmes A, Green T (2004) "MEMS electrostatic micro-power generator for low frequency operation," *Sensors and Actuators A* 115: 523–529. doi:10.1016/j.sna.2004.04.026.

[8] Kornbluh R, Pelrine R, Pei Q, Heydt R, Stanford S, Oh S, Eckerle J (2002) "Electroelastomers: Applications of dielectric elastomer transducers for actuation, generation, and

smart structures," *Proc. Smart Structures and Materials Conference* 4698: 254–270. doi:10.1117/12.475072.

[9] Anton S, Sodano H (2007) "A review of power harvesting using piezoelectric materials (2003-2006)," *Smart Materials and Structures* 16. doi:10.1088/0964-1726/16/3/R01.

[10] Bielsa A (2013) "Smart roads — wireless sensor networks for smart infrastructures: A billion dollar business opportunity,". URL: http://www.libelium.com/smart_roads_wsn_smart_infrastructures/.

[11] Roundy S, Wright P, Rabaey J (2004) *Energy scavenging for wireless sensor networks with special focus on vibrations*, Kluwer Academic Publishers: Norwell, MA 1 edition. doi:10.1007/978-1-4615-0485-6.

[12] Vocca H, Cottone F (2014) "Kinetic energy harvesting," Chapter 03 in *ICT — Energy — Concepts Towards Zero — Power Information and Communication Technology*; Fagas G, Gammaitoni L, Paul D, Berini GA (editors), InTech: Rijeka. doi:10.5772/57091.

[13] Sodano H, Inman D (2004) "A review of power harvesting from vibration using piezoelectric materials," *The Shock and Vibration Digest* 36 (3): 197–205.

[14] Moon F, Holmes P (1979) "A magnetoelastic strange attractor," *Journal of Sound and Vibration* 65 (2): 275–296. doi:10.1016/0022-460X(79)90520-0.

[15] Harne R, Wang K (2013) "A review of the recent research on vibration energy harvesting via bistable systems," *Smart Materials and Structures* 22. doi:10.1088/0964-1726/22/2/023001.

[16] Daqaq M, Masana R, Erturk A, Quinn D (2014) "On the role of nonlinearities in vibratory energy harvesting: A critical review and discussion," *Applied Mechanics Review* 66 (040801-1 0– 040801-23). doi:10.1115/1.4026278.

[17] Stanton S, Owen B, Mann B (2012) "Harmonic balance analysis of the bistable piezoelectric inertial generator," *Journal of Sound and Vibration* 331 (15): 3617–3627. doi:10.1016/j.jsv.2012.03.012.

[18] Harne R, Thota M, Wang K (2013) "Concise and high-fidelity predictive criteria for maximizing performance and robustness of bistable energy harvesters," *Applied Physics Letters* 102: 053903. doi:10.1063/1.4790381.

[19] Erturk A, Hoffman J, Inman D (2009) "A piezomagnetoelastic structure for broadband vibration energy harvesting," *Applied Physics Letters* 94 (254102). doi:10.1063/1.3159815.

[20] Ott E, Grebogi C, Yorke J (1990) "Controlling chaos," *Physical Review Letters* 64 (11): 1196–1199. doi:10.1103/PhysRevLett.64.1196.

[21] Dosch J, Inman D (1992) "A self-sensing piezoelectric actuator for collocated control," *Journal of Intelligent Material Systems and Structures* 3: 166–185. doi:10.1177/1045389X9200300109.

[22] Curie L, Curie P (1880) "Developement par compression de Lélectricité Polaire dans les cristaux hemiedres a faces inclinees," *Bulletin de la Societe Minerologique de France* 3: 245–251. doi:10.1051/jphystap:018820010024500.

[23] Lippman G (1881) "Principe de la conservation de L'electricite," *Annales de Chimie et de Physique ou Second Principe de la Theorie des phenom'enes electriques* 24: 145. doi:10.1051/jphystap:0188100100038100.

[24] Voight W (1910) "Lehrbuch der Kristallphysik," *B. G. Teubner*. doi:10.1007/978-3-663-15884-4.

[25] Minary-Jolandan M, Yu M (2009) "Nanoscale characterization of isolated individual type I collagen fibrils: Polarization and piezoelectricity," *Nanotechnology* 20 (8). doi:10.1088/0957-4484/20/8/085706.

[26] Lee B, Zhang J, Zueger C, Chung W, Yoo S, Wang E, Meyer J, Ramesh R, Lee S (2012) "Virus-based piezoelectric energy generation," *Nature Nanotechnology* 7 (6): 351–356. doi:10.1038/nnano.2012.69.

[27] Sodano H, Inman D, Park G (2005) "Comparison of piezoelectric energy harvesting devices for recharging batteries," *Journal of Intelligent Material Systems and Structures* 16: 799–807. doi:10.1177/1045389X05056681.

[28] IEEE (1987) "IEEE standard on piezoelectricity," *ANSI/IEEE Std* 3: 176–1987. doi:10.1109/IEEESTD.1988.79638.

[29] Leo DJ (2007) *Engineering Analysis of Smart Materials*, John Wiley and Sons, Ltd. doi:10.1002/9780470209721.

[30] Hagood N, von Flotow A (1991) "Damping of structural vibrations with piezoelectric materials and passive electrical networks," *Journal of Sound and Vibration* 146 (2): 243–268. doi:10.1016/0022-460X(91)90762-9.

[31] Anon (1991) "Piezoelectric ceramics: Properties and applications," *Philips Components*.

[32] Kauffman J (2007) "Low-order modeling of a piezoelectric energy harvesting device," *Masters Thesis*.

[33] Takacs G, Rohal-Ilkiv B (2012) *Basics of vibration dynamics. In: Model predictive vibration control*, Springer: London. doi:10.1007/978-1-4471-2333-0_2.

[34] Mateu L, Moll F (2005) "Optimum piezoelectric bending beam structures for energy harvesting using shoe inserts," *Journal of Intelligent Marterial Systems and Structures* 16: 835–845. doi:10.1177/1045389X05055280.

[35] Gurav S, Kasyap A, Sheplak M, Cattafesta L, Haftka R, Goosen F, van Keulen F (2004) "Uncertainty-based design optimization of a micro piezoelectric composite energy reclamation device," *Proc. of the 10th AIAA/ISSMO Multidisplinary Analysis and Optimization Conference* pages 3559–3570. doi:10.2514/6.2004-4619.

[36] Roundy S, Leland E, Baker J, Carleton E, Reilley E, Lai E, Otis B, Rabaey J, Wright P (2005) "Improving power output for vibration-based energy scavengers," *IEEE Pervasive Computing* 4 (1): 28–36. doi:10.1109/MPRV.2005.14.

[37] Roundy S, Wright P, Rabaey J (2005) "Alternative geometries for increasing power density in vibration energy scavenging for wireless sensor networks," *Proc. of the 3rd International Energy Conversion Engineering Conference* pages 959–970. doi:10.2514/6.2005-5617.

[38] Mossi K, Green C, Ounaies Z, Hughes E (2005) "Harvesting energy using a thin unimorph prestressed Bender: Geometrical effects," *Journal of Intelligent Material Systems and Structures* 16: 249–261. doi:10.1177/1045389X05050008.

[39] Johnson T, Charnegie D, Clark W, Buric M, Kusic G (2006) "Energy harvesting from mechanical vibrations using piezoelectric cantilever beams," *Proc. of the Smart Structures and Materials Conference* 6169: 61690D. doi:10.1117/12.659466.

[40] Sodano H, Park G, Inman D (2004) "Estimation of electric charge output for piezoelectric energy harvesting," *Strain* 40 (2): 49–58. doi:10.1111/j.1475-1305.2004.00120.x.

[41] Ng T, Liao W (2004) "Feasibility study of a self-powered piezoelectric sensor," *Proc. Smart Structures and Materials Conference* 5389: 377–388. doi:10.1117/12.539706.

[42] Ng T, Liao W (2005) "Sensitivity analysis and energy harvesting for a self-powered piezoelectric sensor," *Journal of Intelligent Material Systems and Structures* 16 (10): 785–797. doi:10.1177/1045389X05053151.

[43] Jiang S, Li X, Guo S, Hu Y, Yang J, Jiang Q (2005) "Performance of a piezoelectric bimorph for scavenging vibration energy," *Smart Materials and Structures* 14: 769–774. doi:10.1088/0964-1726/14/4/036.

[44] Yoon W, Washington G, Danak A (2005) "Modeling, optimization, and design of efficient initially curved piezoceramic unimorphs for energy harvesting applications," *Journal of Intelligent Material Systems and Structures* 16: 877–888. doi:10.1177/1045389X05055759.

[45] Shahruz S (2006) "Design of mechanical band—pass filters for energy scavenging," *Journal of Sound and Vibration* 292: 987–998. doi:10.1016/j.jsv.2005.08.018.

[46] Shahruz S (2006) "Limits of performance of mechanical band—pass filters used in energy scavenging," *Journal of Sound and Vibration* 293: 449–461. doi:10.1016/j.jsv.2005.09.022.

[47] Erturk A, Renno J, Inman D (2008) "Piezoelectric energy harvesting from an L-shaped beam-mass structure," *Proc. SPIE 6928, Active and Passive Smart Structures and Integrated Systems* 692801. doi:10.1177/12.776211.

[48] Erturk A, Anton S, Inman D (2008) "Energy harvesting from rigid body motions," *Proc. of the 17th Internationsl Synposium on Application of Ferroelectrics, 3rd Annual Energy Harvesting Workshop*.

[49] Erturk A, Anton S, Inman D (2007) "Energy harvesting from rigid body motion," *Proc. of the 18th International Conference of Adaptive Structures and Technologies*.

[50] Tayahi M, Johnson B, Holtzman M, Cadet G (2005) "Piezoelectric materials for powering remote sensors," *Proc. IEEE 24th International Performance, Computing, and Communications Conference* pages 383–386. doi:10.1109/PCCC.2005.1460592.

[51] Han J, von Jouanne A, Le T, Mayaram K, Fiez T (2004) "Novel power conditioning circuits for piezoelectric micro power generators," *Proc. of the 19th Annual IEEE Applied Power Electronics Conference and Exposition Conf.* pages 1541–1546. doi:10.1109/APEC.2004.1296069.

[52] Ottman G, Hofmann H, Lesieutre G (2003) "Optimized piezoelectric energy harvesting circuit using step-down converter in discontinuous conduction mode," *IEEE Transactions on Power Electronics* 18 (2): 696–703. doi:10.1109/TPEL.2003.809379.

[53] Lesieutre G, Ottman G, Hofmann H (2004) "Damping as a result of piezoelectric energy harvesting," *Journal of Sound and Vibration* 269: 991–1001. doi:10.1016/S0022-460X(03)00210-4.

[54] Lefeuvre E, Badel A, Richard C, Guyomar D (2004) "High performance piezoelectric vibration energy reclamation," *Proc. Smart Structures and Materials Conference* 5390: 379–387. doi:10.1117/12.532709.

[55] Badel A, Guyomar D, Lefeuvre E, Richard C (2005) "Efficiency enhancement of a piezoelectric energy harvesting device in pulsed operation by synchronous charge inversion," *Journal of Intelligent Material Systems and Structures* 16: 889–901. doi:10.1177/1045389X05053150.

[56] Guyomar D, Badel A, Lefeuvre E, Richard C (2005) "Toward energy harvesting using active materials and conversion improvement by nonlinear processing," *IEEE Trans. on Ultrasonics, Ferroelectrics, and Frequency Control* 52 (4): 584–595. doi:10.1109/TUFFC.2005.1428041.

[57] Lallart M, Anton S, Inman D (2010) "Frequency self-tuning scheme for broadband vibration energy harvesting," *Journal of Intelligent Material Systems and Structures* 21: 897–906. doi:10.1177/1045389X10369716.

[58] Erturk A, Inman D (2011) "Broadband piezoelectric power generation on high-energy orbits of the bistable Duffing oscillator with electromechanical coupling," *Journal of Sound and Vibration* 330: 2339–2353. doi:10.1016/j.jsv.2010.11.018.

[59] Ott E, Hunt B (1997) "Control of chaos by means of embedded unstable periodic orbits," *Control and Chaos Mathematical Modeling* 8: 134–141. doi:10.1007/978-1-4612-2446-4_8.

[60] Vincent T (2000) "Chaotic control systems," *Nonlinear Dynamics and Systems Theory* 1 (2): 205–218.

[61] Duffing G (1918) *Erzwungene Schwingung bei veranderlicher Eigenfrequenz und ihre technische Bedeutung*, Vieweg: Braunschweig. doi:10.1002/zamm.19210010109.

[62] Brennan M, Kovacic I, Carrella A, Waters T (2008) "On the jump-up and jump-down frequencies of the duffing oscillator," *Journal of Sound and Vibration* 318: 1250–1261. doi:10.1016/j.jsv.2008.04.032.

[63] Geiyer D, Kauffman J (2015) "Chaotification as a means of broadband energy harvesting with piezoelectric materials," *ASME Journal of Vibration and Acoustics* In Print. doi:10.1115/SMASIS2014-7425.

[64] Poincaré H (1885) "L'equilibre d'une masse fluide animee d'un mouvement de rotation," *Acta Mathematica* 7: 259–380.

[65] Liu Y, Wiercigroch M, Ing J, Pavlovskaia E (2013) "Intermittent control of coexisting attractors," *Philosophical Transactions of the Royal Society A* 371: 20120428. doi:10.1098/rsta.2012.0428.

[66] Stanton S, Mann B, Owen B (2012) "Melnikov theoretic methods for characterizing the dynamics of a bistable piezolectric inertial generator in complex spectral environments," *Physica D.* 241: 711–720. doi:10.1016/j.physd.2011.12.010.

[67] Eckmann J, Ruelle D (1985) "Ergodic theory of chaos and strange attractors," *Review of Modern Physics* 57: 617–656. doi:10.1103/RevModPhys.57.617.

[68] Yagasaki K, Kouyama M (2005) "Exclusion of false periodic orbits detected from chaotic time series," *International Journal of Bifurcation and Chaos* 15 (02): 659–665. doi:10.1142/S0218127405012272.

[69] Paskota M, Mees AI, Teo KL (1995) "On control of chaos: Highler periodic orbits," *Dynamics and Control* 5 (4): 365–387. doi:10.1007/BF01968503.

[70] Lathrop DP, Kostelich EJ (1989) "Characterization of an experimental strange attractor by periodic orbits," *Physical Review A* 40 (7): 4028–4031. doi:10.1103/PhysRevA.40.4028.

[71] So P, Ott E, Sauer T, Gluckman BJ, Grebogi C, Schiff SL (1997) "Extracting unstable periodic orbits from chaotic time series data," *Physical Review E* 55 (5): 5398–5417. doi:10.1103/PhysRevE.55.5398.

[72] Witvoet G (2005) "Control of chaotic dynamical systems using OGY,".

[73] Lenz H, Obradovic D (1999) "Stabilizing higher periodic orbits of chaotic discrete-time maps," *International Journal of Bifurcation and Chaos* 9 (1): 251–266. doi:10.1142/S0218127499000134.

[74] So P, Ott E (1995) "Controlling chaos using time delay coordinates via stabilization of periodic orbits," *Physical Review E* 51 (4): 2955–1962. doi:10.1103/PhysRevE.51.2955.

[75] Eckmann JP, Kamphorst SO, Ruelle D (1987) "Recurrence plots of dynamical systems," *EPL (Europhysics Letters)* 4 (9): 973.

[76] Geiyer D, Kauffman J (2015) "Chaotic control of a piezomagnetoelastic beam for improved energy harvesting," *Proc. SPIE* 9431: 94310O. doi:10.1117/12.2084048.

[77] Geiyer D, Kauffman JL (2016) "High-dimensional chaos control algorithms for improved piezoelectric energy harvesting using a bistable structure," *ASME 2015 International Design Engineering Technical Conferences and Computers and Information in Engineering Conference* 9799: 9799. doi:10.1115/DETC2015-46654.

[78] Geiyer D, Kauffman JL (2016) "Control between coexistent attractors for optimal performance of a bistable piezoelectric vibration energy harvester," *Proc. SPIE* 9799: 9799. doi:10.1117/12.2222125.

[79] Liao Y, Sodano HA (2009) "Optimal parameters and power characteristics of piezoelectric energy harvesters with an rc circuit," *Smart Materials and Structures* 18 (4): 045011. doi:10.1088/0964-1726/18/4/045011.

[80] Ditto W, Rauseo S, Spano M (1990) "Experimental control of chaos," *Physical Review Letters* 65 (26): 3211–3214. doi:10.1103/PhysRevLett.65.3211.

[81] Zhou S, Cao J, Inman DJ, Lin J, Liu S, Wang Z (2014) "Broadband tristable energy harvester: Modeling and experiment verification," *Applied Energy* 133: 33 – 39. doi:10.1016/j.apenergy.2014.07.077.